



UPPSALA
UNIVERSITET

*Digital Comprehensive Summaries of Uppsala Dissertations
from the Faculty of Science and Technology 2132*

Studies of second coordination sphere effects and metal variations on [FeFe]-hydrogenase mimics

HOLLY J. REDMAN



ACTA
UNIVERSITATIS
UPSALIENSIS
UPPSALA
2022

ISSN 1651-6214
ISBN 978-91-513-1461-7
URN urn:nbn:se:uu:diva-470634

Dissertation presented at Uppsala University to be publicly examined in Polhemsalen(10134), Lägerhyddsvägen 1, 752 37 Uppsala, Uppsala, Friday, 20 May 2022 at 09:00 for the degree of Doctor of Philosophy. The examination will be conducted in English. Faculty examiner: Professor Pickett Chris (University of East Anglia).

Abstract

Redman, H. J. 2022. Studies of second coordination sphere effects and metal variations on [FeFe]-hydrogenase mimics. *Digital Comprehensive Summaries of Uppsala Dissertations from the Faculty of Science and Technology* 2132. 121 pp. Uppsala: Uppsala universitet. ISBN 978-91-513-1461-7.

Mitigation of climate change motivates researchers to explore hydrogen as a potential energy carrier. Unfortunately, widespread use of hydrogen as an energy carrier is limited by numerous challenges in its production, including high energy consumption; high economic cost; current reliance on rare metals such as platinum. Diiron hydrogenases could provide a solution to the above-mentioned challenges because they are able to turnover hydrogen at very high frequencies, and utilise earth abundant iron as the redox active centre. However, diiron hydrogenases are not currently a scalable technology, and more research is needed to fully understand their reaction mechanism, and to allow engineering of optimal proton reduction catalysts. The H-cluster is an hexanuclear iron cluster in the active site, which consists of a [Fe₄S₄]-cluster and a [Fe₂S₂] cofactor. The [Fe₄S₄]-cluster behaves as a redox active ligand for the [Fe₂S₂] cofactor. The [Fe₂S₂] cofactor is a diiron complex in which the irons share a bridging azadithiolato ligand, and one bridging carbonyl ligand. Each iron has one terminal carbonyl ligand and one cyanide ligand. The [Fe₄S₄]-cluster and [Fe₂S₂] cofactor are coupled via a bridging cysteine thiol. Several mechanisms for the diiron hydrogenase enzyme have been put forth, and are still debated. In parallel synthetic chemists continue to develop a diverse array of structural and functional mimics of the diiron hydrogenase active site. This thesis aims to examine several aspects of the H-cluster from a molecular design perspective, utilising FTIR, electrochemistry, EPR, XAS, among other spectroscopic techniques, to do so. Paper I studies the effects of the bridgehead ligand in the outer coordination sphere, and what effect this has on the oxygen tolerance and reduction chemistry. Papers II and III investigate the effect of tuning the electron density on the iron centres through the incorporation of a redox active ligand (paper II) or through introduction of capping Lewis acidic moieties on the cyanide ligands of the diiron cofactor (paper III). Paper III also reports on the potential role played by the Lewis acid in protecting the cyanide ligands from proton attack during catalysis. In paper IV a new synthetic mimic is synthesised in which the iron is replaced with manganese while the coordination environment remains intact. The results from these studies inform on future design perspectives for diiron hydrogenase active site mimics.

Keywords: hydrogenases, synthesis, inorganic chemistry, molecular biomimetics, spectroscopy, FTIR, cyclic voltammetry, catalysis

Holly J. Redman, Department of Chemistry - Ångström, Molecular Biomimetics, Box 523, Uppsala University, SE-75120 Uppsala, Sweden.

© Holly J. Redman 2022

ISSN 1651-6214

ISBN 978-91-513-1461-7

URN urn:nbn:se:uu:diva-470634 (<http://urn.kb.se/resolve?urn=urn:nbn:se:uu:diva-470634>)

“Think of yourself as your own pet, and be gently fascinated and amused by the mad-ass crazy shit that’s happening to you as you march on down life’s long path.”

Caitlin Moran

List of Papers

This thesis is based on the following papers, which are referred to in the text by their Roman numerals.

- I. Vincent C.-C. Wang, Charlène Esmieu, Holly J. Redman, Gustav Berggren, Leif Hammarström. (2020) **The reactivity of molecular oxygen and reactive oxygen species with [FeFe] hydrogenase bi-mimetics: reversibility and the role of the second coordination sphere.** *Dalton Transactions*, 49, 858–865
- II. Charlène Esmieu, Meiyuan Guo, Holly J. Redman, Marcus Lundberg, Gustav Berggren. (2019) **Synthesis of a miniaturized [FeFe] hydrogenase model system.** *Dalton Transactions*, 48, 2280–2284
- III. Holly J. Redman, Michael Haumann, Mun Hon Cheah, Gustav Berggren. (2022) **Borane protected cyanide ligands tune the electron density on an [FeFe]-Hydrogenase mimic.** *Dalton Transactions*, 51, 4634-4643
- IV. Holly J. Redman, Mun Hon Cheah, Gustav Berggren. (2022) **Ex-changing iron for manganese in a [FeFe]-hydrogenase mimic: synthesis, characterisation and semi-synthetic enzyme,** Manuscript in preparation

Reprints were made with permission from the Royal Society of Chemistry.

Papers not included in this thesis

- V. Brigitta Nemeth, Charlene Esmieu, Holly J. Redman and Gustav Berggren. (2019) **Monitoring H-cluster assembly using a semi-synthetic HydF protein.** *Dalton Transactions*, 48, 5978-5986
- VI. Henrik Land, Pierre Ceccaldi, Livia S. Meszaros, Holly J. Redman, Moritz Senger, Sven T. Stripp, and Gustav Berggren. (2019) **Discovery of novel [FeFe]-hydrogenases for biocatalytic H₂-production.** *Chemical Science*, 10, 9941-9948

- VII. Livia S. Meszaros, Pierre Ceccaldi, Marco Lorenzi, Holly J. Redman, Emmanuel Pfitzner, Joachim Heberle, Moritz Senger, Sven T. Stripp, and Gustav Berggren. (2020) **Spectroscopic investigations under whole-cell conditions provide new insight into the metal hydride chemistry of [FeFe]-hydrogenase**. *Chemical Science*, 11, 4608-4617
- VIII. Brigitta Nemeth, Moritz Senger, Holly J. Redman, Pierre Ceccaldi, Joan Broderick, Ann Magnuson, Sven T. Stripp, Michael Haumann and Gustav Berggren. (2020) **[FeFe]-hydrogenase maturation: H-cluster assembly intermediates tracked by electron paramagnetic resonance, infrared, and X-ray absorption spectroscopy**. *JBIC Journal of Biological Inorganic Chemistry*, 25, 777-788
- IX. Henrik Land, Alina Sekretareva, Ping Huang, Holly J. Redman, Brigitta Nemeth, Nakia Polidori, Livia Meszaros, Moritz Senger, Sven T. Stripp, Gustav Berggren. (2020) **Characterization of a putative sensory [FeFe]-hydrogenase provides new insight into the role of the active site architecture**. *Chemical Science*, 11, 12789-12801
- X. Marco Lorenzi, Pierre Ceccaldi, Patricia Rodríguez-Macia, Holly J. Redman, Afridi Zamader, James A. Birrell, Livia S. Mészáros, Gustav Berggren. (2021) **Stability of [FeFe]-hydrogenases under whole-cell conditions**, *JBIC Journal of Biological Inorganic Chemistry*, 27, 345-355
- XI. Moritz Senger, Tobias Kernmayr, Marco Lorenzi, Holly J. Redman and Gustav Berggren. (2022) **Hydride state accumulation in native [FeFe]-hydrogenase with the physiological reductant H₂ supports its catalytic relevance**, *Chemical communications*, Submitted

Review papers not included in this thesis

- Livia Meszaros, Henrik Land, Holly J. Redman, Gustav Berggren. (2021) **Semi-synthetic hydrogenases-in vitro and in vivo applications**. *Current Opinion in Green and Sustainable Chemistry*, 32:100521

Contribution Report

- I. Supported in interpretation of results, co-wrote the manuscript, supported in the revising and editing process.
- II. Performed some FTIR experiments, assisted in synthesis, co-wrote the manuscript, supported in the revising and editing process.
- III. Conceptualisation, carried out synthesis and characterisation, led investigation of electrochemistry and redox chemistry, measurements of electrochemistry, FTIR and some EPR and assisted in XAS, formal analysis of electrochemistry and FTIR data, wrote original manuscript with support and feedback from co-authors.
- IV. Conceptualisation, carried out synthesis and characterisation, led investigation of electrochemistry and redox chemistry, measurements of electrochemistry, FTIR and some EPR, formal analysis of electrochemistry and FTIR data, wrote original manuscript with support and feedback from co-authors.

Contents

Contribution Report	7
Chapter 1: Introduction	13
General	13
1.1 Hydrogenases	14
1.2 [FeFe]-H ₂ ases	17
1.3 Artificial maturation	20
1.4 Structural mimics of the H-cluster	21
1.5 Other proton reduction catalysts	27
1.6 Solid state catalysts for hydrogen production	30
1.7 Summary and Aims	31
Chapter 2: Experimental methods	33
2.1 FTIR spectroscopy	33
2.2 EPR spectroscopy	38
2.3 X-ray absorption spectroscopy (XAS)	41
2.4 Electrochemistry	43
Chapter 3: Paper I Oxygen tolerance	49
Introduction	49
2.2 Reactivity of 1a	51
2.3 Reactivity of 2a	57
3.4 Comparison of 1a and 2a	62
3.5 Conclusions and outlook	63
Chapter 4: Paper II Synthetic H-cluster	65
Introduction	65
4.1 Synthesis of the [Fe ₄ S ₄]-cluster	66
4.2 Maturation of the [Fe ₄ S ₄]-cluster to form a miniaturised hydrogenase	68
3.3 Activity of 2b -[Fe ₄ S ₄]-FdM	71
3.4 Conclusions and outlook	71
Chapter 5: Paper III Protecting the Cyanide ligands	73
Introduction	73
5.1 Synthesis of borane capped mimic and formation of the bridging hydride	75

5.2 Oxidation chemistry.....	77
5.3 Reduction chemistry.....	79
5.4 Conclusions and outlook.....	80
Chapter 6: Paper IV Metal exchange	82
Introduction	82
6.1 Synthesis of a manganese metal-exchange [FeFe]-H ₂ ase cofactor mimic	84
6.2 Ligand substitution chemistry of 36a	86
6.3 Electrochemistry of 36a	91
6.4 Electrochemistry of 36b-d	92
6.5 Chemical reduction of 36a-d	94
6.6 Conclusions and outlook.....	96
Chapter 7: Concluding remarks	98
Popular science description.....	101
Svensk Sammanfattning.....	102
Acknowledgements.....	103
References.....	105
Appendix I – Synthesis of selected cofactor mimics	115
Appendix 2 – Synthesis of 36e and using 36e to make a semi-synthetic [FeFe]-hydrogenase	119

Abbreviations

[Fe]-H ₂ ase	Monoiron hydrogenase
[FeFe]-H ₂ ase	Diiron hydrogenase
[NiFe]-H ₂ ase	Nickel-iron hydrogenase
adt	Azadithiolate
Ag AgCl	Silver/silver chloride reference electrode
BCF	Tris(pentafluorophenyl)borane
Cl ₃ CCOOH	Trichloroacetic acid
ClCH ₂ COOH	Chloroacetic acid
CoCp* ₂	Decamethylcobaltocene
CoCp ₂	Cobaltocene
Cr(bz) ₂	Dibenzylchromium
DCM	Dichloromethane
DFT	Density functional theory
dppv	Cis-1,2-C ₂ H ₂ (PPh ₂) ₂ , cis-1,2-bis(diphenylphosphaneyl)ethane
E ⁰	Standard potential
E ^{0'}	Formal potential
E _{1/2}	Half wave potential
E _{p,a}	Peak anodic potential
E _{p,c}	Peak cathodic potential
EPR	Electron paramagnetic resonance
EXAFS	Extended X-ray absorption fine structure
	Fc ^{+/0}
FTIR	Ferrocene internal reference
GMP	Fourier transform infrared
i _{p,a}	Guanylylpyridinol
i _{p,c}	Peak anodic current
j ₀	Peak cathodic current
kcal	Exchange current density
mCPBA	Energy unit equivalent to 4.184 kJ
Methylene-H4MPT	Meta-Chloroperoxybenzoic acid
ORR	Methenyltetrahydromethanopterin
PCET	Oxygen reduction reaction
pdt	Proton coupled electron transfer
PGM	Propanedithiolate
	Platinum group metals

RNR	Ribonucleotide reductase
ROS	Reactive oxygen species
SCE	Standard calomel reference electrode
SHE	Standard hydrogen reference electrode
SOD	Superoxide dismutase
TOF	Turnover frequency
TON	Turnover number
XANES	X-ray attenuated near edge structure
XAS	X-ray absorption spectroscopy

Chapter 1: Introduction

General

At the time of writing, we have less than 8 years to make the changes necessary in order to prevent irreversible damage to the Earth's climate caused by human use of fossil fuels.¹ Society has grown used to abundant energy sources, becoming dependent on finite resources such as coal, natural gas and oil. This extraordinary consumption has led to a depletion of resources and an increasing global average temperature (due to greenhouse gas emissions).²⁻⁴ The predicted outcome of this pattern is bleak. It does, however, provide motivation and inspiration to pursue research on sustainable energy solutions.¹ What is required of a sustainable energy source? It must be renewable, abundant and reliable.^{3,4}

The most abundant energy source is the Sun, and energy can be captured from it using solar cells (also known as photovoltaics, PV). PVs have been a rapidly growing source of energy in recent years, and are now one of the cheapest sources of electricity. However there are some limitations regarding the intermittency of PVs. Simply put, PVs are ineffective at night and on short days due to the diurnal nature of sunlight. This means that electricity from PVs must either be used immediately or stored, usually inside batteries. However, battery technology is currently limited by the challenge of their relatively low energy density as compared to some liquid fuels.⁵ For example, the lithium ion battery used for Tesla's electric vehicles has an energy density of 1.86 MJ/l,⁶ whereas hydrogen gas has energy density of ~10 MJ/l and that of methanol is ~18 MJ/l.⁷ Consequently, it would be excellent if the electricity produced by PV cells could be used to drive electrochemical conversion of feedstocks to energy carriers such as molecular hydrogen or other hydrogen containing fuels.

Terms such as *hydrogen economy* or *hydrogen society* are becoming increasingly more mainstream as hydrogen becomes recognized as the energy carrier of the future. It is widely viewed as a necessary aspect of the energy transition to a carbon-free economy. Hydrogen could provide a quarter of Europe's energy demand by 2050, if its potential is fully tapped. This is expected to reduce CO₂ emissions by 560 Mt, from total European CO₂ emissions of 3536 Mt in 2015.⁸ That is the same as if half of global passenger flights were grounded, according to 2019 figures on CO₂ emissions from the aviation industry.⁹ The energy required to produce future energy carriers should come

from multiple renewable sources, i.e. solar, wind, hydroelectric. In order to achieve the ambitious but vital goals set out by the Paris agreement in 2015, these sources must be renewable and carbon neutral. This vision of the future will require the development of new and sustainable technologies.

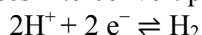
An important issue facing scientist working on hydrogen production is how to produce hydrogen from sustainable sources. There are currently a few options for producing hydrogen commercially. The two main options are steam reforming of natural gas, and electrolysis of water. Steam reforming of natural gas required very high temperatures in the order of 700 °C,¹⁰ making it a very energy inefficient process, and it is also reliant on a finite resource. Electrolysis of water holds more potential as a method for green hydrogen production as the electrical energy can come from a sustainable source. Electrolysis requires temperatures of only 50-80 °C, however, the most efficient electrolyzers rely on platinum group metals to function.¹¹ Reliance of a hydrogen based economy on expensive rare metals such as platinum would result in massive geo-political inequalities due to uneven distribution of rare metals in the earth's crust.⁴

A possible solution to this challenge is the use of iron. Iron is one of the most abundant element in the Earth's crust. It follows that an iron based catalyst would be a sustainable candidate for electrochemical hydrogen production.¹² Iron is present in many enzymes in nature, and we can draw inspiration from these enzymes. Of particular interest are the hydrogenase enzymes and their related synthetic molecular mimics; the focus of this thesis.

1.1 Hydrogenases

There are three main classes of the hydrogenase enzyme; [NiFe], [Fe], [FeFe] hydrogenase. All classes are based on earth abundant metals, making the hydrogenase enzymes ideal to study for renewable hydrogen production as an alternative to the methods of hydrogen production described above.¹³

[NiFe] and [FeFe] hydrogenases interconvert protons and hydrogen (eq 1.1).



Equation 1.1 Chemical reaction scheme for interconversion of protons and hydrogen.

Hydrogenases have been thoroughly reviewed by Lubitz *et al*,¹⁴ and more recently by Apfel *et al*¹⁵ but in summary the structures are as follows:

1.1.2 [NiFe]-hydrogenases

Although nickel-iron hydrogenases, from here on referred to as [NiFe]-H₂ase, favour hydrogen oxidation, they are additionally capable of proton reduction. [NiFe]-H₂ases consist of two protein subunits.¹⁶ The small subunit generally has a molecular weight of 29 kDa, and contains the [Fe₄S₄]-clusters that form the electron transport chain necessary for catalysis. [Fe₄S₄]-clusters are able to accept or donate electrons, and when multiple clusters are present, they are

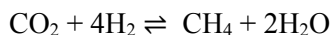
able to form electron transport chains which allows electrons to be transported over long distances (i.e. $>15 \text{ \AA}$) from the surface of a protein to the catalytic site. The second subunit, the large subunit, has a molecular weight of 63 kDa and houses the [NiFe] active site. Some [NiFe]-H₂ases contain more protein subunits, but that is beyond the scope of this thesis. The active site of the [NiFe]-H₂ase contains an iron ion and a nickel ion bound via two bridging cysteine thiolato units, and an X-type ligand.¹⁷ The iron is additionally bound to a carbonyl ligand and two cyanide ligands. The nickel is bound to two further cysteine thiolato sulfur atoms, and also contains a vacant coordination site (figure 1.1 panel A).¹⁸

The mechanism of proton-hydrogen interconversion by [NiFe]-H₂ases is not fully established. A 2004 study from Dementin *et al* investigated the proton transfer pathway in the [NiFe]-H₂ase isolated from *Desulfovibrio fructosovorans*. After hydrogen is split to electrons and protons, the proton is transferred from one of the terminal cysteines (cys-72) on the nickel site of the cofactor to the nearby glutamate residue (glu-25).¹⁹ From here, there are two hypotheses. Either the protons are transported to a groove in the protein surface via glutamate residues (glu-25, glu-16 and glu-46), or the protons travel from glu-25 via a pathway involving transfer along water molecules to the C-terminal histidine (his-549) and then to glu-533 which is close to a magnesium dication that lies close to the protein surface.²⁰ Another hypothesis on the transfer of protons away from the active site, is that the arginine located close to the bridging hydride accepts a proton, facilitating transfer through a histidine rich motif.²¹

Activation of the [NiFe]-H₂ase by reaction with hydrogen results in the formation of the catalytic state Ni-C, which contains a bridging hydride (X = H). One-electron reduction of Ni-C leads to Ni-R which also contains a bridging hydride. A crystal structure of *D. vulgaris* in the Ni-R state shows not only the presence of the bridging hydride, but also the protonated terminal cysteine-thiol. Which means that Ni-R carries the initial products of H₂ splitting.²² Theoretical studies supported the analysis of the crystal structure of Ni-R, but also found several other hydride states, varying only by 10 kcal in energy, that cannot be ruled out as taking part in the hydrogen oxidation reaction. These states are the hydride with a protonated bridging cysteine thiol, or the hydrogen bound side-on to the Ni site.²³

1.1.3 [Fe]-hydrogenases

The iron hydrogenase ([Fe]-H₂ase, figure 1.1 panel B) is different to [NiFe] and [FeFe] H₂ases in several ways. The first is that it is actually one enzyme involved in a series of steps in the methanogenic energy conversion pathway (summarized in equation 1.2).²⁴ The [Fe]-H₂ase is only found in the methanogenic energy conversion pathway of methanogenic archaea.



Equation 1.2 Summary of the methanogenic energy conversion pathway. Hydrogen and carbondioxide are converted to methane and water, or *vice versa*.

The second difference is that the [Fe]-H₂ase does not interconvert H⁺ and H₂, nor is the metal site considered to be redox active during catalysis. Rather it only works in the presence of one specific substrate (methenyltetrahydromethanopterin, Methylene-H₄MPT).²⁵ Finally, the [Fe]-H₂ase does not contain any [Fe₄S₄]-clusters, which are required by redox enzymes for electron transfer, instead direct hydride transfer occurs by heterolytic fission of the dihydrogen bond at the iron centre. The methylene-H₄MPT reversibly accepts the hydride, while a cysteine (cys-173, *Methanococcus aeolicus*) accepts the proton.

The structure of the [Fe]-H₂ase is homodimeric; that is two identical units are bound together in a dimer, and both units contain one cofactor each (figure 1.1; panel B).²⁶ The cofactor Fe-guanylylpyridinol (Fe-GP) has an octahedral geometry, with two coordinated carbonyl ligands, axial and equatorial. Also coordinated is a bridging sulfur from a cysteine in the second axial position, and an X-type ligand in an equatorial position. Finally, a bidentate guanylylpyridinol ligand (GMP) is coordinated to the iron in the two remaining equatorial positions.

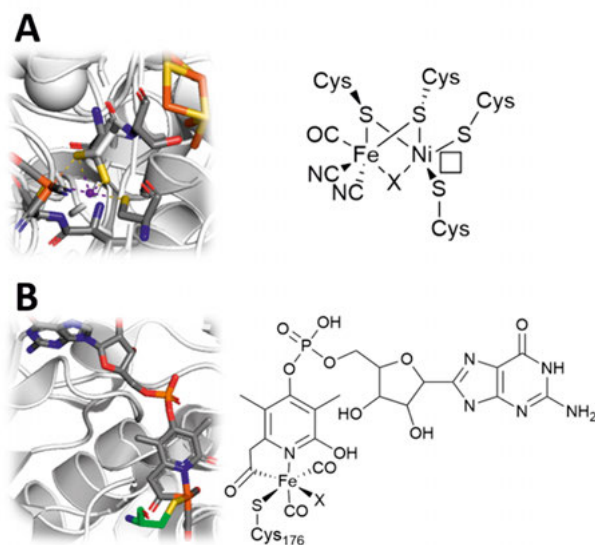


Figure 1.1. Active sites of [NiFe] and [Fe] hydrogenase. **Panel A:** Left, crystal structure of a typical [NiFe]-H₂ase active site, adapted from crystal structure of *E. coli* hydrogenase-1 in its as-isolated form, based on the Protein Data Bank entry 3USE;²⁷ right, chemdraw representation of the active site [NiFe]-cofactor, showing the cysteine ligands that hold the cofactor in the active site pocket. **Panel B:** Left, crystal structure of the active site of an [Fe]-H₂ase (Hmd) holoenzyme from *Methanococcus aeolicus* (open form), based on the Protein Data Bank entry 6HAC;²⁶ right, chemdraw representation of the active site [Fe]-cofactor showing the cysteine holding the cofactor in the active site pocket.

1.2 [FeFe]-H₂ases

The diiron hydrogenase enzyme ([FeFe]-H₂ase, figure 1.2) is the topic of this thesis. The [FeFe]-H₂ase is able to interconvert protons and hydrogen very efficiently, with reported turnover frequencies (TOF) of up to $\sim 10,000\text{ s}^{-1}$.²⁸ Additionally, the presence of carbonyl ligands and cyanide ligands in the [FeFe]-H₂ase active site provide excellent spectroscopic handles for infrared spectroscopy, additional spectroscopic handles for EPR spectroscopy can also be found in the paramagnetic states of the [FeFe]-H₂ase. For these reasons, the [FeFe]-H₂ase is a prime candidate for study of proton reduction to hydrogen gas.

The [FeFe]-H₂ase is a structurally and functionally diverse family of enzymes, however the most simple [FeFe]-H₂ases (CrHydA1, *Chlamydomonas reinhardtii*) contain one subunit with a single domain harbouring the active site (known as the H-cluster). The H-cluster is housed in the active site pocket, which is highly conserved and well characterised among class A-prototypical hydrogenases. It consists of three binding motifs; TSCPxW; MPCxxKxxE; and ExMACxxGCxxGGxP.¹⁴ The H-cluster is a hexairon complex consisting of a [Fe₄S₄]-cluster coupled to the organometallic [FeFe]-cofactor, where the catalytic activity happens. The [Fe₄S₄]-cluster is believed to function as an electron mediator during the turnover, aiding the electron transfer that is vital for catalytic function. The iron centres in the [FeFe]-H₂ase cofactor are low valent, low spin (Fe(I)Fe(II)) in the as matured, resting state, **H_{ox}**. They share a bridging azadithiolate ligand (-SCH₂NHCH₂S-, adt) forming a pendant basic site in the second coordination sphere, and each iron is coordinated by strong field ligands cyanide (CN⁻) and carbonyl (CO). Each iron centre has one CN⁻ ligand, one terminal CO ligand, and they share a bridging carbonyl (μ -CO).^{29,}³⁰ The CO and CN⁻ ligands produce strong vibrational bands in a characteristic region of IR spectra, thus FTIR spectroscopy is an ideal tool for studying [FeFe]-H₂ase. The active site is bound to the protein by only one covalent bond to a cysteinethiol, however multiple weaker interactions also hold the [FeFe]-H₂ase cofactor in place.³¹ The surrounding amino acids interact with the CN⁻ ligands through hydrogen bonds,³² and the CO ligands sit in hydrophobic pockets.

The mechanism of proton reduction/hydrogen oxidation by [FeFe]-H₂ases is under intense investigation and several hypotheses have been put forward into the hydrogenase community.³³⁻³⁵ The proton acceptor during the catalytic cycle is debated; it is either the nitrogen bridgehead, or the [Fe₄S₄]-cluster component of the H-cluster (figure 1.2; left). The presence of a bridging hydride in the enzymes catalytic cycle is also disputed.^{34, 35} Figure 1.3, cycle A shows a cycle put forth by the Lubitz group and subsequently James Birrell *et al*³⁶; Cycle B was developed by Sven Stripp and Michael Haumann (figure 1.4).^{37, 38} Both cycles start from the **H_{ox}** state which has a mixed valent

Fe(I)Fe(II) diiron cluster with a bridging carbonyl and a Fe_4S_4 cluster with a charge of (2+).

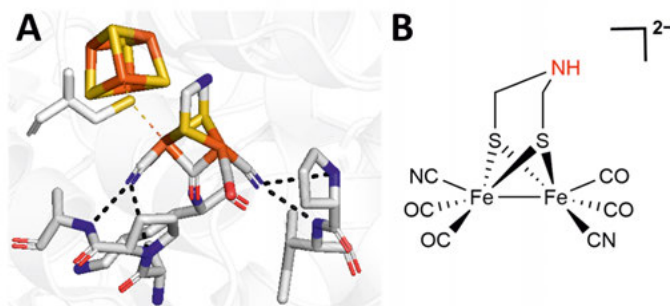


Figure 1.2. The active site of [FeFe] hydrogenase and a synthetic mimic. **Panel A:** Crystal structure of the active site of a typical [FeFe]-H₂ase, adapted from crystal structure of the [FeFe]-H₂ase from *Desulfovibrio desulfuricans* in the H_{inact} state in the Protein Data Bank entry 6SG2,³⁹ the only covalent bond holding the cofactor in the active site pocket is provided by a cysteine bridging the cofactor and the [Fe₄S₄]-cluster. Hydrogen bonds also hold the cofactor in the active site pocket, and these are indicated by black dashed lines. **Panel B:** Chemdraw depiction of a synthetic [FeFe]-cofactor mimic (Fe(I)Fe(I)), which can be used to activate (or “mature”) the apo-enzyme. Upon maturation, one terminal carbonyl ligand is lost, and the cofactor adopts the rotated structure with the bridging carbonyl shown in the left panel. As matured the [FeFe]-H₂ase cofactor is in the H_{ox} state with oxidation states Fe(I)Fe(II).

Cycle A

Cycle A was developed by several groups, and is frequently updated with most new data coming from the Lubitz group in Mulheim, Germany. The cycle shown in figure 1.3 is adapted from the latest proposed mechanism at the time of writing.⁴⁰ In the first step **H_{ox}** is reduced at the [Fe₄S₄]-cluster such that the [Fe₄S₄]-cluster has a (1+) charge, and the bridging carbonyl (μ -CO) becomes “semi-bridging”, forming **H_{red}**. **H_{red}** is then protonated at the nitrogen bridgehead to form **H_{red}H⁺**, the charge of the [Fe₄S₄]-cluster returns to (2+) and the oxidation states of the [FeFe]-H₂ase cofactor are reduced from Fe(I)Fe(II) to Fe(I)Fe(I). This species is reduced again at the [Fe₄S₄]-cluster (from (2+) to (1+)) to **H_{sred}H⁺**. Two possible species are proposed to form from **H_{sred}H⁺** upon migration of the proton to the [FeFe]-H₂ase cofactor. One is **H_{hyd:ox}** which has only been observed at cryogenic temperatures and is not thought to take part in the predominant catalytic cycle.⁴¹ The second and more important species is **H_{hyd}** (also denoted **H_{hyd:red}** in some publications). **H_{hyd}** is a hydride state, in which the iron ions of the [FeFe]-H₂ase cofactor are in oxidation states Fe(II)Fe(II), with a fully bridging carbonyl and (1+) charge on the [Fe₄S₄]-cluster. **H_{hyd}** is protonated at the nitrogen bridgehead to make **H_{hyd}H⁺** and the [FeFe]-H₂ase cofactor is reduced to Fe(I)Fe(II) while the [Fe₄S₄]-cluster is oxidized to (2+). The proton migrates from the bridgehead to the hydride to form hydrogen near the [FeFe]-H₂ase cofactor, **H_{ox}-H₂**. H₂ then leaves the active site, regenerating **H_{ox}**.

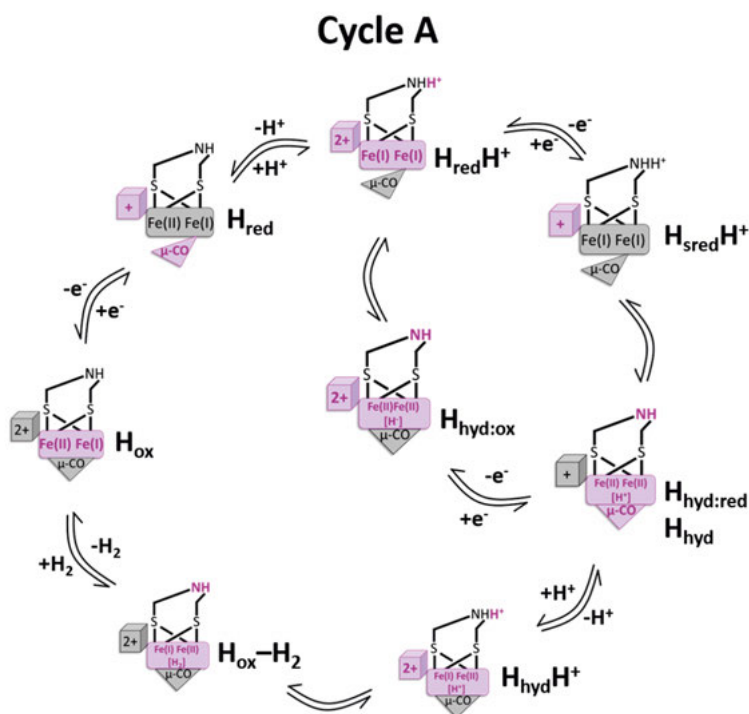


Figure 1.3. Cycle A: the two pathway cycle proposed by Lubitz and further built upon by Birrell and co-workers.⁴⁰ Starting from \mathbf{H}_{ox} , left. Pink is used to highlight the components of the H-cluster that are changed relative to the preceding state. The cubes denote the $[\text{Fe}_4\text{S}_4]$ -cluster which cycles between (1+) and (2+) during catalysis. The rectangles represent the $[(\text{CO})(\text{CN})\text{Fe}-\text{Fe}(\text{CN})(\text{CO})]$ component of the H-cluster, which cycles between $\text{Fe}(\text{II})_2$ and $\text{Fe}(\text{I})_2$ during the catalysis, sometimes taking on a terminal hydride (as in the \mathbf{H}_{hyd} states). The triangles denote a bridging or semi-bridging carbonyl depending on if the triangle is fully in contact with the H-cluster or just in contact by one corner respectively.

Cycle B

Cycle B, originally proposed by Stripp and Haumann, consists of two cycles, the fast and the slow cycle.³⁴ Starting from \mathbf{H}_{ox} , it enters the fast cycle. It is protonated and reduced through proton coupled electron transfer (PCET) at the $[\text{Fe}_4\text{S}_4]$ -cluster so that the $[\text{Fe}_4\text{S}_4]$ -cluster is protonated and has an overall charge of (1+), this species is \mathbf{H}_{red}' . \mathbf{H}_{red}' may then either enter the slow cycle, or continue in the fast cycle by undergoing a second PCET step to form \mathbf{H}_{hyd} . In this intermediate (\mathbf{H}_{hyd}), the protonated $[\text{Fe}_4\text{S}_4]$ -cluster remains the same as in \mathbf{H}_{red}' , but the $[\text{FeFe}]$ - H_2 ase cofactor has gained a terminal hydride and has been (formally) oxidized from $\text{Fe}(\text{I})\text{Fe}(\text{II})$ to $\text{Fe}(\text{II})\text{Fe}(\text{II})$. Following this, \mathbf{H}_{hyd} reacts with a proton to give hydrogen and $\mathbf{H}_{\text{ox}}\mathbf{H}$ which is deprotonated once more to regenerate \mathbf{H}_{ox} and close the cycle. As mentioned above, cycle B also contains a slow cycle that starts at \mathbf{H}_{red}' . \mathbf{H}_{red}' loses the hydride associated

with the $[\text{Fe}_4\text{S}_4]$ -cluster, and gains a proton which actually forms a bridging hydride on the $[\text{FeFe}]$ -H₂ase cofactor to form **H_{red}**. **H_{red}** has a $[\text{Fe}_4\text{S}_4]$ -cluster with charge (2+), and the oxidation states of the $[\text{FeFe}]$ -H₂ase cofactor are Fe(II)Fe(II). In cycle B, **H_{red}** does not contain a μ -CO ligand. The formation of the bridging hydride requires a structural change in the complex, hence the slowness of the cycle. **H_{red}** is then reduced to **H_{sred}**, in which the $[\text{Fe}_4\text{S}_4]$ -cluster has (1+) charge. To close the slow cycle, **H_{sred}** must be protonated to form **H_{hyd}**, and rejoin the fast cycle, this step also requires some structural reorganization.

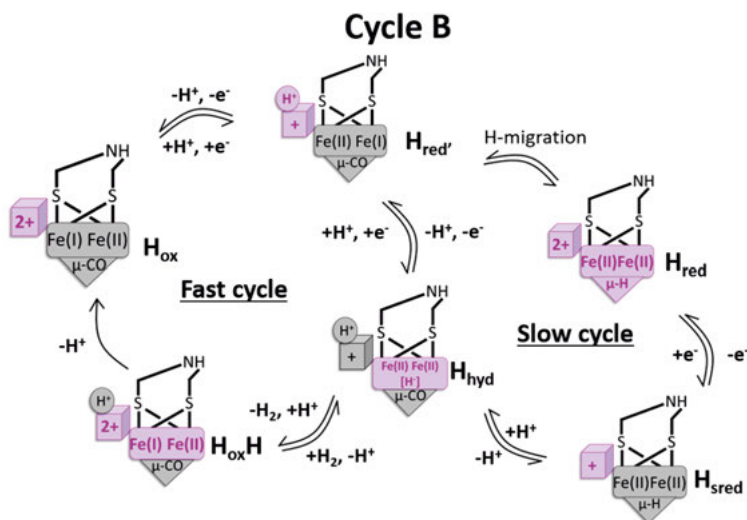


Figure 1.4. Cycle B, the double cycle proposed by Haumann and Stripp. Starting from **H_{ox}**, left. Pink is used to highlight the components of the H-cluster that are changed relative to the preceeding state. The cubes denote the $[\text{Fe}_4\text{S}_4]$ -cluster which cycles between (1+) and (2+) during catalysis, sometimes accepting a proton, as in the **H_{red}'** state (top middle). The rectangles represent the $[(\text{CO})(\text{CN})\text{Fe}-\text{Fe}(\text{CN})(\text{CO})]$ component of the H-cluster, which cycles between Fe(II)Fe(I) and Fe(II)Fe(II) during the cycle, sometimes taking on a bridging hydride, as in the **H_{red}** and **H_{sred}** states. The triangles denote a bridging ligand.

1.3 Artificial maturation

Usually the $[\text{FeFe}]$ -H₂ase requires a cascade of maturation enzymes in order to fully assemble.⁴²⁻⁴⁹ However, the $[\text{FeFe}]$ -H₂ase enzyme can be artificially matured using a close structural $[\text{FeFe}]$ -H₂ase cofactor mimic.⁵⁰ Arguably the closest mimic is $[\text{Fe}_2(\mu\text{-adt})(\text{CO})_4(\text{CN})_2]^{2-}$ (**2b²⁻**, figure 1.2, panel B), which, upon insertion into the empty active site pocket (apo-HydA) through artificial maturation binds to the $[\text{Fe}_4\text{S}_4]$ -cluster, loses one carbonyl ligand, and adopts a rotated structure, such that the two iron centres share a μ -CO ligand.^{51, 52} It is believed that $[\text{Fe}_2(\mu\text{-adt})(\text{CO})_4(\text{CN})_2]^{2-}$ decomposes when the cyanide ligands are exposed to protons, and this decomposition pathway has

been investigated by Zhang *et al* and shown to form $[\text{Fe}_6(\{\text{SCH}_2\}_3\text{N})_2(\text{CO})_{17}]$ through a self-condensation pathway.⁵³⁻⁵⁵ Despite this reactivity, when inserted into apo-HydA $[\text{Fe}_2(\mu\text{-adt})(\text{CO})_4(\text{CN})_2]^{2-}$ becomes as active as the native enzyme, highlighting the importance of an outer coordination sphere for the function of the $[\text{Fe}_2(\mu\text{-adt})(\text{CO})_4(\text{CN})_2]^{2-}$ mimic.⁵⁰

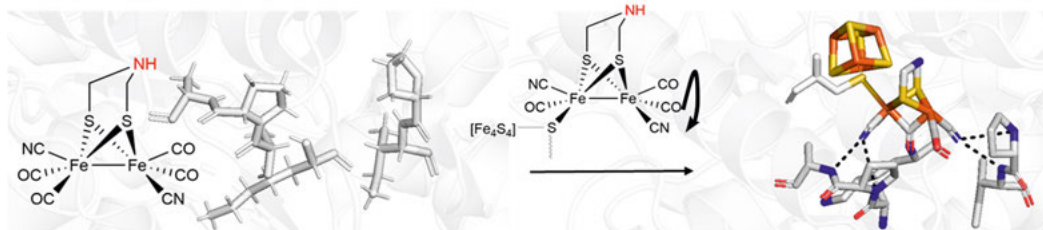


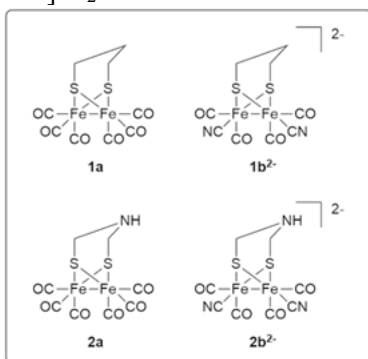
Figure 1.5. Schematic diagram showing artificial maturation of apo-HydA. During this process, the cofactor ($2\mathbf{b}^{2-}$) loses a carbonyl ligand, and adopts a rotated structure inside the active site pocket.

The active site pocket provides an outer coordination sphere vital for the activity of the $[\text{FeFe}]\text{-H}_2\text{ase}$ cofactor. Likewise chapter 4 (paper II) will present research that further supports the importance of the outer coordination sphere through the synthesis and study of a miniaturized hydrogenase.⁵⁶ It is well established that the CN^- ligands of mimics react with protons under catalytic conditions resulting in decomposition.⁵³ Chapter 5 (paper (III)) will present my project on borane protected hydrogenase mimics, which even further underscores the importance of the outer coordination sphere.⁵⁷

1.4 Structural mimics of the H-cluster

$[\text{FeFe}]\text{-H}_2\text{ases}$ have extremely high potential for biotechnological applications; and due to their high hydrogen production activity and the high abundance of iron in the Earth's crust, it is necessary to understand the enzyme's mechanism, so that hydrogenases or their mimics can be optimized to engineer the best proton reduction or hydrogen oxidation catalysts. Consequently, the scientific literature is rich with $[\text{FeFe}]\text{-H}_2\text{ase}$ cofactor mimics.⁵⁸⁻⁶⁶ Mimics aid understanding of the hydrogenase mechanism by providing simple and easily modifiable systems for study of hydrogen production that are sometimes easier to study by spectroscopy than the native enzymes. Model complexes also aid in computational investigations of the hydrogenase,³³ and in rationalizing some of the spectroscopy.⁶⁷ Synthetic complexes offer diverse design pathways towards the development of novel proton reduction or hydrogen oxidation catalysts. A well characterized structural $[\text{FeFe}]\text{-H}_2\text{ase}$ cofactor mimic is the propanedithiolato bridged complex $[\text{Fe}_2(\mu\text{-pdt})(\text{CO})_4(\text{CN})_2]^{2-}$ ($1\mathbf{b}^{2-}$, scheme 1.1).^{53, 54, 68} $1\mathbf{b}^{2-}$ is a low valent (Fe(I)Fe(I)) low spin complex consisting of a Fe_2S_2 core, with C_{2v} symmetry. In addition to the propanedithiolato

ligand, the iron ions are coordinated by four carbonyl ligands and two cyanide ligands, all of which are strong field ligands. The previously mentioned complex $[\text{Fe}_2(\mu\text{-adt})(\text{CO})_4(\text{CN})_2]^{2-}$ (**2b**²⁻, figure 1.9), reported already in 2002^{69, 70}, is highly similar to **1b**²⁻, but it has an amine bridgehead, which forms a pendant base, instead of a methylene bridgehead as in pdt. Compound **1b**²⁻ is often preferred by synthetic chemists because it is more robust than the mimic with the nitrogen bridgehead, and it exhibits much simpler protonation chemistry. However, the $[\text{FeFe}]$ -H₂ase cofactor in the native enzyme is known to have a nitrogen bridgehead, so **2b**²⁻ is considered the most structurally biomimetic model complex. Developing synthetic protocols that works for this group has formed a large part of my PhD, so it seems important that a full explanation of my experiences with these two $[\text{FeFe}]$ -H₂ase cofactor mimics and their related hexacarbonyl precursors is included in the thesis. The synthetic routes to **1b**²⁻ and **2b**²⁻ are therefore described in appendix 1. In the coming pages I will discuss some illustrative $[\text{FeFe}]$ -H₂ase cofactor mimics from the literature. Additionally I will briefly discuss some hydrogen production/oxidation catalysts that are inspired by the $[\text{FeFe}]$ -H₂ase, but do not structurally resemble the $[\text{FeFe}]$ -H₂ase cofactor.



Scheme 1.1. Four simple but well studied examples of $[\text{FeFe}]$ -H₂ase cofactor mimics.

1.4.2 Fe based mimics

The scientific literature is rich with $[\text{FeFe}]$ -H₂ase cofactor mimics.^{59, 61, 64}

Three major considerations for hydrogenases and their mimics of particular relevance to this thesis are:

1. Both the mimics and the hydrogenases found in nature are oxygen sensitive (explored more in chapter 3, paper I)⁷¹
2. Under catalytic conditions, the cyanide ligands of the model complexes are attacked by protons leading to degradation (Chapter 5, introduction of a synthetic outer coordination sphere).⁵⁷

3. The electron density on the iron atoms of the diiron cofactor can be adjusted through introduction of electron withdrawing/donating ligands, electron mediators in the outer coordination sphere (chapter 4),⁵⁶ or by changing the metal itself (chapter 6).

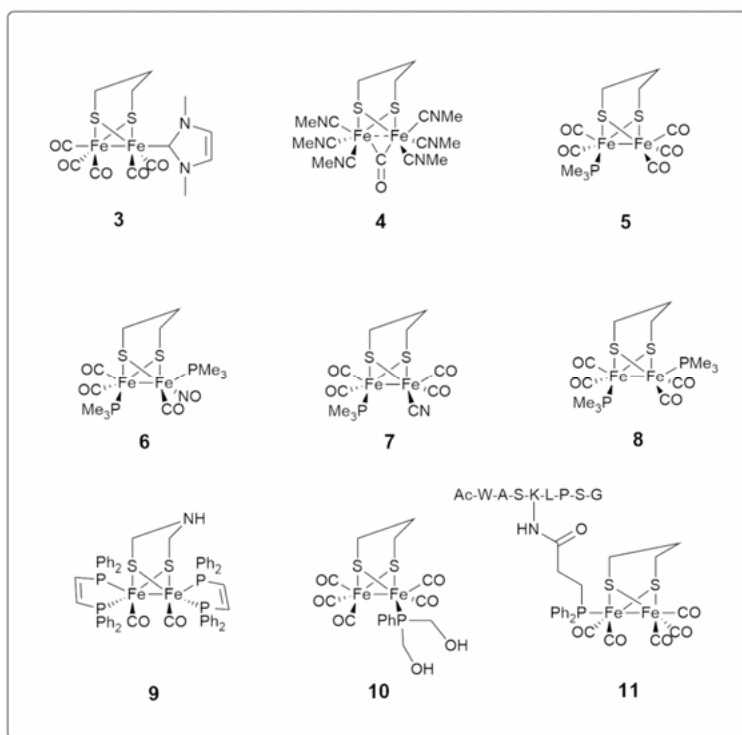
Here I discuss some important and relevant proton reduction catalysts from the literature. Many of which were inspired by or even mimic the [FeFe]-H₂ase. There are several aspects of the H-cluster that can be mimicked; the carbonyl ligands; the bridgehead; the [Fe₄S₄]-cluster; and the metal centres themselves.

Cyanide ligands, while biomimetic, are ambidentate which complicates the proton reduction/hydrogen oxidation chemistry of diiron dithiolato carbonyl complexes. This is why cyanide ligands are often substituted for other ligands with comparable σ -donating capacity. Examples of σ -donating ligands that have been utilized in ligand substitution on diiron dithiolato carbonyl complexes are carbenes,⁷² isonitriles⁷³ and nitrosyls (scheme 1.2, complexes **3-6**).⁷⁴ Tertiary phosphines are another example of σ -donating ligands that are widely used as alternatives to cyanide ligands and they are extensively used to develop novel catalysts due to their diverse chemistry. They have also been dubbed as the synthetic chemists alternative to cyanide ligands.⁷⁵

Examples of phosphine substituted complexes are shown in scheme 1.2. Complex **6** is an asymmetric [FeFe]-H₂ase mimic that contains two phosphine ligands in addition to a nitrosyl ligand.⁷⁴ The nitrosyl ligand actually has a remarkable effect on the reduction potential of the complex, which is -0.88 vs SHE (reported as -0.67 vs Ag|AgCl), this is much more positive than the diphosphine lacking a nitrosyl ligand, complex **8**, which has reduction potential at the very unfavorable potential of -1.85 V vs SHE.^{76,77} The very negative potential of complex **8** is the result of the highly σ -donating nature of the phosphine ligands, which is apparently counteracted by the electron withdrawing nitrosyl ligand of complex **6**. Furthermore, the asymmetric monophosphine monocyanide, **7**, first synthesised in 2001 by Gloaguen *et al*, shows an even more negative reduction potential of -2.34 vs SHE (reported as -2.14 V vs Ag|AgCl).⁷⁸ This reflects the σ -donating nature of both the cyanide and the phosphine. Despite the very unfavourable reduction potential of **7**, the asymmetry provides an interesting biomimetic aspect because the [FeFe]-H₂ase cofactor in the enzyme is also in an asymmetric environment caused by ligation to the [Fe₄S₄]-cluster.

The tertiary phosphines are really diverse ligands as illustrated by complexes **9-11**. Complex **9** shows how two bidentate phosphine ligands (dppv, *cis*-C₂H₂(PPh₂)₂) coordinate to the iron centres of an [FeFe]-H₂ase mimic.^{79, 80} The complex reduced protons at very negative potentials, just like the other phosphine substituted [FeFe]-H₂ase cofactor mimics, -2.28 V vs SHE (reported as -1.64 V vs Fc^{+/0} in MeCN). However, complex **9** is very unusual because of its rich hydride chemistry. Depending on the pK_a of an acid in

MeCN, and the temperature, complex **9** may form a bridging hydride (weak acid, 0 °C) or a terminal hydride (stronger acid, -40 °C). Bridging hydrides are very common products of protonation among [FeFe]-H₂ase cofactor mimics, however terminal hydrides are less frequently reported,⁶⁴ which makes complex **9** rather rare. Furthermore, terminal hydrides are considered as key intermediates in proposed catalytic cycles of proton reduction/hydrogen oxidation by [FeFe]-H₂ases (figures 1.3 and 1.4). For this reason, the presence of terminal hydrides in synthetic mimics of the [FeFe]-H₂ase cofactor is particularly interesting.



Scheme 1.2. Examples of [FeFe]-H₂ase mimics in which the carbonyl ligand has been replaced with more electron donating ligands.

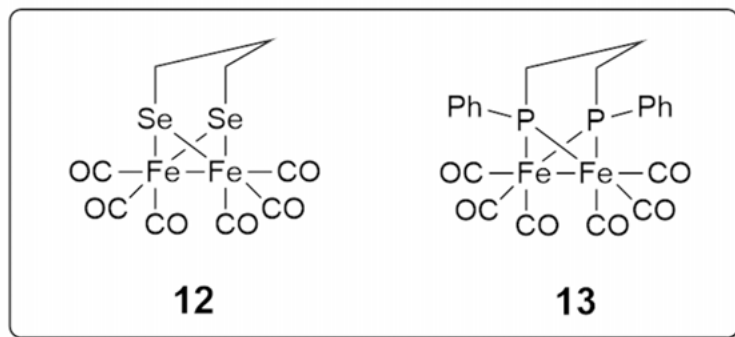
Complex **10** is another example of a [FeFe]-H₂ase mimic that takes advantage of the diverse modifications that can be made on phosphine ligands. The -OH groups make it soluble in water. A phosphine functionalized peptide has been used to incorporate an outer coordination sphere into a [FeFe]-H₂ase mimic. Roy *et al* have produced four diiron-phosphino-peptides that exhibit electrocatalytic proton reduction from acetic acid in the presence of water, complex **11**. In acetonitrile, a catalytic current is observed at -2.74 vs SHE (reported as -2.1 V vs Fc^{+/0} in MeCN). While in an acetonitrile/water solvent mixture the reduction potential is pushed to less reducing potentials by a value between

100–150 mV. This system is exciting because it allows for the synthesis of a diverse range of mimics by incorporating other peptides/artificial peptides to adapt the outer-coordination sphere. The incorporation of peptides induces water solubility, which in the future could serve as both a solvent and a substrate.⁸¹

The activity of [FeFe]-H₂ase cofactor mimics (and that of a semi-synthetic enzyme) is influenced by the bridging ligand of the [FeFe]-H₂ase cofactor mimic, as will be explored further in chapter 3. There are two major places where the bridging ligand can be modified, and that is the thiolato group (scheme 1.3) and more commonly the bridgehead group (scheme 1.4).

Compound **12** was synthesised by the reaction of Fe₃(CO)₁₂ with 1,3-diselenocyanato propane. The IR spectrum shows carbonyl bands at 2064 cm⁻¹, 2026 cm⁻¹ and 1988 cm⁻¹. The reduction chemistry was not reported.⁸²⁻⁸⁴

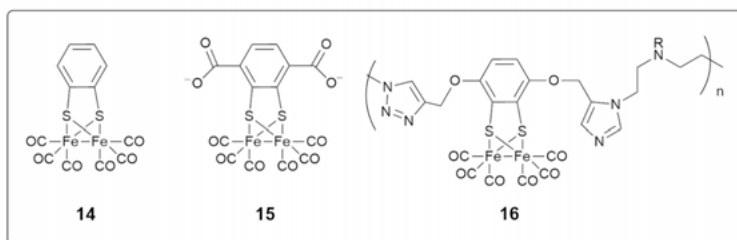
Complex **13** was first synthesised in 1982,⁸⁵ and electrochemically characterized in 2007.⁸⁶ Complex **13** is reduced at -1.76 V vs SHE (reported as -1.52 V vs SCE). IR spectroelectrochemistry and CV simulations were used to identify intermediates and the authors of that study found that electrocatalytic proton reduction of **13** follows a shared reaction path with **1a**. Computational studies on this compound by Arrigoni *et al* revealed some guidelines for the rational design of diiron complexes with Fe₂P₂ cores, like **13**, that should enable control of redox potential inversion.⁸⁷



Scheme 1.3. Chemdraw depictions of complexes in which the thiols of the bridging ligand are replaced. **12** is an example of a [FeFe]-H₂ase cofactor mimic in which the bridging sulfurs of the bridging ligand have been replaced with selenium; **13** is an example in which the sulfurs have been replaced with phosphorous.

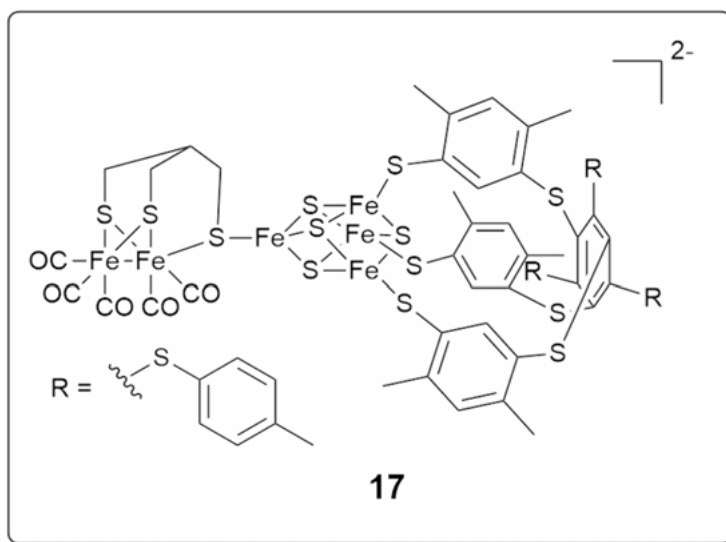
Complex **14** can be synthesised by reaction of Fe₂(CO)₉ with benzene-1,2-dithiolate.⁸⁸ The electrochemistry of **14** was later characterized and revealed a reduction potential at -1.97 V vs SHE (reported as -1.33 V vs Fc^{+/0}).⁸⁹ The complex was also studied for photoinduced proton reduction and intermediates were observed directly through time resolved IR and UV-vis spectroscopy, one of these intermediates was assigned as a bridging hydride.⁹⁰ Compound **15** has a reduction potential at -1.87 V vs SHE (reported as -1.23 V vs Fc^{+/0}).^{91, 92} **15** has been used as a linker in metal organic frameworks (MOFs)

by post synthetic exchange. The MOF it produces is capable of photocatalytic hydrogen production. Investigations on these MOFs have identified important considerations that should be taken into account when investigating MOFs with redox active linkers. Bridgehead ligands have also been adapted to enable incorporation into polymers. In the case of polymer **16** the reduction potential is -2.8 vs SHE (reported as -1.8 Vs Ag|AgCl). The integrity of the cofactor in the polymer is shown by FTIR. However the authors of that study suggest that the polymer decomposes at these highly reducing potentials.⁹³



Scheme 1.4. Examples of [FeFe]-H₂ase mimics featuring benzene di-thiolate bridging ligands.

In 2005, the first free-standing H-cluster mimic was synthesised in order to enable understanding of how the interaction between the [Fe₄S₄]-cluster and the [FeFe]-cofactor enables catalysis (**17**, scheme 1.5).⁶⁸ A cofactor mimic composed of dithiolate containing a carbon bridgehead, and thioester group was synthesised. This was subsequently coupled to a pre-formed [Fe₄S₄(L)(SEt)]²⁺ cluster, where L is 1,3,5-tris(4,6-dimethyl-3-mercapto-phenylthio)-2,4,6-tris(p-tolyl-thio)benzene, (scheme 1.5) and it is vital for the formation of the [Fe₄S₄]-cluster. L blocks three of the Fe ions, and leaves one free for coupling to the [FeFe]-cofactor through the formation of a (μ -SR) linkage. This bond holds the two segments together, and provides for electronic communication between the two components. Cyclic voltammetry experiments showed the half-wave reduction potential of this system to be $E_{1/2} = -1.06$ V vs SHE (reported as $E_{1/2} = -0.86$ V vs Ag|AgCl in DCM). The parent cluster ([Fe₄S₄(L)(SEt)]²⁺) has $E_{1/2} = -1.18$ V vs SHE (reported as $E_{1/2} = -0.98$ V vs Ag|AgCl in DCM). The system reduces protons at $E_{p,c} = -1.33$ V vs SHE (reported as $E_{p,c} = -1.13$ V vs Ag|AgCl).⁶⁸



Scheme 1.5. Chemdraw depiction of the synthetic freestanding H-cluster mimic

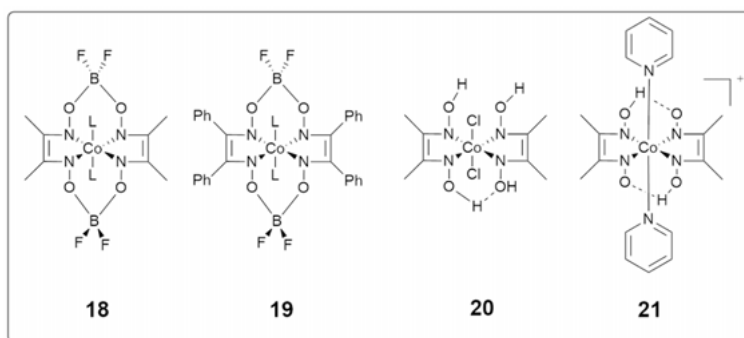
A new approach to synthesizing a free-standing H-cluster was taken in 2019.⁵⁶ A synthetic maquette derived from *Peptococcus aerogenes* Ferredoxin 1 (FdM) that contains four cysteine residues capable of binding to Fe to produce a $[\text{Fe}_4\text{S}_4]$ -cluster.⁹⁴ The cofactor mimic reacts with the reduced $[\text{Fe}_4\text{S}_4]$ -cluster to form the H-cluster, encased in the ferredoxin derived oligopeptide. This work was supported by EPR, UV-Vis, and FTIR spectroscopy, as well as deoxyhemoglobin assays, and DFT calculations. The hydrogen evolution activity was determined by reaction with reduced methylviologen, meaning that the reduction potential must be below -0.45 V vs SHE (reduction potential of methyl viologen⁹⁵). The turnover number in 1 hour was 10. Nevertheless, this is a great example of a minaturised H-cluster, and the structure remains very close to that of the H-cluster inside the enzyme. Further work can be done by changing the peptide design, thus editing the outercoordination sphere. This will be discussed more in chapter 4.

1.5 Other proton reduction catalysts

Other proton reduction catalysts include cobaloxime (based on cobalt), molybdenum-sulfur dimers and the DuBois catalyst (based on nickel).

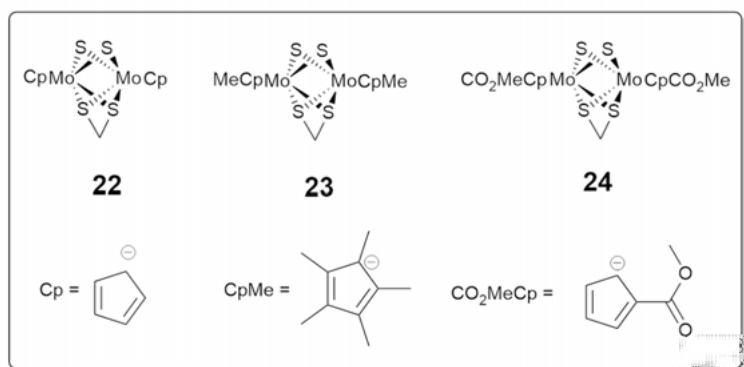
Cobaloximes were first reported in 1986 by Connolly and Espenson (scheme 1.6 complex **18**), and demonstrated proton reduction in the presence of a strong reductant (i.e. Cr(II) , Eu(II) , V(II)).⁹⁶ Complex **18** was later characterized electrochemically and shown to reduce protons in the presence of

acid at -0.79 V vs SHE (reported as -0.55 V vs SCE in MeCN). Variations of the glyoxime ligands have allowed tuning of electron density and therefore the redox potential. For example substituting the methyl groups for phenyl groups (as in complex **19**) enabled the reduction potential to shift to -0.52 V vs SHE (reported as -0.28 V vs SCE in MeCN). The axial ligands may also be modified (scheme 1.6, complexes **20** and **21**). And these complexes have served as good catalysts for the demonstration/illustration of some relevant electrochemical principles, for example, Rountree et al used complex **18** to study the relationship between the log of the global rate constant of catalysis and the pK_a of acid. They additionally carried out foot of the wave analysis (FOWA) to determine k_1 of an ECEC' proton reduction mechanism (see section 2.4.3 for more details on EC notation).⁹⁷⁻⁹⁹



Scheme 1.6. Chemdraw representations of cobaloxime based proton reduction catalysts.

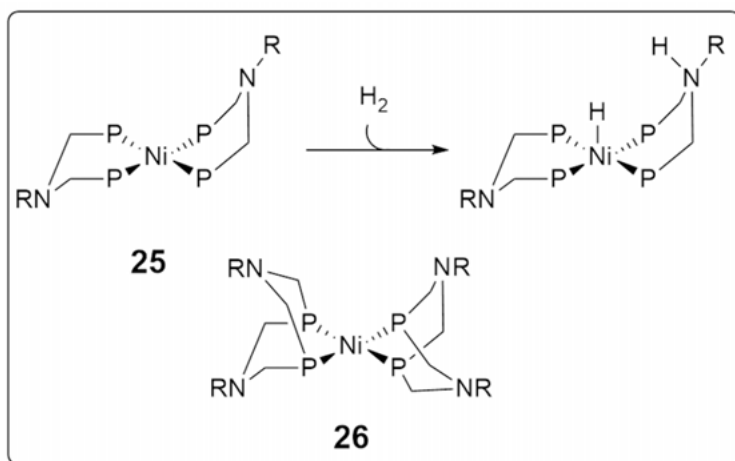
Another example of proton reduction catalysts not based on iron is the molybdenum dimer complexes shown in scheme 1.7. The electrocatalytic proton reduction activity of molybdenum sulfur dimers was reported by Appel and Dubois in 2005.¹⁰⁰ They demonstrated that these molybdenum dimers operate at -0.12 V vs SHE (reported as -0.65 V vs $Fc^{+/0}$ in MeCN) (complex **22**). The electron density on the metal centres was tuned by adjusting the substituents on the cyclopentadienyl ligands (complexes **23** and **24**). While this did result in new CV traces, only very small catalytic current was observed in the presence of acid.



Scheme 1.7. Chemdraw representations of molybdenum based proton reduction catalysts

DuBois' more famous complex for hydrogen production/oxidation, the DuBois catalyst, is a functional mimic of the hydrogenase enzyme. It has a square-planar Nickel centre, bound by two bidentate phosphine ligands (bis(diethylphosphineomethyl)methylamine, PNP). This ligand contains an amine group in the outercoordination sphere, similarly to the amine bridgehead in the [FeFe]-H₂ase, forming a six-membered ring when bound to the nickel ion. Similar complexes were also synthesised using an eight-membered cyclic ligand in order to incorporate further pendant amine groups in the complex.

Reaction of these complexes with hydrogen forms a new complex in which a hydride is bound to the nickel centre and a proton is bound to one of the pendant amine bases (Scheme 1.8, complexes **25** and **26**).¹⁰¹ Studies of the DuBois complexes demonstrated the importance of an amine bridgehead for hydrogen production/oxidation 10 years before the presence of the amine bridgehead in the native enzyme was confirmed.^{102, 103} The complexes have primarily been investigated for hydrogen oxidation rather than proton reduction, and complex **25** demonstrated catalytic oxidation of hydrogen at -1.51 V vs SHE (reported as -0.87 V vs Fc^{+/0}).



Scheme 1.8. Chemdraw representations of the DuBois catalyst for hydrogen oxidation. **25** reacts with molecular hydrogen to form a hydride. **26** is an example containing multiple pendant amines in the outer-coordination sphere.

1.6 Solid state catalysts for hydrogen production

Hydrogen evolution is also possible using solid state catalysts. For the simplest solid state catalysts, monometallic solids, precious metals display optimal intrinsic hydrogen evolution reaction catalysis as exemplified by the volcano plot in figure 1.6.¹⁰⁴ In the case of hydrogen evolution, the volcano plot is a graph showing the relationship between the log of the exchange current density ($j_0/\text{A cm}^2$) against the M-H bond strength ($E_{\text{M-Hads}}/\text{kcal mol}^{-1}$ or kJ mol^{-1}), which gives an indication of the Gibbs energy of adsorption (ΔG_{ads}). According to Sabatier's principle, in general, the peak of the volcano plot is where $\Delta G_{\text{ads}} \approx 0$ and therefore where catalysis will not be limited by adsorption/desorption of substrate,¹⁰⁵ as with all models, there are limits to this analysis, but I will not discuss them here. In the case of monometallic electrodes for hydrogen evolution, the volcano plot peaks around platinum, rhodium and iridium (platinum group metals, PGM). Unfortunately the high cost, rarity and poor geographical distribution of Pt, Rh and Ir prohibits them from widespread use in devices for hydrogen production.

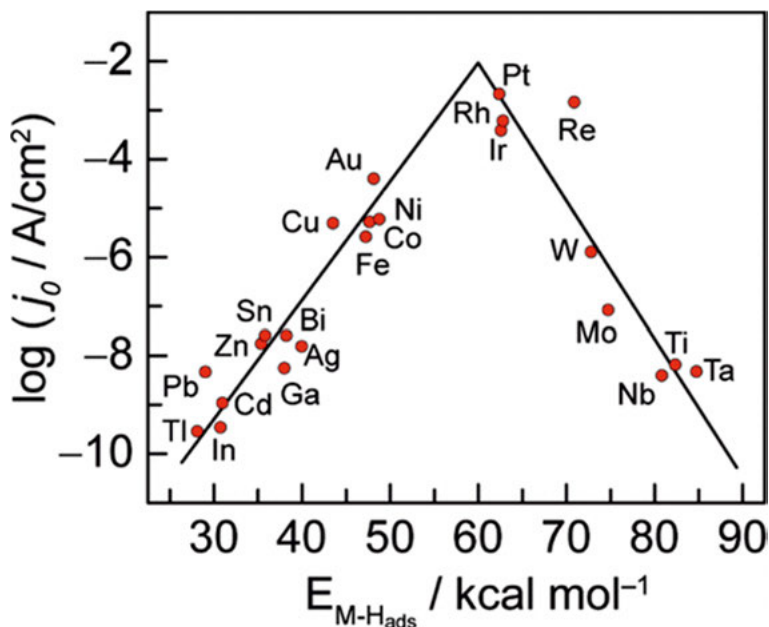


Figure 1.6. Volcano plot comparing the relationship between the metal hydrogen binding energy and the exchange current density of the transition metals. Reproduced from reference ¹⁰⁶ and ¹⁰⁴ with permission from the American Chemical Society and Elsevier.

The clear disadvantage of earth abundant metals in solid state hydrogen evolution, shown in the volcano plot, has been addressed by the development of multimetallic alloys.¹⁰⁶ One such example is a nanoporous copper-titanium bimetallic catalyst (np-Cu_{100-x}Ti_x, where $x = 1, 3, 5, 7$ or 9). By varying the titanium content and using a dealloying process, to leach out aluminium and create a high surface area, it was possible to create a solid state catalyst with hydrogen evolution activity close to a commercially available Pt/C electrocatalyst.¹⁰⁷ Another successful example of increasing the surface area of a solid state catalyst is the dealloying of Ni-Al to form Raney nickel, which exhibits hydrogen evolution activity approaching that of platinum electrodes.¹⁰⁸ A third example of a H₂ producing catalyst based on earth abundant metals is the molybdenum-sulfur based material, MoS₂, in the form of nanoparticles supported on carbon.¹⁰⁹ Since 2005 many different nanostructures of MoS₂ have been generated and shown to be active for hydrogen production.¹¹⁰

1.7 Summary and Aims

In summary, hydrogen as an energy carrier or as a precursor to liquid fuels provides a very promising path towards mitigating climate change. However, there are still challenges to hydrogen production that prohibits its widespread

use today. These challenges include large energy consumption (if not using PGM), high economic cost and the requirement to use rare platinum group metals. [FeFe]-H₂ases could provide a solution to these dilemmas because they are able to produce hydrogen at high turnover frequencies and require iron as the redox active centre. However, the [FeFe]-H₂ases are air sensitive and they are not scalable. Thus, intense research is underway to further understand the enzyme's mechanism and to engineer optimal catalysts for proton reduction. Several mechanisms have been put forth and they are hotly debated. In parallel, synthetic chemists continue to develop complexes that mimic the [FeFe]-H₂ase cofactor either structurally (e.g. **2b**²⁻) or functionally (e.g. **25** and **26**). Development of new catalysts for proton reduction requires understanding the mechanism which cannot be done without the aid of spectroscopic and electrochemical techniques which are utilised in the projects presented in this thesis.

The aims of this thesis are to examine several aspects of the H-cluster from a molecular design perspective, and to investigate the effect of the following on the reactivity of H-cluster and [FeFe]-H₂ase mimics:

- The outer coordination sphere as studied by investigating the bridging dithiolato ligand in chapter 3 (paper I).
- Tuning the electron density on the iron ions in the [FeFe]-H₂ase cofactor mimics. This is addressed in chapters 4 and 5 (papers II and III respectively) through the introduction of a [Fe₄S₄]-cluster as a redox active ligand, and electron withdrawing capping Lewis acid moieties, respectively.
- Protection of the cyanide ligands using a Lewis acid capping moiety, addressed in chapter 5.
- Changing the metal at the centre of the [FeFe]-H₂ase cofactor mimic while maintaining the primary coordination sphere, explored in chapter 6 (paper IV).

These studies required the use of a broad toolbox of characterisation techniques, which I have summarised in the experimental methods chapter.

Chapter 2: Experimental methods

In this section I have summarised some of the techniques used in this thesis to characterise compounds and to investigate catalytic activity.

2.1 FTIR spectroscopy

2.1.1 Harmonic oscillator model and quantized vibrational energy

FTIR stands for fourier transform infrared. FTIR probes the changes in vibrational states of molecules upon exposure to infrared radiation. The fundamental theory of infrared spectroscopy comes from Hooke's laws description of harmonic oscillation. By approximating a chemical bond as a harmonic oscillator (a spring), we can use Hooke's law to relate chemical bonds to vibrational energy levels (figure 2.1). Hooke's law says that if a spring sits at an equilibrium position $x = 0$, the potential energy of that spring (V) will increase with displacement from the equilibrium position (x). A stiff spring will be harder to displace, and so has a high force constant (k_f).^{111, 112}

$$V(x) = \frac{1}{2}k_f x^2$$

Equation 2.1. Potential energy of a harmonic oscillator. It is quadratically related to the displacement from equilibrium (x), and varies linearly with the force constant (k_f) of the harmonic oscillator.

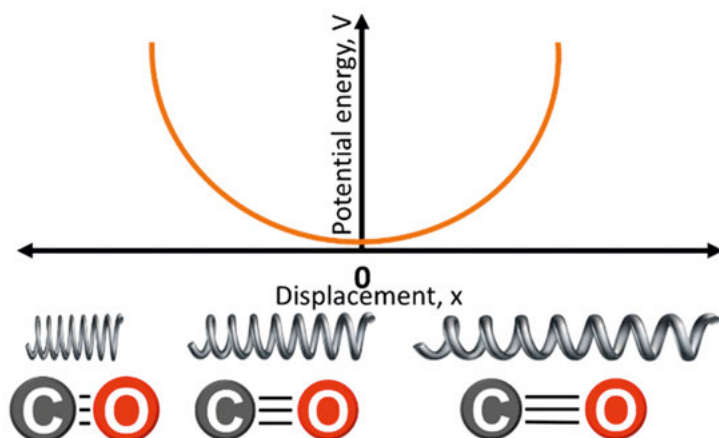


Figure 2.1. Scheme showing the relationship implied by Hooke's law, equation 2.1. The orange line shows how the potential energy of the spring changes with displacement from the equilibrium position (0).

A spring with a specific force constant, k_f , will vibrate at frequency, ω , as in equation 2.2.

$$\omega = \frac{1}{2\pi} \sqrt{\frac{k_f}{\mu}}$$

$$\mu = \frac{m_1 m_2}{m_1 + m_2}$$

Equation 2.2 Vibrational frequency (ω) of a harmonic oscillator. It is related to the square route of the force constant force constant (k_f) and the square route of the reciprocal of the reduced mass (μ), which stems from the two-body problem in Newtonian mechanics.

Where μ is the reduced mass of two objects on either side of the spring.

This spring model is a good model for diatomic molecules, however it does fall short because at an atomic level quantum chemistry takes over. Consequently, the vibrational energies are quantised meaning a molecular bond may only stretch in steps of specific sizes. In addition to this, the concept of $E = 0$ that is implied by the classical harmonic oscillator model does not work on a quantum level because this would violate the uncertainty principle. Repulsion between two nuclei and electrons makes it very difficult to push two atoms together, and if enough vibrational energy is directed into the molecule, the bond will dissociate. The vibrational behaviour of two atoms in a bond is better described using a Morse potential well diagram.

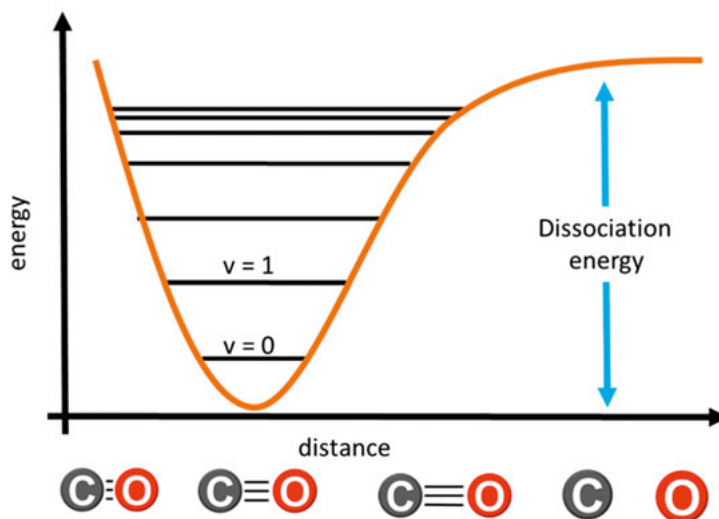


Figure 2.2. Schematic Morse potential well diagram for the diatomic molecule CO. The x-axis shows the distance between the two bodies (carbon atom and oxygen atom), e.g. the displacement from the equilibrium position, the y-axis shows the energy change with the distance. The horizontal lines denote quantised vibrational energy levels. This diagram is described by equation 2.3.

The lowest vibrational state, $v = 0$, does not have zero energy. Instead the energy is given by equation 2.3.

$$E = h\omega(v + 1/2)$$

Equation 2.3. The energy varies with the vibrational frequency and the vibrational energy level (v (not to be confused with ν)) $v = 0, 1, 2, 3, 4 \dots$

Where ν is the vibrational quantum number and depicts the vibrational energy level of the chemical bond. Together these equations tell us that the vibrational energy depends on the mass of the two atoms on either end of the bond (m_n), and on the strength of the bond (force constant, k_f). We can expect heavy atoms held by weak bonds to vibrate at low frequencies, while light atoms held together by strong bonds are expected to vibrate at higher frequencies.

2.1.2 Vibrational modes

A molecule with N atoms has $3N$ degrees of freedom. This is because the position or movement of each atom may be described by the Cartesian coordinates x , y and z . In infrared spectroscopy, we are interested in the movements that cause a change in the bonds or the bond angles within the molecule. Meaning that rotation (around x , y or z) and translation (along x , y or z) does

not contribute to the FTIR signal. Leaving $3N-6$ degrees of freedom for vibrations. If the molecule is linear, there are $3N-5$ degrees of freedom for vibration because rotating around a linear axis (O-C-O of CO₂, for example) does not appear to rotate the molecule at all.

Possible vibrational movements include; symmetric stretch, asymmetric stretch, bending

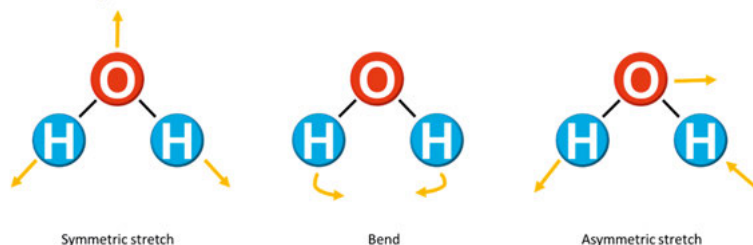


Figure 2.3. Three possible vibrational modes of water. Symmetric stretch, all of the vibrations are in-phase, both OH bonds extend and distend simultaneously; bend, the hydrogen atoms come close together and further apart, like a pair of scissors; asymmetric stretch, the vibrations are out-of-phase, one OH bond extends while the other distends and *vice-versa*.

In order for a vibration to be infrared active, the vibration must result in a change in dipole of the molecule. This means that although N₂ may have the same stretching vibrations as CO, N₂ is not visible on an IR spectrum. N₂ has no permanent electrical dipole across the molecule, whereas oxygen is much more electronegative than carbon. Consequently the oxygen atom of CO holds a partial negative charge while the carbon atom holds a partial positive charge. When the CO undergoes a stretching vibration the separation of these two charges changes, thus changing the dipole on the CO bond. As a result a vibrational band $\nu(\text{CO})$ will be seen in the FTIR spectrum (free CO 2143 cm⁻¹).

The carbon monoxide vibration is actually very useful for inorganic chemists because it appears in a relatively uncrowded region of the FTIR spectrum (1700 - 2000 cm⁻¹). The position of $\nu(\text{CO})$ varies depending on the coordinating transition metal, the oxidation state, or the mode of bonding of CO to the transition metal. There are three metal-CO bonding interactions. They are described by the Dewar Chatt model.

2.1.3 Dewar Chatt Model of synergistic bonding

The Dewar Chatt model describes the interactions between a metal centre and π -acceptor ligands such as CO and CN. Both of which are present in the [FeFe]-H₂ase cofactor and [FeFe]-H₂ase cofactor mimics. The interactions are as follows:¹¹²⁻¹¹⁴

1. CO-Metal sigma bonding
2. Metal-CO π -backbonding
3. CO to metal π -bonding

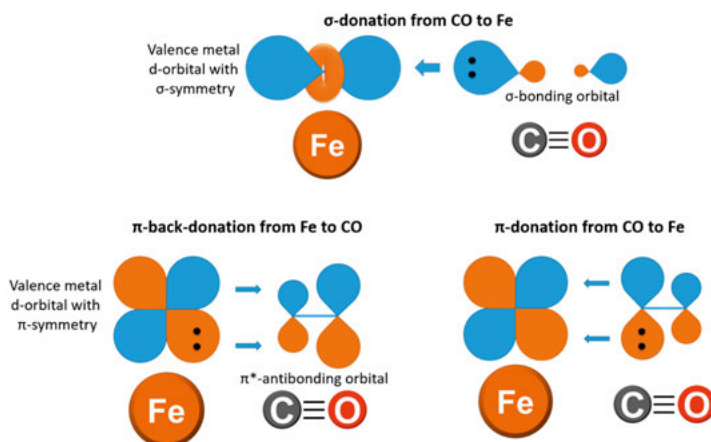


Figure 2.4. Schematic diagrams showing the bonding/antibonding interactions available for a ligand with a CO ligand that is bound to Fe.

There are two main factors governing the vibrational frequency of a π -acceptor ligand like CO. The first, is the oxidation state of the metal centre. The lowest unoccupied molecular orbital (LUMO) of CO (or another π -accepting ligand), is actually the antibonding π^* -orbital. The energy of the LUMO is sufficiently low that it may accept electrons from a metal centre. If the metal centre has plenty of electrons, then it may donate a lot of electron density to the π^* -orbital, weakening the CO bond overall, and thus decreasing the vibrational frequency.

The second big factor determining the vibrational frequency is the coordination geometry of the metal or the bonding mode of the π -acceptor ligand. In the case of [FeFe]-H₂ases, the CO ligand may be terminal, bridging or semi-bridging. Additionally, the CN ligands are also π -accepting so they may also be used to probe the properties of a [FeFe]-H₂ase cofactor mimic. FTIR is therefore a tool that will be extensively used in this thesis to characterise and probe various oxidation states and hydride states of molecular mimics.

The number of vibrational bands in the IR spectrum may be determined by the number of CO ligands and the symmetry of the metal complex. Carbonyl stretching frequencies have been determined by Cao and Hall for Fe₂(μ -pdt)(CO)₆.¹¹⁵ It has C_{2v} symmetry and many [FeFe]-H₂ase cofactor mimics show similar CO vibrational patterns in the FTIR but may differ due to the electronic or geometric properties of the specific complex or state. Changes in

bonding modes of the carbonyl will result in new CO patterns which may indicate structural changes to a complex, for example during artificial maturation the [FeFe]-H₂ase cofactor mimic adopts a rotated structure. All of these factors together make the wavenumber of CO ligands or CN ligands rather sensitive to the electron density or the geometry of the metal centre. Figure 2.5 shows the regions in the FTIR spectrum where one can expect to observe a CO or CN vibration.

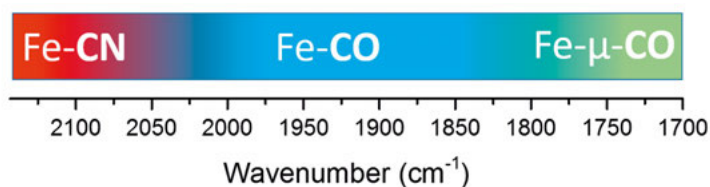


Figure 2.5. Scale showing the wavenumbers at which one may observe a vibrational band for iron (Fe) bound CN or CO. Spread caused by Fe-CO/CN π -backbonding interaction with Fe. CN bands are observed from 2050 cm⁻¹ to 2200 cm⁻¹, the terminal carbonyl bands are observed from 1800 cm⁻¹ to 2050 cm⁻¹, and the bridging CO vibrations are observed around 1700 cm⁻¹ to 1800 cm⁻¹.

2.2 EPR spectroscopy

2.2.1 EPR spectroscopy

EPR is a type of resonance spectroscopy used to study the electrons of molecules that contain unpaired electrons (paramagnetic species). EPR is a research tool useful for investigating radicals and paramagnetic metal clusters. It is an invaluable tool in the study of [FeFe]-H₂ases and their mimics. This section aims to briefly explain how EPR works.

2.2.2 Basic EPR theory

Electrons are moving charges which means that they generate a magnetic moment. For a single electron the magnetic moments are $m_s = \pm\frac{1}{2}$, and in the absence of an externally applied magnetic field they are degenerate in energy. However, when a magnetic field is applied, B_0 , the energy levels are split following the relationship in equation 2.4, illustrated in figure 2.6. The differences in the energy levels increases until it is in resonance with the applied magnetic field. A photon is absorbed and this leads to an absorption peak in the EPR spectrum. This is known as the Zeeman effect and it forms the basis of EPR spectroscopy.^{112, 116}

$$\Delta E = h\nu = g\mu_B B_0$$

Equation 2.4 Describes the Zeeman effect, i.e. how the difference in energy levels (ΔE) changes with an applied magnetic field (B_0)

Where;

ΔE is the energy difference between the two electron magnetic moments.

h is Planck's constant

ν is the frequency of (microwave) radiation

g is a conversion factor equal to 2.00232 for a free electron that is not associated with an orbital

μ_B is the Bohr magneton $= 9.274 \times 10^{-24} \text{ J T}^{-1}$

B_0 is the externally applied magnetic field

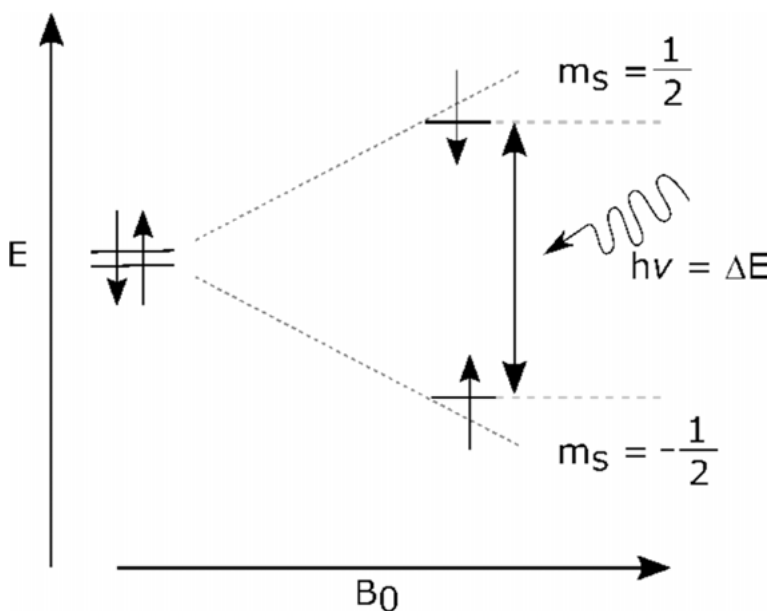


Figure 2.6. Schematic showing the change in energy between the electronic magnetic moments when an external magnetic field is applied. At $B_0 = 0$ the m_s levels are degenerate, as B_0 increases, the energy levels diverge.

2.2.3 EPR spectra

EPR spectra are traditionally illustrated as the first derivative of the absorption spectrum. The observed EPR spectra are determined by several other factors which will be described below.

Spin orbit coupling is a major contributor to the observed g -value. Spin-orbit coupling is a result of the interaction between the spin angular momentum (\underline{S}) of an electron and its orbital angular momentum (\underline{L}). For an electron in a molecular orbital the magnetic moment operator ($\underline{\mu}$) contains a contribution from both the spin angular momentum of the electron and the spin orbital moment of the electron. The effect of spin orbit coupling on the EPR spectrum varies depending on the size of the atom associated with the electron. For small atoms (C, H, N, O), the contribution from spin orbit coupling is small, meaning that the observed g -values are close to that of the free electron (2.00232). For larger atoms such as iron, the contribution from spin orbit coupling is high

so that the g-value can vary significantly from the g-value associated with a free electron. Meaning that the observed g-value holds some important structural information.

The line shape of the EPR spectrum also gives very important structural information. The directionality of molecular orbitals gives rise to g-factor anisotropy (directionality of the spectrum). Meaning that if you have a crystal sample, the EPR spectrum you obtain will vary depending on the orientation of the crystal in space. The spectra reported in this thesis are all measurements of powder samples (frozen solutions of sample). In such cases, the paramagnetic molecules are randomly arranged in all possible orientations, and the observed spectrum is a sum of all of these.

The major factor that affects the shape of the EPR spectrum is the selection rules that impose that only the magnetic moments perpendicular to the magnetic field are detected. The consequence of this on the EPR spectrum is that it is possible to observe 4 different line shapes, shown in figure 2.7.

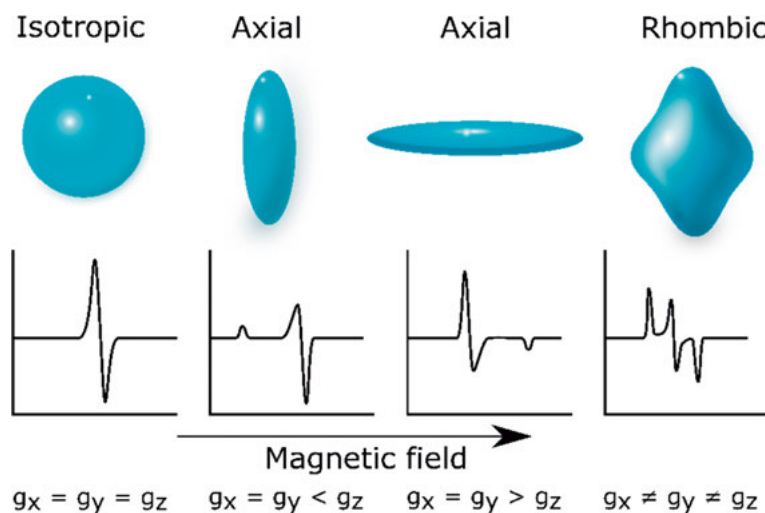


Figure 2.7. The various characteristic EPR spectral shapes. An isotropic signal is observed for highly symmetric molecules when $g_x = g_y = g_z$; axial signals occur when either $g_x = g_y < g_z$ or $g_x = g_y > g_z$; and rhombic signals occur when none of the g-values are equal $g_x \neq g_y \neq g_z$.

Nuclear hyperfine coupling comes into play when the atom coupling to the electron has a non-zero nuclear spin ($I \neq 0$). This is the case for e.g. manganese, which has nuclear spin $I = 5/2$. The result is $2I+1$ energy levels so the observed spectrum of a paramagnetic manganese species is expected to have a 6-line feature, as is observed for one of the reduced dimanganese complexes in paper IV.

2.3 X-ray absorption spectroscopy (XAS)

X-ray absorption spectroscopy (XAS) gives information on the oxidation states and coordination environments of specific elements in compounds. XAS was developed in 1971 by Sayers *et al.*¹¹⁷ XAS observes the results of exciting an electron from the ground state to the excited state or into the continuum (ionisation). XAS is particularly applicable to (redox) metalloenzymes and their inorganic cofactor mimics because of characteristic changes in the spectra caused by changes in oxidation state, and also because it is possible to probe a specific element without interference from the other elements in a complicated system by selecting an appropriate X-ray energy.¹¹⁸ Synchrotron sources are able to provide the X-ray energies required to probe most elements.

There are two major component of the XAS spectrum:¹¹⁹

- XANES – X-ray absorption near edge structure- measures the transition of electrons from core electronic states to excited electronic states (LUMO). These measurements report on the electronic structure and the geometry/symmetry of the metal centre.
- EXAFS – extended X-ray absorption fine structure – measures the transition of electrons from the core electronic states to the continuum (ionisation). These measurements report on the ligands neighbouring the metal centre and the distance between the metal and ligands.

Molecular mimics of inorganic cofactors play an essential role in interpreting XAS of biological samples. Model complexes with known structures provide a benchmark for analysing the influence of the coordination environment on the XAS spectrum. There are many examples in the literature of the study of XAS spectra of [FeFe]-H₂ase cofactor mimics. One notable example is the study by Kozitski *et al* in which 18 [FeFe]-H₂ase cofactor mimics were investigated by XAS to create a catalogue of XANES and EXAFS spectra of [FeFe]-H₂ase cofactor mimics with various substitutions.⁶⁷ Later studies have also specifically investigated the effect of asymmetry¹²⁰ or the presence of a bridging hydride¹²¹ on the XAS spectra. These studies together provide valuable insight into how changes in the coordination sphere of irons in [FeFe]-H₂ase cofactor mimics can be seen in XANES and EXAFS spectra, informing the analysis of XAS of biological samples in which the cofactor may not be so well defined.

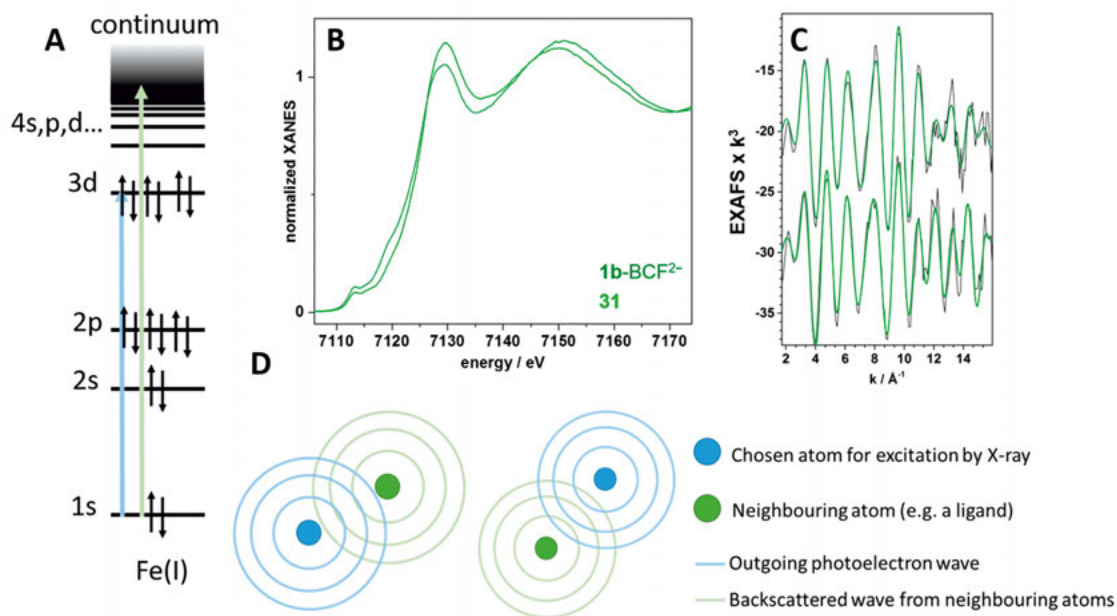


Figure 2.8. Schemes and diagrams visualizing selected key principles in XAS. **Panel A:** Energy level diagram showing the transitions observed by K-edge XAS, the blue arrow indicates the transitions observed by the XANES region, and the green arrow the transitions observed in the EXAFS region, the $3s$ and $3p$ orbitals are omitted for clarity. **Panel B:** Shows an example of a XANES spectrum which contains a pre-edge (~ 7110 – 7120 eV) and a difference in K-edge accompanied by oxidation. Reproduced from reference 57 (paper III) with permission from the Royal Society of Chemistry. **Panel C:** Shows an example of EXAFS spectra, exemplifying the characteristic oscillatory nature of the EXAFS region. Reproduced from reference 57 (paper III) with permission from the Royal Society of Chemistry. **Panel D:** A diagram showing the interaction between the outgoing photoelectron wave, and backscattered radiation from neighbouring atoms.

Sharp increases in absorption at specific X-ray photon energies are characteristic of specific elements. These sharp increases are known as the absorption edge and depending on which core shell the electron comes from, the edge is called either the K-edge or the L-edge. The K-edge results from the excitation of an electron from a $1s$ core level, while the L-edge originates from the excitation of an electron from a $2s$ or $2p$ core level. L-edge spectra are very sensitive, but because of the experimental difficulty accompanied by L-edge studies, most investigations focus on the K-edge.

XANES spectra give information about the K-edge because the K-edge absorption energy increases with a decrease in electron density on the metal centre. An illustrative example of this is shown in figure 2.8, panel B in which shows the XANES spectra of complex **1b**-BCF $^{2-}$ and the product of oxidation, **31** (see Chapter 5, paper III, for details). The most prominent contributor to

the K-edge absorption is usually the transition from $1s$ to np . np is the lowest unoccupied p orbital of the chosen metal centre. However other transitions are possible, especially for transition metals with partially occupied d -orbitals. The formally forbidden transitions from $1s$ to $(n-1)d$ result in a weak absorption before the larger absorption in the K-edge. These absorptions are consequently known as pre-edge features. Pre-edge features increase in intensity if the metal centre is perturbed from an octahedral geometry.

Sometimes the energy of the X-ray photon is enough to cause ionisation of the metal centre releasing a photoelectron. In the context of EXAFS the photoelectron is modelled as a wave phenomenon, and the oscillatory nature of the EXAFS spectrum is a consequence of this (figure 2.8, panel C). The outgoing wave (the photoelectron) interacts with backscattered waves resulting from the neighbouring atoms (the ligands/coordination environment). Depending on the energy of the incoming X-ray photon, some of these interactions are constructive, and some are destructive, which results in alternating variations in the absorption coefficient (figure 2.8, panel D). Fourier transform of the EXAFS spectra can provide information about the distances between the X-ray absorbing metal centre and the neighbouring atoms, within a range of 4-5 Å. Complex equations are used to fit the EXAFS region and gain valuable insight into the structure of non-crystalline samples, the analyses were summarised by Junko Yano and Vittal K. Yachandra, and also by Lytle *et al.*^{118, 122}

2.4 Electrochemistry

Electrochemistry is a vital tool for observing electron transfer processes (reduction/oxidation). Cyclic voltammetry (CV) in particular is used frequently in this thesis to probe for proton reduction by my molecular catalysts. CV is a central technique for understanding molecular catalysis and is widely used to observe small molecule activation. In this thesis I use molecular cyclic voltammetry in which the analyte (the molecule being measured) is in solution, rather than attached to an electrode as in protein film electrochemistry (PFE) for example.

2.4.1 Cyclic voltammetry

In cyclic voltammetry the applied potential (V) is varied in steps and the resulting current (i, measured in amperes, A) is measured. When the applied potential reaches a voltage that is the correct energy to transfer electrons into the analyte's lowest unoccupied molecular orbital (LUMO) an increase in current is observed. In the case of a reversible reduction, a similar increase in current is observed on the return scan. A good indication that a redox event is truly reversible is to check the potential difference between the peak reducing (cathodic) current potential ($E_{p,c}$) and the peak oxidizing (anodic) current potential ($E_{p,a}$) (figure 2.9). The difference for a truly reversible electron transfer

will result in a peak-to-peak separation of 57 mV at 25 °C for analytes in solution. However, in practice this is not always true, as in paper III. One can confirm the peak separation for a reversible electron transfer by measuring the CV of a well known internal standard, most commonly ferrocene.¹²³

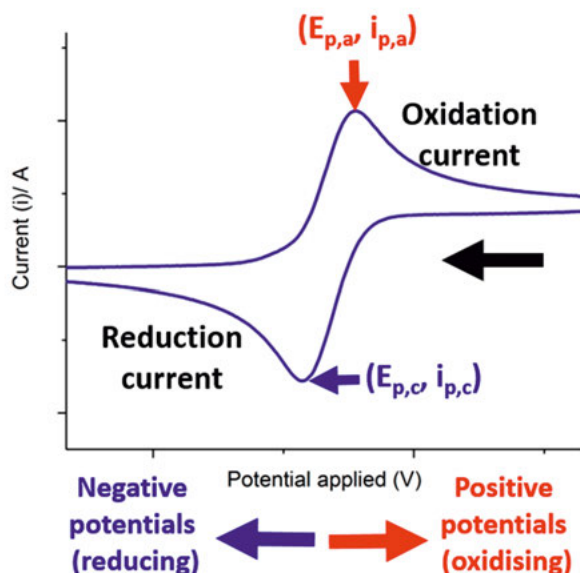


Figure 2.9. Schematic depiction of a CV trace for a reversible redox process. I use the IUPAC convention for plotting CVs in this thesis. That is, scan start starts at oxidising potentials and scans to more negative potentials before turning around at a specified cut-off point, beginning the return scan. The x-axis starts at the negative (more reducing potentials) on the left and increases to the more positive (oxidising) potentials on the right, the oxidising currents are recorded as peaks ($E_{p,a}$, $i_{p,a}$), and the reducing currents are recorded as troughs ($E_{p,c}$, $i_{p,c}$).

Cyclic voltammetry can be rationalised by the Nernst equation (equation 2.5), which relates the applied potential (E) to the formal potential ($E^{0'}$) of the analyte and the equilibrium concentrations of the oxidised analyte ($[ox]$) or reduced analyte ($[red]$). The formal potential is the measured reduction potential of the analyte.

$$E = E^{0'} + \frac{RT}{F} \ln \left(\frac{[ox]}{[red]} \right)$$

Equation 2.5 The Nernst equation. E is the applied potential in the electrochemical cell, $E^{0'}$ is the formal potential of the analyte, R is the gas constant, T is the temperature in Kelvin, F is faraday's constant, $[ox]$ is the concentration of oxidised analyte and $[red]$ is the concentration of reduced analyte.

The Nernst equation predicts how the concentration of the species close to the electrode (in the diffusion layer) changes as the applied potential is scanned. The concentrations are local to the working electrode and the CV is actually measuring both the reduction of analyte and the depletion of oxidised or reduced analyte from the diffusion layer. These phenomena have been nicely summarised in the Practical beginner's guide to cyclic voltammetry.¹²³

2.4.2 What information can we get from CV experiments?

In addition to the formal reduction potential, cyclic voltammetry experiments can also provide information on other properties of the analyte. One experiment that should be carried out before investigating catalytic activity is a scan rate experiment, in which you can vary the scan rate and observe an increase in $i_{p,a}$ or $i_{p,c}$ with an increase in scan rate. Specifically, for a diffusion controlled process, the peak current is linearly proportional to the square root of the scan rate, and this relationship is described by the Randels-Sevcik equation, equation 2.6.

$$i_p = 0.446nFAC \left(\frac{nFvD_0}{RT} \right)^{1/2}$$

Equation 2.6. The Randels-Sevcik equation for a diffusion controlled electron transfer process, which shows that the peak current is linearly proportional to the square-root of the scan rate. n is the number of electrons, F is Faraday's constant, A (cm^2) is the surface area of the electrode, C is the concentration of oxidised analyte (mol cm^{-3}), v is the scan rate, D_0 is the diffusion coefficient ($\text{cm}^2 \text{s}^{-1}$), R is the gas constant and T is the temperature in Kelvin.

Fitting the peak anodic/cathodic current to this equation can indicate whether the analyte is moving freely in solution or if it is adsorbed as a film on the electrode surface. It is important to establish this before you start studying the catalytic activity of a supposedly homogeneous catalyst in detail, otherwise you may just be measuring the catalytic activity of a film on the electrode surface. Further information that can be gained from the Randels-Sevcik plot is the diffusion coefficient of the analyte. This is useful for accurate modelling of electron transfer processes in software such as digielch. The diffusion coefficient is hidden in the slope of the Randels-Sevcik plot (where x is $v^{1/2}$).¹²⁴ Another useful number to be gained from scan rate experiments is the heterogeneous rate constant. This can be calculated by comparing the peak anodic and peak cathodic potentials with $E_{1/2}$ in a trumpet plot. As the scan rate is increased, so does the peak-to-peak separation. Plotting the difference between E_p and $E_{1/2}$ against the log of the scan rate creates a trumpet shape, hence the name. The experimental trumpet plot is then overlaid with a working curve (simulated in digielch as $D_{0,\text{sim}} = 1 \times 10^{-5} \text{ cm}^2 \text{s}^{-1}$, and $k_{s,\text{sim}} = 1 \text{ cm s}^{-1}$), see figure 2.10, reproduced from paper III.

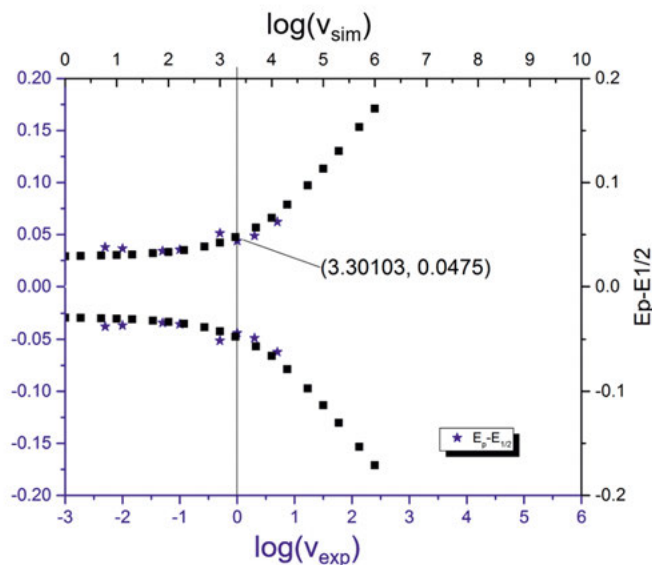


Figure 2.10. Trumpet plot used to calculate the heterogeneous rate constant (rate of electron transfer from the working electrode to the analyte). Reproduced from reference 57 (paper III) with permission from the royal society of chemistry.⁵⁷

Equation 2.7 can then be utilised to find $k_{s,exp}$ (assuming the diffusion coefficient is determined from the Randels-Sevcik analysis).⁹⁹

$$\log \left(\frac{k_{s,sim} \sqrt{D_{0,exp}}}{\sqrt{D_{0,sim}} k_{s,exp}} \right) = \frac{1}{2} (\log(v_{sim}) - \log(v_{exp}))$$

Equation 2.7. Equation used to calculate the heterogeneous rate constant for electron transfer from the electrode to the analyte. A very good explanation for this equation can be found at reference ⁹⁹.

2.4.3 Catalysis

Catalytic mechanisms are usually written using EC notation. E denotes an electronic step, which is drawn as a downward arrow and can be reversible (subscript r) or irreversible (subscript i); C denotes a chemical step, which is drawn as a sideways arrow, and can also be reversible or irreversible. This means that for a one electron one chemical reaction (EC), there are four possibilities; $E_r C_r$, $E_i C_r$, $E_r C_i$, or $E_i C_i$. This is already quite complicated and it gets even more complex when we consider the fact that proton reduction involves 2 electrons and 2 protons. The EC mechanism has been modelled extensively, and researchers are just beginning to get to grips with the EECC, ECEC, ECCE and CEEC models. Never the less, some mechanistic information can be gained from observing CV traces.¹²⁵

The first thing to do when studying catalysis is to find out if your analyte is actually a catalyst. In the case of proton reduction, a good first indication is through observing the change in CVs when an acid is titrated into the electrochemical cell. The current should increase with the addition of acid due to the higher concentration of protons (figure 2.11, panel A). If the electronic and chemical step are coupled, as in (figure 2.11, panel B), then the onset potential will become more positive with the addition of protons. The higher concentration of protons pushes the equilibrium of the chemical step towards RedH, which in turn pulls the equilibrium of the electronic step towards Red. If the reaction started with a chemical step, that would likely be observable by spectroscopy (paper III).

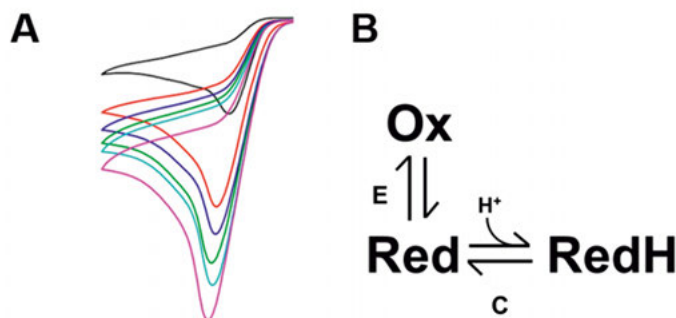


Figure 2.11. Panel A: an example of a catalytic wave. The peak current increases with substrate (in this case protons) concentration. **Panel B:** reaction scheme showing a coupled EC mechanism.

Zone diagrams, introduced by Saveant can help with interpreting catalysis.¹²⁶ By changing experimental parameters, one can traverse the zone diagram and change the shape of the CV. The ideal case is the S shaped curve, this zone is known as *pure kinetic conditions no consumption of substrate*. In this regime, the bulk concentration of substrate (C_s) far exceeds the bulk concentration of analyte (C_a) and the curve is independent of scan rate. If you are lucky enough to observe this regime, the overall rate constant for catalysis (k) can be calculated from the experimentally measured plateau current intensity (I_p) using equation 2.8.

$$I_p = FC_a\sqrt{D_0}\sqrt{kC_s}$$

Equation 2.8. This equation can be used to calculate the rate constant of catalysis for an EC mechanism, k , from the plateau current intensity, I_p . F is faraday's constant and D_0 is the diffusion coefficient.

However, in cyclic voltammetry, especially methods using a stationary working electrode, it is very rare to observe this S-shaped curve. We usually observe the regime called *pure kinetic conditions substrate diffusion*. In this regime, the plateau current density cannot be used to calculate the rate constant because there is no plateau, and because the regime is now dependent on an array of other factors.¹²⁷ These zone diagrams have only really been studied for EC mechanisms (figure 2.11), only recently have people extended these ideas into modelling more complicated reaction schemes.¹²⁸

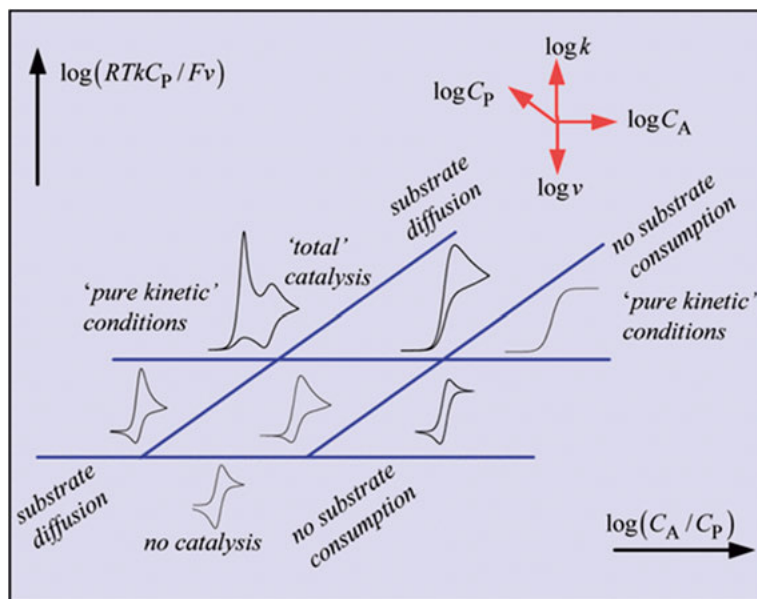


Figure 2.12. Cyclic voltammetry zone diagram. Kinetic regimes observable from studying catalysis by CV. Reproduced with permission from reference ¹²⁶. By varying experimental parameters one may observe different kinetic regimes (zones) for the EC mechanism.

Other options to gain quantitative information about a catalytic mechanism from CV traces, include analyses such as FOWA, or modelling using digielch. In my opinion, the most reliable way to get kinetic and mechanistic information about your catalyst is to compliment CVs with spectroscopic characterisation of trapped intermediates, other electrochemical techniques such as chronoamperometry, or time resolved spectroscopy such as stopped flow.

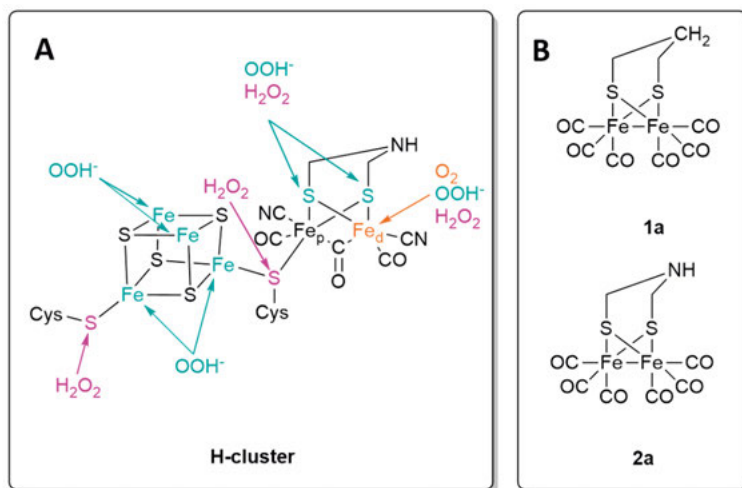
Chapter 3: Paper I Oxygen tolerance

Introduction

As discussed in chapter 1, H₂-evolving catalysts will play a central role in the transition to a hydrogen economy. [FeFe]-H₂ases and their cofactor mimics are a promising route towards the goal of a hydrogen economy, and the focus of this thesis. However, hydrogenases are notoriously oxygen sensitive.¹²⁹⁻¹³¹ On the H-cluster, there are multiple possible sites of attack by oxygen or reactive oxygen species (ROS, also known as partially reduced oxygen species, PROS) as shown in Scheme 3.1 panel A. Attack is most likely to occur at a sulphur or an iron ion. When one of these sites is attacked by oxygen/ROS, a cascade of reactions is initiated that ultimately leads to decomposition of the H-cluster.¹³⁰

Many molecular [FeFe]-H₂ase cofactor mimics, even without the [Fe₄S₄]-cluster, and other homogeneous proton reduction catalysts reported so far are inactivated by oxygen, making them incompatible with operation under air, and therefore not viable for scale-up at an industrial level.¹⁰⁶ A notable exception is the cobalt-ATCUN tripeptide catalyst of Bren and co-workers, which operates at 88 % faradaic efficiency and TON 447 in 250 minutes, and functions for several hours on the bench, i.e. under aerobic conditions.¹³² Additionally, Dey and co-workers have reported several [FeFe]-H₂ase cofactor mimics that are O₂ tolerant catalysts after surface immobilisation.^{58, 133} Computational studies have demonstrated that binding of oxygen to the [FeFe]-H₂ase cofactor is thermodynamically favourable.^{134, 135} Furthermore, Esselborn has demonstrated that CpI crystals (from *Chlostridium pasteurianum*) undergo structural changes at the H-cluster upon exposure to oxygen accompanied by a decrease in the enzymes activity. These structural changes were observed by X-ray crystallography and showed that there are multiple paths to decomposition by oxygen, and that attack of the distal iron of the [FeFe]-H₂ase cofactor is required to initiate both pathways.¹³⁶ These previous investigations suggest that investigations of oxygen attack on just the [FeFe]-H₂ase cofactor mimic in the absence of a [Fe₄S₄]-cluster can provide useful information regarding oxygen tolerance.

Understanding the processes by which oxygen inactivates these synthetic systems is key to designing and developing new H₂-evolving catalysts, both molecular and enzymatic, with improved oxygen tolerance and scalability. In this chapter, I will discuss the results of our investigation of the oxygen tolerance of two structural mimics of the [FeFe]-H₂ase diiron cofactor. Specifically, we investigated the effect of changes in the bridgehead in the bridging dithiolato ligand, from an alkyl bridgehead (-CH₂-, **1a**), to an amine bridgehead, (-NH-, **2a**) (redrawn in scheme 3.1, panel B, for reference). The reason for this is that the nitrogen bridgehead is believed to play a role not only in the proton relay of the native enzyme, but also in the protection of [FeFe]-H₂ase cofactor mimics from O₂/ROS attack.



Scheme 3.1. Oxygen attack on the H-cluster and [FeFe]-H₂ase mimics. **Panel A:** Showing the possible sites of oxygen attack on the H-cluster, along with the probable attacking species as proposed by Stiebitz *et al* 2012, oxygen (orange), hydrogen peroxide (magenta) and hydroperoxyl (the protonated form of superoxide) (cyan).¹³⁰ **Panel B:** Complexes **1a** with a carbon bridgehead, and **2a** with a nitrogen bridgehead.

The reactivity of similar model complexes with molecular oxygen under electrocatalytic conditions has already been reported by Dey *et al.* In 2014 they showed, through study of the oxygen reduction reaction (ORR) by [FeFe]-H₂ase cofactor mimics, that the presence of a nitrogen bridgehead in the bridging dithiolato ligand plays a major role in reducing the amount of H₂O₂ produced under ORR catalytic conditions. They also demonstrated that this lower H₂O₂ production led to a longer lifetime of the catalysts for hydrogen evolution under acidic, aerobic conditions in aqueous solvent. Despite the detailed studies described above, it is challenging to know specifically which ROS attacks the [FeFe]-H₂ase cofactor mimics under electrocatalytic conditions for proton reduction, because many ROS may be generated at the electrode before the potential for proton reduction is reached (eqs 3.1 - 3.4).^{137, 138}

Potentials reported against SHE at pH 7



These reductions make it impossible to precisely control the species that actually attack the [FeFe]-H₂ase cofactor mimics at the potentials required for proton reduction. It is also rather challenging to spectroscopically observe the products of oxygen attack under electrocatalytic conditions. For example, in Dey's report, they were able to observe the FTIR of the electrode only before and after the ORR experiment. Interestingly, at the end of their ORR experiments, they observed a decrease in carbonyl peak intensities, relative to the starting spectra, which is expected due to degradation of the catalyst, accompanied by the appearance of peak intensities at 800-1200 cm⁻¹, corresponding to the S-O stretches of RSO₂⁻ and RSO₃⁻ groups.¹³⁹ Potential sulfoxxygenation of the complexes **1a** and **2a** will be discussed later in the chapter.

The aims of the project summarised in this chapter are:

- To investigate the reactivity of **1a** and **2a** towards molecular oxygen and ROS.
- Observe the reactivity of **1a** and **2a** with oxygen under reducing and acidic conditions.
- Compare how the different bridgeheads in the bridging -pdt- or -adt- ligands affect these reactivities.

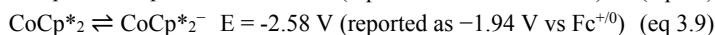
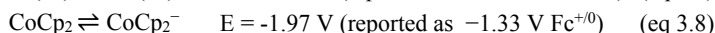
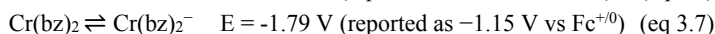
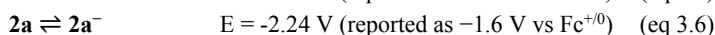
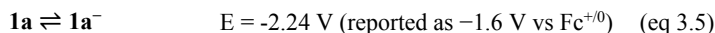
In this investigation we therefore used chemical reductants to reduce compounds **1a** and **2a** in the presence and absence of oxygen. The products of these treatments were then characterised by FTIR, NMR and EPR spectroscopy as well as mass spectrometry. Additionally time-resolved IR was carried out to observe transient species during oxygen attack. Importantly, we found that **O-1a⁻** and **O-2a⁻** form at potentials less negative than the starting complexes **1a** and **2a**. This means that the observed transformations likely do not occur via **1a⁻** or **2a⁻**. I will start by discussing the reactivity of **1a**, followed by **2a** and then I will make a comparison of the two complexes.

2.2 Reactivity of **1a**

A cyclic voltammogram of **1a** was recorded to determine its reduction potential -2.24 V vs SHE (reported as -1.6 V vs Fc^{+/0}). Based on this, three reducing agents were tested for reactivity with **1a**. The chosen reducing agents were

bis(benzene)chromium ($\text{Cr}(\text{bz})_2$), cobaltocene (CoCp_2) and decamethylocobaltocene (CoCp^*_2), and their reduction potentials are shown in equations 3.5 to 3.9.

Potentials reported against SHE (reported against $\text{Fc}^{+/0}$)



As expected **1a** does not react significantly with $\text{Cr}(\text{bz})_2$, CoCp_2 or O_2 in isolation. However, even in the absence of oxygen, significant reactivity was observed when CoCp^*_2 was mixed with **1a**. A complicated FTIR spectrum was obtained with peaks at 1975 cm^{-1} , 1945 cm^{-1} and 1925 cm^{-1} , and multiple broad and smaller peaks between 1970 cm^{-1} – 1850 cm^{-1} that did not correspond to the FTIR spectrum previously reported for **1a**[−], figure 3.1 panel A. Instead, we attributed this more complicated FTIR spectrum to the dimerization of **1a**[−], as previously reported by Borg and coworkers.¹⁴⁰ Regarding the dimerization hypothesis, we did not observe the $\mu\text{-CO}$ band in the FTIR that should be present if it is indeed the species proposed by Borg and co-workers. When the mixture of **1a** and CoCp^*_2 was exposed to oxygen, another new spectrum was observed, figure 3.1 panel A. More surprisingly, reactivity was observed also with the milder reductant CoCp_2 , and we focused our efforts on the oxygenation chemistry under these milder reducing conditions. The reactivity of **1a** is summarised in scheme 3.2

A mixture of **1a** and CoCp_2 was exposed to oxygen. Limited reactivity was observed showing only small new, broad, ill-defined carbonyl bands at 2020 cm^{-1} , 1960 cm^{-1} and 1891 cm^{-1} after the addition of 10 eq CoCp_2 , figure 3.1 panel B. These many broad peaks at lower wavenumbers than **1a** indicated that at least two reduced species were present after exposure to the CoCp_2 , one of the species we assigned to the reduced oxygenated species **O-1a**[−], and it is possible that dimerization also occurred.¹⁴⁰ These new carbonyl bands in the IR spectrum were fully diminished after 20 minutes in the glovebox, indicating that the reduced oxygenated product **O-1a**[−] or its dimer is not stable at room temperature.

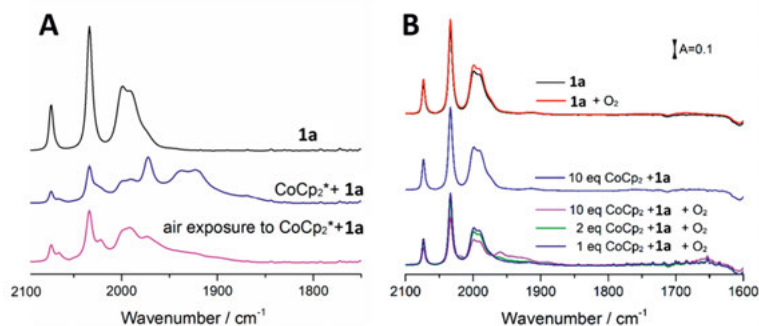


Figure 3.1. Reduction of **1a** **Panel A:** **1a** (black spectrum); reduction of **1a** using **CoCp₂*₂** (blue spectrum); reduction of **1a** using **CoCp₂*₂** in the presence of oxygen. **Panel B:** Top: **1a** (black spectrum) and reaction of **1a** with oxygen (red spectrum), shows low reactivity. Middle: reactivity of **1a** with 10 equivalents of **CoCp₂** (relative to **1a**) shows limited reactivity. Bottom: Reaction of mixtures of **1a** and **CoCp₂** with oxygen, some reactivity is observed at higher equivalents of **CoCp₂**. Reproduced from reference 71 with permission from the Royal Society of Chemistry.

Determining the intermediates during the deactivation of **1a** by oxygen under reducing conditions is a central aim of this investigation. Subsequently we explored the reactivity of **1a** with the oxygen transfer reagent mCPBA (*meta*-chloroperoxybenzoic acid) and also with ROS species superoxide ($\text{O}_2^{\cdot-}$) and hydrogen peroxide (H_2O_2). mCPBA was employed to explore the possibility of **O-1a** as a transient species during deactivation of **1a** by oxygen under reducing conditions. **O-1a** was previously synthesised using mCPBA and crystallised by Liu *et al.*,¹⁴¹ and sulphur oxygenates have been reviewed by Darensbourg and Wiegand,¹³⁹ based on these publications we expected mCPBA to react with **1a** to form **O-1a**, and that this would result in a new vibrational band at $\sim 1000\text{ cm}^{-1}$ corresponding to those already reported for S=O. mCPBA reacted with **1a** over 30 minutes to give a new FTIR spectrum with carbonyl bands at 2080 cm^{-1} , 2045 cm^{-1} and 2025 cm^{-1} , figure 3.2 panel A (**O-1a** in acetone 2083 cm^{-1} , 2045 cm^{-1} , 2017 cm^{-1} , 2000 cm^{-1}).¹⁴¹ These new peaks were stable over the course of 1 hour and when **CoCp₂** was added, no new carbonyl bands were observed. This lack of reactivity of **O-1a** with **CoCp₂** is likely due to the negative reduction potential of **O-1a** relative to **CoCp₂** -2.22 V vs SHE (reported as -1.58 V vs $\text{Fc}^{+/0}$ as determined in 2009)¹⁴¹ and it indicated that **O-1a** is unlikely to be an intermediate during the formation of a reduced oxygenated species **O-1a⁻**.

To test the possibility that ROS play a role in the formation of reduced oxygenated species. Potassium superoxide was added to **1a** which resulted in the formation of a broad signal between 1980 cm^{-1} and 1900 cm^{-1} , this signal remained stable for at least 20 hours, after which the experiment was terminated, figure 3.2 panel B. This apparent lack of spontaneous reversibility in-

indicates that whatever is formed when O_2^- is reacted with **1a** is not an intermediate in the formation of **O-1a⁻**. Additionally, H_2O_2 was added to **1a**. No new peaks were observed when H_2O_2 was added, indicating that **1a** does not react with hydrogen peroxide, figure 3.2 panel C. When a mixture of CoCp_2 and **1a** was reacted with H_2O_2 , the carbonyl bands completely disappeared, indicating full decomposition of the complex, figure 3.2 panel C, summarised in scheme 3.3 (this is in agreement with studies by Dey in 2014)¹³³. This dramatic reactivity indicates that H_2O_2 is not involved in the formation of a **O-1a⁻**, nor is it a ROS that can cause decomposition of **1a** alone. Together these results indicate that ROS species alone are probably not responsible for the formation of **O-1a⁻** under catalytic turnover conditions.

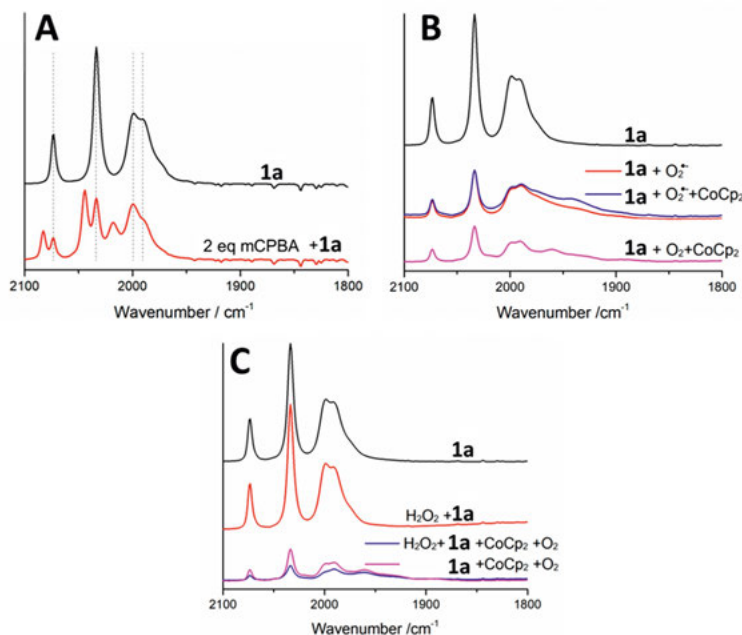
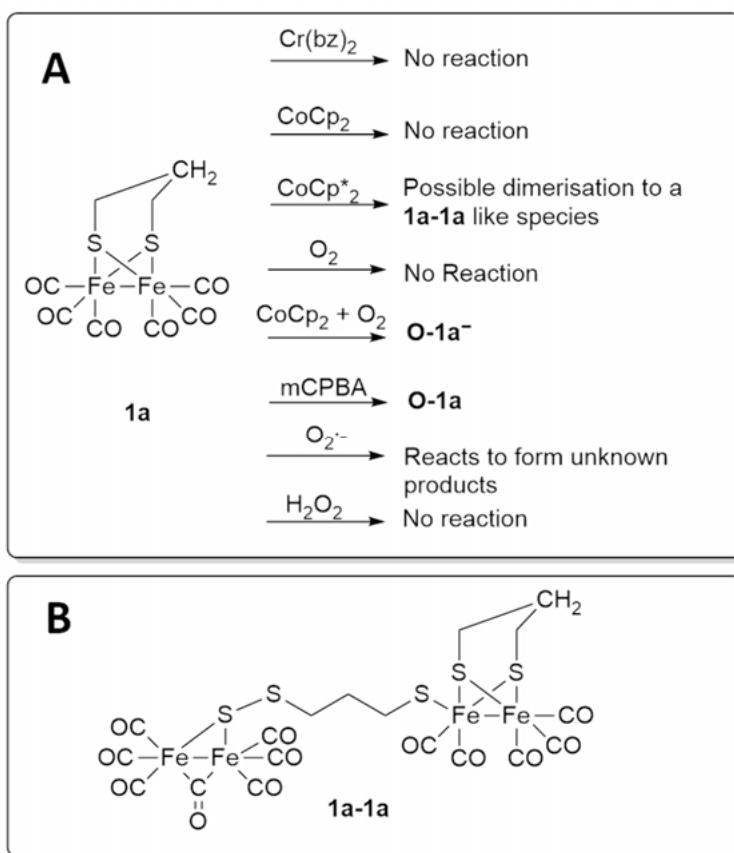


Figure 3.2. Oxygen transfer and attack by ROS. **Panel A:** FTIR spectrum of **1a** (black spectrum), FTIR spectrum showing the reactivity of **1a** with oxygen transfer reagent mCPBA (red spectrum). **Panel B:** FTIR spectrum of **1a** (black spectrum), FTIR spectrum showing the reactivity of **1a** with super oxide (red spectrum); FTIR spectrum of **1a** in the presence of superoxide and CoCp_2 (blue spectrum); FTIR spectrum of **1a** in the presence of oxygen and CoCp_2 (magenta spectrum). **Panel C:** FTIR spectrum of **1a** (black spectrum); FTIR spectrum of **1a** in the presence of hydrogen peroxide (red spectrum); FTIR spectrum of **1a** in the presence of hydrogen peroxide, CoCp_2 and oxygen (blue spectrum); FTIR spectrum of **1a** in the presence of CoCp_2 and O_2 . Reproduced from reference 71 with permission from the Royal Society of Chemistry.



Scheme 3.2. Schematic showing the reactivity of **1a** with reductants, mCPBA and ROS. **Panel A:** Summary of the reactivity of **1a** with three reducing agents, ROS species and the oxygen transfer agent mCPBA in dichloromethane. The reaction of **1a** with Cr(bz)_2 is shown in Paper I; The reaction of **1a** with CoCp_2 , CoCp^*_2 and CoCp_2 and O_2 are shown in figure 3.1; the reaction of **1a** with mCPBA, superoxide and hydrogen peroxide is shown in figure 3.2. **Panel B:** Possible products of dimerization. **1a-1a** was observed by FTIR spectroelectrochemistry under reducing conditions by Borg *et al.*¹⁴⁰

Subsequently, the reactivity of **O-1a⁻** with protons was explored and summarised in figure 3.3 and scheme 3.3. Chloroacetic acid and trichloroacetic acid were selected for this study. We found that deoxygenation (reactivation) of the complex was accelerated in the presence of protons. We thus conclude that the presence of protons facilitated deoxygenation and prevents further degradation at room temperature.

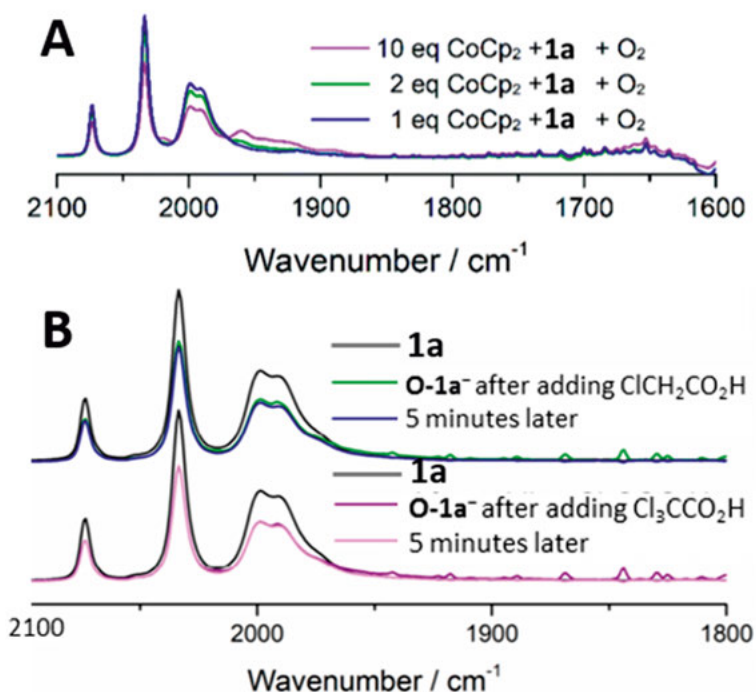
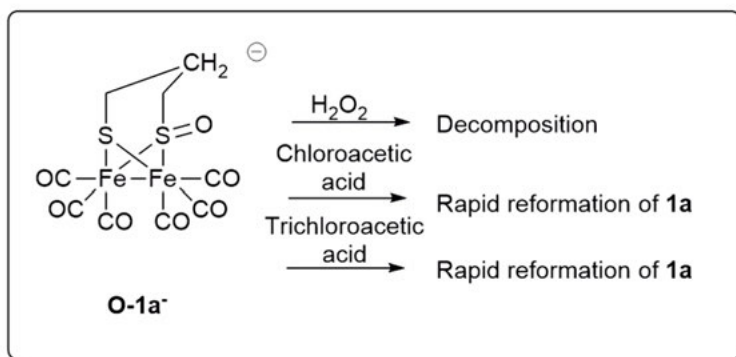


Figure 3.3. Addition of protons **Panel A:** Reproduced from figure 3.1 for clarity. Reactivity of **1a** with CoCp_2 in the presence of oxygen to form **O-1a⁻**. **Panel B:** Reactivity of **O-1a⁻** with chloroacetic acid ($\text{ClCH}_2\text{CO}_2\text{H}$) and trichloroacetic acid ($\text{Cl}_3\text{CCO}_2\text{H}$), both demonstrate that **1a** is reformed upon addition of protons. Black spectra, **1a** reference spectra to show that **1a** is indeed a product of the reaction between **O-1a⁻** and chloroacetic acid or trichloroacetic acid. Reproduced from reference 71 with permission from the Royal Society of Chemistry



Scheme 3.3. Summary of the reaction of **O-1a⁻** with hydrogen peroxide, chloroacetic acid and trichloroacetic acid. Observed by FTIR in figure 3.3.

2.3 Reactivity of **2a**

Complex **2a** also has a reduction potential at ~ -2.24 V vs SHE (reported as -1.6 V vs $\text{Fc}^{+/0}$). Because of this, **2a** is expected to react with the chemical reductants in a similar way to **1a**. And this is indeed what we observed. **2a** reacts neither with $\text{Cr}(\text{bz})_2$, CoCp_2 nor O_2 alone (scheme 3.4). The bands at 2074 cm^{-1} , 2033 cm^{-1} , 2000 cm^{-1} and 1989 cm^{-1} remain the same. The pronounced reactivity of **2a** with CoCp^*_2 indicated dimerization of the one-electron reduced species $\mathbf{2a}^-$, figure 3.4.¹⁴²

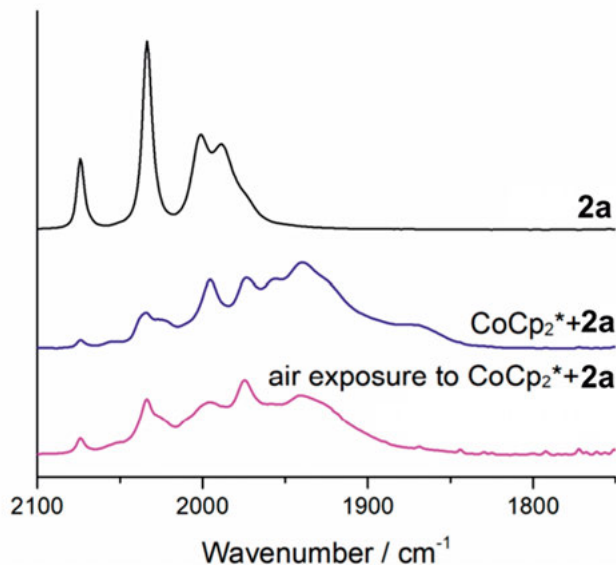


Figure 3.4. Reactivity of **2a** with CoCp^*_2 . Top: **2a** black spectrum. Middle: **2a** + CoCp^*_2 (blue spectrum). Bottom: **2a** + CoCp^*_2 in the presence of oxygen. Reproduced from reference 71 with permission from the Royal Society of Chemistry

When a mixture of **2a** and CoCp_2 was exposed to air, the peaks of **2a** almost disappeared to be replaced by new spectral features at 2038 cm^{-1} , 1997 cm^{-1} , 1957 cm^{-1} and 1946 cm^{-1} , figure 3.5. This is different from the spectrum of $\mathbf{2a}^-$ previously reported by Hammarstöm *et al.*¹⁴³ Nevertheless, the shift of approximately $35\text{--}40\text{ cm}^{-1}$ as compared with **2a** is in agreement with the formation of a reduced species. We thus assigned this product as the reduced oxygenated species $\mathbf{O-2a}^-$, with the O atom on one of the bridging sulphur ligands as proposed by Darensbourg, scheme 3.5.¹⁴¹

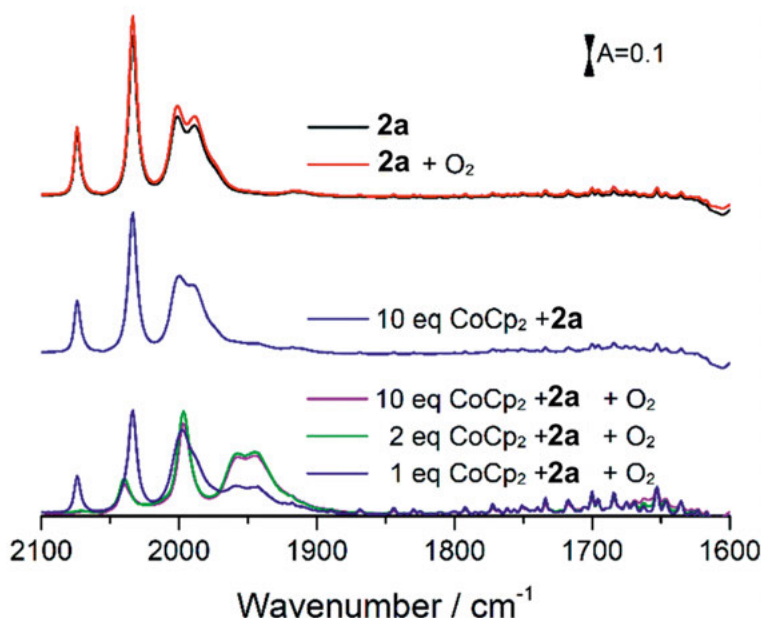


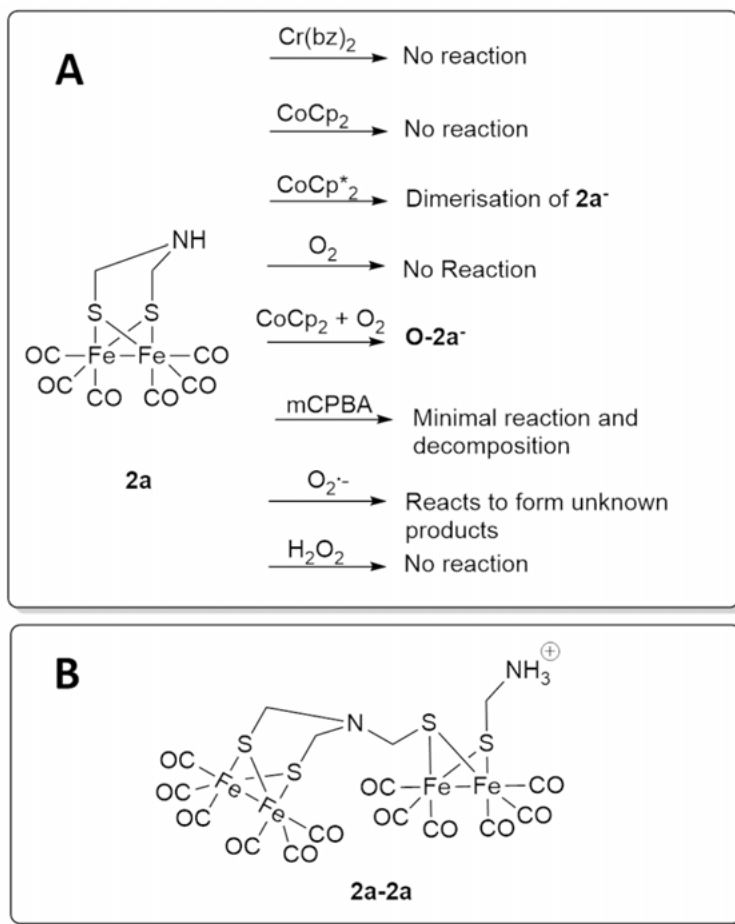
Figure 3.5. Reactivity of **2a** with CoCp₂ in the presence and absence of oxygen. Top: **2a** (black spectrum) and **2a** in the presence of oxygen (red spectrum). Middle: **2a** + CoCp₂ (blue spectrum). Bottom: **2a** + 1 eq CoCp₂ in the presence of oxygen (blue spectrum), **2a** + 2 eq CoCp₂ in the presence of oxygen (green spectrum), **2a** + 10 eq CoCp₂ in the presence of oxygen (magenta spectrum). Reproduced from reference 71 with permission from the Royal Society of Chemistry

Over the course of 20 minutes, the bands that we attributed to **O-2a⁻** degraded and approximately 30 % of the IR signal of **2a** was recovered. This behaviour contrasts with that of **1a**, which produced a less well defined and broader FTIR spectrum when it reacted with CoCp₂ in the presence of oxygen. This suggests that the more biologically relevant -adt- bridging ligand present in **2a** must play some role in the protection of the complex from degradation by oxygen under reducing conditions.

EPR was employed to probe the electronic structure of **O-2a⁻**. **2a** is EPR silent indicating a diamagnetic species, but the mixture of **2a**, CoCp₂ and O₂ shows an axial signal with g-values $g = 2.14$ and $g = 2.02$. The appearance of an EPR signal indicates the production of a paramagnetic species which we assigned to the one-electron reduced species, **O-2a⁻**. Through a combination of FTIR, UV-vis, EPR, mass spectrometry and DFT, we were able to propose the structure of **O-2a⁻** shown in scheme 3.5.

When **2a** was reacted with mCPBA, no new peaks were observed in the FTIR spectrum. Instead, the FTIR diminished with addition of mCPBA and

only at higher equivalents of mCPBA (10 eq relative to **2a**) were two new carbonyl bands observed in the FTIR at 2082 cm^{-1} and 2040 cm^{-1} (figure 3.6 panel A). These new peaks remained for 1 hour before decomposing. This reactivity indicated that **O-2a** is not an intermediate in the oxygenation of **2a** to form **O-2a⁻**.



Scheme 3.4. Schematic showing the reactivity of **1a** with reductants, mCPBA and ROS. **Panel A:** Summary of the reactivity of **2a** with three reducing agents, ROS species and the oxygen transfer agent m-CPBA in dichloromethane. **Panel B:** While **2a-2a** is a proposed dimer in the condensation of **2a** to $[\text{Fe}_6[(\text{SCH}_2)_3\text{N}]_2(\text{CO})_{17}]$ under acidic ($\text{HOTf } \text{pK}_a = -11.4$ in DCE).¹⁴⁴ It should be noted that **2a-2a** was not directly observed in this study, however a dimerization of **2a⁻** may result in a species with a similar structure to **2a-2a**.

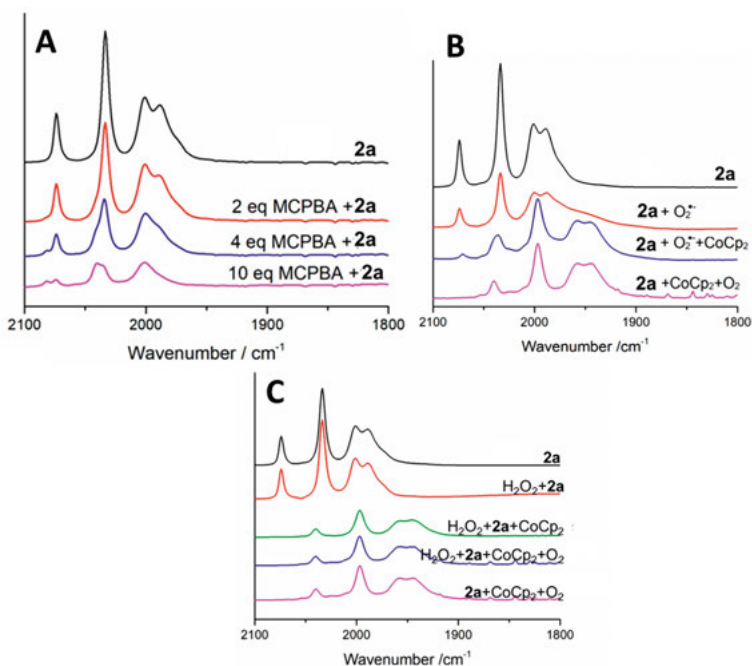
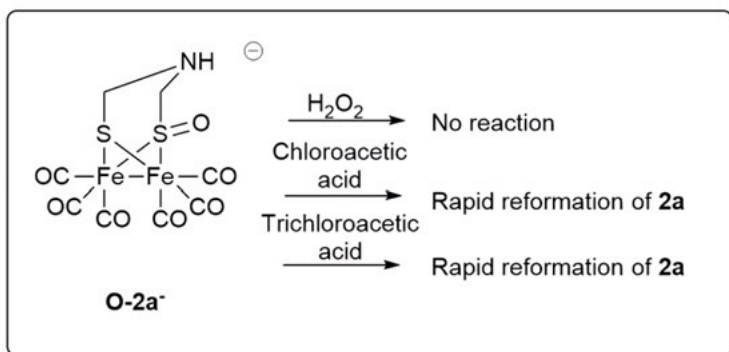


Figure 3.6. Reactivity of **2a** with mCPBA, superoxide, H₂O₂. **Panel A:** reactivity of **2a** with the oxygen transfer agent mCPBA. **Panel B:** reactivity of **2a** with superoxide (O₂⁻). **Panel C:** reactivity of **2a** with hydrogen peroxide. Reproduced from reference 71 with permission from the Royal Society of Chemistry.

Superoxide was added to **2a** to test if it could be a ROS responsible for the oxygenation of **2a** under reductive conditions. A new, broad FTIR signal was observed between 1980 cm⁻¹-1900 cm⁻¹ which remained for 20 hours (figure 3.6 panel B), indicating a lack of reversibility in contrast to the reversibility observed when **2a** is mixed with CoCp₂ and O₂. We therefore concluded that O₂⁻ was not involved in the formation of **O-2a**⁻. In addition to this, no change was observed in the FTIR spectrum when H₂O₂ was mixed with **2a**. ROS are therefore unlikely to be involved in the formation of **O-2a**⁻ (figure 3.6 panel C).

When **O-2a**⁻ was incubated for 20 hours in the glovebox, 30 % of **2a** was recovered. Furthermore, during this time, new carbonyl features were observed indicating the formation of intermediate species. Additionally, a new broad IR band attributable to H₂O was observed during the deoxygenation process. Further, **O-2a**⁻ was regenerated by the addition of fresh CoCp₂ and O₂. When protons were added to **O-2a**⁻, **2a** was recovered more rapidly and in higher yield (~60 %) than in the absence of protons. Protons therefore enable the deoxygenation process while preventing damage to the complex at room temperature (figure 3.7).



Scheme 3.5. Summary of the reaction of **O-2a⁻** with hydrogen peroxide, chloroacetic acid and trichloroacetic acid.

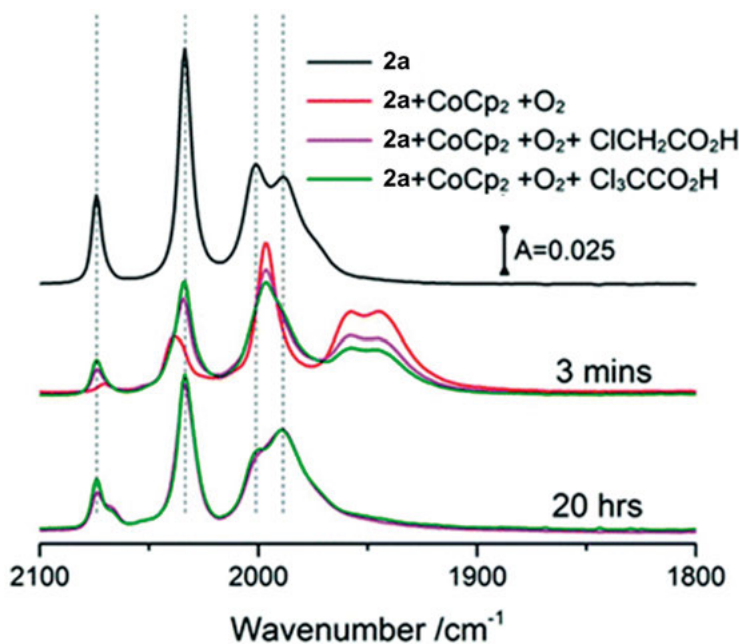


Figure 3.7. Reactivity of **2a** with acid. **Top:** **2a** reference spectrum (black spectrum). **Middle:** FTIR spectra 3 minutes after exposure of **2a** to CoCp₂ in the presence of oxygen (red spectrum), after exposure of **2a** to CoCp₂ in the presence of oxygen and chloroacetic acid (magenta spectrum), after exposure of **2a** to CoCp₂ in the presence of oxygen and trichloroacetic acid (green spectrum). **Bottom:** FTIR spectra 20 hours after exposure of **2a** to CoCp₂ in the presence of oxygen and chloroacetic acid (magenta spectrum), after exposure of **2a** to CoCp₂ in the presence of oxygen and trichloroacetic acid (green spectrum). Reproduced from reference 71 with permission from the Royal Society of Chemistry.

3.4 Comparison of **1a** and **2a**

The reduction potential of Fe(I)Fe(I)/Fe(I)Fe(0) is more negative than CoCp₂, meaning that CoCp₂ cannot reduce **1a**. It is therefore unlikely that the reduction chemistry occurs before oxygenation to **O-1a** or **O-2a**. Instead, to rationalize the observed reactivity we proposed a pre-equilibrium in which O₂ reversibly binds to **1a** and **2a** to form [O₂...**1a**] or [O₂...**2a**], albeit with a very low dissociation constant. The formation of [O₂...**1a**] is accompanied by an anodic shift in the potential of the diiron centre. This then facilitates sequential reduction and oxygenation reactions.

Schemes 3.2-3.5 summarise the reactivity of **1a** and **2a** reported in paper I. For the most part, **1a** and **2a** react in a very similar way. However, subtle differences in reactivity lead us to believe that the nitrogen bridgehead of **2a** plays a role in the reversibility of attack by oxygen. Notably, the product of the reduction of **1a** in the presence of oxygen to form **O-1a**⁻ has a poorly defined carbonyl band between 1950 cm⁻¹ and 1910 cm⁻¹ indicating the formation of side-products during the formation of **O-1a**⁻. In comparison, the FTIR spectrum of **O-2a**⁻ shows four rather clean peaks, and over the course of 20 minutes **2a** could be partially recovered, whereas **1a** fully degraded under the reducing and oxygenating conditions. In the presence of the oxygen transfer agent mCPBA, **1a** reacts to form **O-1a** which has also been reported by Darensbourg.¹⁴¹ However, when mCPBA was added to **2a**, almost no reaction occurred until at least 10 equivalents of mCPBA relative to **2a** were added. And the overall effect of adding the mCPBA to **2a** seems to be simply decomposition, rather than the formation of the expected **O-2a**. These results demonstrate that the outer-coordination sphere (-adt- vs -pdt-) mediates the reactivity of the complex with oxygen.

Despite these differences, **1a** and **2a** were both regenerated rapidly after the addition of acids to **O-1a**⁻ and **O-2a**⁻. Water was observed during the deoxygenation process of complex **O-2a**⁻, in keeping with earlier reports of electrocatalysis of the ORR by analogous complexes.⁵⁸ Table 3.1 summarises the FTIR spectra reported herein.

Table 1 – FTIR spectra discussed in paper I

Compound	Wavenumbers/cm ⁻¹	Solvent	Reference
1a	$\tilde{\nu}(\text{CO}) = 2074, 2033, 2000, 1989$	DCM	71
2a	$\tilde{\nu}(\text{CO}) = 2074, 2033, 2000, 1989$	DCM	71
1a⁻	$\tilde{\nu}(\text{CO}) = 2006, 1942, 1915, 1899$	THF	140
2a⁻	$\tilde{\nu}(\text{CO}) = 2006, 1942, 1910$	MeCN	143
O-1a	$\tilde{\nu}(\text{CO}) = 2083, 2045, 2017, 2000, \tilde{\nu}(\text{SO}) = 800\text{--}1020$	DCM	141
O-2a	Not reported		
O-1a⁻	$\tilde{\nu}(\text{CO}) = 2020, 1960, 1891, 1950\text{--}1910$ (broad shoulder)	DCM	71
O-2a⁻	$\tilde{\nu}(\text{CO}) = 2038, 1997, 1957, 1946, \tilde{\nu}(\text{SO}) = 900\text{--}1030$	DCM	71

3.5 Conclusions and outlook

[FeFe]-H₂ases and their mimics are oxygen sensitive and the project summarised in this chapter contributes to the understanding of oxygen sensitivity by examining the effect that the bridging ligand has on the reactivity of two bio-mimetic [FeFe]-H₂ase mimics with molecular oxygen and ROS. The goal was to examine the reactivity of the complexes **1a** and **2a** with molecular oxygen and ROS under neutral, reducing and acidic conditions. These goals were achieved by selecting reducing agents with appropriate reduction potential, CoCp₂. Potassium superoxide and hydrogen peroxide were used as ROS and were reacted with **1a** or **2a** in the presence or absence of reductant. The oxygen transfer reagent mCPBA was used in an attempt to generate the oxygenated species **O-1a** and **O-2a**.

FTIR, UV-Vis, and EPR spectroscopy were used to characterise the products of reduction or oxygenation. In addition to this, Paper I also includes some time-resolved FTIR and UV-vis spectroscopy which observes the formation of **O-2a⁻** over 90 minutes (2 minute time resolution). And the formation of the reduced oxygenated species **O-2a⁻** is further supported by DFT calculations and mass spectrometry.

The results of this study further solidify the idea that the nitrogen bridgehead in both the native [FeFe]-H₂ases and its model complexes plays a central role in protecting the cofactor from decomposition via oxygen attack. Additionally, this chemical approach, rather than the electrochemical approach previously used to study the oxygen tolerance of [FeFe]-H₂ase cofactor mimics enabled fine control of the ROS present at reducing conditions. Consequently we have been able to eliminate specific species as responsible for oxygenation of the model complexes. Furthermore, we were able to rationalise why **1a** and

2a did not react with the reductant CoCp₂ or oxygen alone, by suggesting that molecular oxygen reversibly binds to **1a** and **2a**, with a very low dissociation constant to form [O₂...**1a**] or [O₂...**2a**]. These adducts have a mild enough reduction potential that they may then be reduced by CoCp₂, facilitating further reduction and oxygenation reactions. Finally, the observed reformation of both **1a** and **2a** upon addition of acid to **O-1a**⁻ and **O-2a**⁻ respectively indicate that protons are also important to the deoxygenation process. This study may guide the design of oxygen tolerant catalysts for proton reduction. And may also solidify some directions for the engineering of oxygen tolerant [FeFe]-H₂ase cofactor mimics.

Chapter 4: Paper II Synthetic H-cluster

Introduction

Incorporation of metallocentres into small oligopeptides provides a middle-ground between investigations of redox active metalloenzymes and their organometallic analogues. The use of small peptides enables us to approach the design of molecular catalysts from new angles. For example, introducing mutations in the coordinating peptide, or introducing artificial amino acids to edit the secondary coordination sphere of a metallocentre.

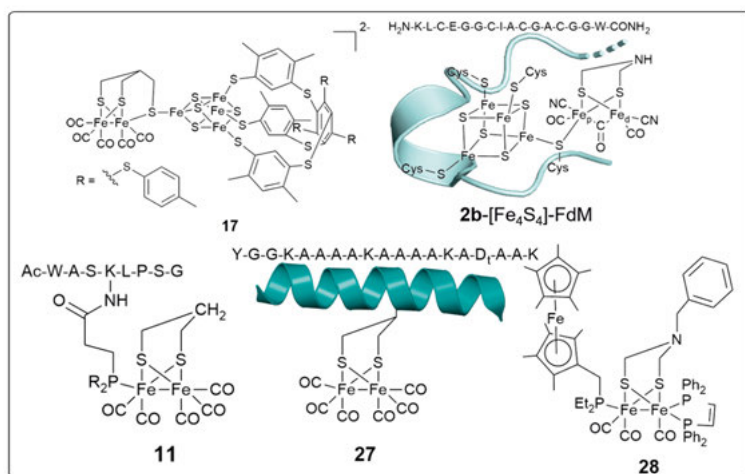
An example of this was demonstrated by Roy, Nguyen and co-workers in 2015 in which they coordinated a [FeFe]-H₂ase cofactor to an oligopeptide containing one artificial amino acid which incorporated phosphine functionality (scheme 4.1, **11**).⁸¹ This side-chain enabled coordination of the peptide directly to the iron centre of the [FeFe]-H₂ase cofactor mimic. The result was a [FeFe]-H₂ase cofactor mimic that was partially soluble in water and demonstrated catalytic turnover of protons to hydrogen at -2.36 V vs SHE (reported as -1.72 V vs Fc^{+/0} in a 3:2 MeCN:H₂O solvent mixture). Another example from Roy and Madden *et al*, demonstrated that it is possible to also use the dithiolato bridging moiety to bind the cofactor mimic to an alpha helical peptide (scheme 4.1, **27**). This resulted in a water soluble photocatalyst for hydrogen production.¹⁴⁵ Additional studies have also been carried out using peptides as scaffolds for other proton reduction catalysts, like cobaloximes, cobalt-porphyrins,¹⁴⁶⁻¹⁴⁸ and the nickel based Dubois catalysts described in chapter 1.^{102, 149, 150}

As discussed in chapter 1, incorporation of the catalytically inactive **2b**²⁻ into apo-HydA1 results in a semi-synthetic enzyme that is as active as the native enzyme.¹⁵¹ This highlights the importance of an outer coordination sphere for catalytic activity of the [FeFe]-H₂ase cofactor and its mimics. In addition to the outer coordination sphere, introduction of **2b**²⁻ into the active site pocket of the [FeFe]-H₂ase also fuses **2b**²⁻ to a redox active ligand, the [Fe₄S₄]-cluster. This has been mimicked by Pickett in the form of complex **17** which was already discussed in chapter 1. Another example is provided by complex **28** which uses decamethylferrocene as a redox active ligand. The latter was reported in 2012 and contains a nitrogen in the bridgehead ligand and the bidentate diphosphine ligand (dppv) also present in complex **9**.¹⁵² As catalytic activity can be induced by incorporating the organometallic cofactor into the [FeFe]-H₂ase active site, it follows that it may be possible to

create a miniaturised hydrogenase by combining the same organometallic co-factor into a pre-formed $[\text{Fe}_4\text{S}_4]$ -cluster supported by a small oligopeptide, complex **11**.

The aims of the project summarised in this chapter are:

- Reproduce the artificial maturation procedure using a $[\text{Fe}_4\text{S}_4]$ -cluster in an oligopeptide scaffold to synthesise the miniaturised hydrogenase **2b**- $[\text{Fe}_4\text{S}_4]$ -FdM.
- Investigate the effect of introducing the redox active ligand $[\text{Fe}_4\text{S}_4]$ -FdM on the structure of the $[\text{FeFe}]$ - H_2 ase cofactor mimic.
- Investigate the proton reduction activity of **2b**- $[\text{Fe}_4\text{S}_4]$ -FdM.



Scheme 4.1. Selected examples of $[\text{FeFe}]$ hydrogenases mimics featuring redox active ligands, and/or peptides. **17** Pickett *et al.*'s free standing H-cluster mimic already discussed in chapter 1; **2b**- $[\text{Fe}_4\text{S}_4]$ -FdM schematic diagram of the synthetic $[\text{FeFe}]$ - H_2 ase H-cluster mimic reported in paper II; **11** an example of a $[\text{FeFe}]$ - H_2 ase cofactor mimic bound to a short oligopeptide via the phosphine side chain of an artificial amino acid; **27** an example of a $[\text{FeFe}]$ - H_2 ase cofactor mimic bound to an alpha-helical peptide via the carbon bridgehead of the propane dithiolato bridging ligand; **28** $[\text{FeFe}]$ - H_2 ase mimic that incorporates several design principles in order to mimic the functionalities present in the $[\text{FeFe}]$ - H_2 ase active site, notably acid-base functionality and a redox active ligand (decamethyl ferrocene).

4.1 Synthesis of the $[\text{Fe}_4\text{S}_4]$ -cluster

The first step in the synthesis of the miniaturised hydrogenase is to make the $[\text{Fe}_4\text{S}_4]^{2+}$ -cluster. In this study we used the 16 amino acid polypeptide based on the $[\text{Fe}_4\text{S}_4]$ binding motif of *peptococcus aerogenes* ferredoxin I, here on abbreviated to FdM. This had already been reported as a ferredoxin mimic by Dutton *et al.*^{94, 153} FdM contains four cysteine residues that can coordinate to the iron ions of the $[\text{Fe}_4\text{S}_4]^{2+}$ -cluster analogously to the binding of cysteine

residues to the iron ions in the $[\text{Fe}_4\text{S}_4]^{2+}$ -cluster in $[\text{FeFe}]\text{-H}_2\text{ases}$ such as HydA1.

The formation of $[\text{Fe}_4\text{S}_4]^{2+}$ -FdM is extremely sensitive to oxygen, so was carried out under strict anaerobic conditions. During standard experiments, the FdM maquette was dissolved to make a concentration of 1 mM in a 50 mM solution of HEPES buffer at pH8. This stock solution was further diluted using the HEPES buffer, so that the final concentration was 60 μM (although it is possible to work at higher concentrations, for example when preparing EPR samples). Following this dilution, β -mercaptoethanol was added to the experiments in order to reduce any disulphide bonds between the cysteine groups of the polypeptide that would otherwise prevent coordination of FdM to the iron ions which were added next. After incubation for 2 hours at room temperature, Fe(III)Cl_3 , $\text{Fe(II)SO}_4\cdot(\text{NH}_4)_2\text{SO}_4\cdot 6\text{H}_2\text{O}$ (Mohr's salt), and Na_2S were added to the solution so that the Fe(II) and Fe(III) reagents had a final concentration of 120 μM (i.e. 2 molar equivalents with respect to FdM) and Na_2S had a final concentration of 240 μM (i.e. 4 molar equivalents with respect to FdM). Over the course of 2 hours incubation the FdM, iron ions and sulphide self-assembled to form $[\text{Fe}_4\text{S}_4]^{2+}$ -FdM.

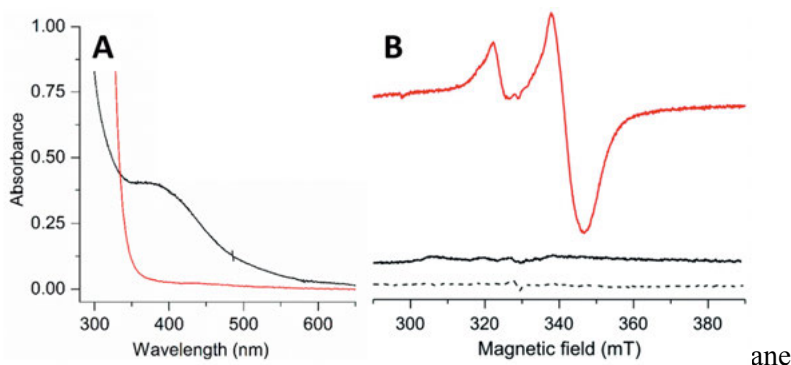


Figure 4.1. Spectroscopic characterisation of the $[\text{Fe}_4\text{S}_4]$ -cluster. **Panel A:** UV-Vis spectra of $[\text{Fe}_4\text{S}_4]^{2+}$ -FdM (black spectrum), and $[\text{Fe}_4\text{S}_4]^+$ -FdM (red spectrum); **Panel B:** EPR spectra of $[\text{Fe}_4\text{S}_4]^{2+}$ -FdM (black spectrum), and $[\text{Fe}_4\text{S}_4]^+$ -FdM (red spectrum). Reproduced from reference 56 with permission from the Royal Society of Chemistry.

The formation of $[\text{Fe}_4\text{S}_4]^{2+}$ -FdM is confirmed by UV-Vis and EPR spectroscopy. As prepared, $[\text{Fe}_4\text{S}_4]^{2+}$ -FdM shows a broad absorption in the UV-vis spectrum at 385 nm with absorption coefficient $\epsilon_{385} = 13,000 \text{ L mol}^{-1} \text{ cm}^{-1}$ (figure 4.1, panel A). This is in agreement with the previous reports from Dutton *et al.*,^{94, 153} and with studies of $[\text{Fe}_4\text{S}_4]$ -clusters present in $[\text{FeFe}]\text{-H}_2\text{ase}$ enzymes.^{154, 155} EPR spectra of the as prepared cluster $[\text{Fe}_4\text{S}_4]^{2+}$ -FdM show no signal indicating that it is a diamagnetic species. Upon reduction by sodium dithionite to form the reduced cluster $[\text{Fe}_4\text{S}_4]^+$ -FdM, the UV-Vis absorption disappears. However, a rhombic signal becomes visible in the EPR spectrum

with apparent g-values $g_1 = 2.06$, $g_2 = 1.93$ and $g_3 = 1.89$ (figure 4.1, panel B). This rhombic signal is also in agreement with Dutton's reports and with other reports of $[\text{Fe}_4\text{S}_4]^+$ -FdM in the literature.¹⁵⁴ Furthermore, spin quantification of the signal generated by $[\text{Fe}_4\text{S}_4]^+$ -FdM showed that 55 ± 10 % of the $[\text{Fe}_4\text{S}_4]^{2+}$ -FdM was reduced to the EPR active species $[\text{Fe}_4\text{S}_4]^+$ -FdM.

Interestingly, when the experiment was carried out using β -mercaptoethanol in the absence of FdM, we observed an absorption in the UV-vis spectrum at 385 nm indicative of the formation of $[\text{Fe}_4\text{S}_4]^{2+}$, however upon reduction no signal in the EPR was observed. These data indicate that $[\text{Fe}_4\text{S}_4]^{2+}$ does form in the presence of β -mercaptoethanol, but that the peptide scaffold, FdM, is a requirement for the clusters stability upon reduction.

4.2 Maturation of the $[\text{Fe}_4\text{S}_4]$ -cluster to form a miniaturised hydrogenase

One goal of this paper was to determine if such a $[\text{Fe}_4\text{S}_4]$ -cluster could be linked with $2\mathbf{b}^{2-}$ (or "artificially matured"), in an analogous way to the H-cluster in HydA1; to produce a miniaturised hydrogenase.¹⁵¹

A freshly prepared solution of $[\text{Fe}_4\text{S}_4]^{2+}$ -FdM was treated with sodium dithionite (1200 μM , effectively 20 molar equivalents relative to FdM) to generate $[\text{Fe}_4\text{S}_4]^+$ -FdM. Complex $2\mathbf{b}^{2-}$ was added to the solution containing the reduced cluster so that the final concentration of $2\mathbf{b}^{2-}$ was 60 μM (1 molar equivalent relative to FdM). The resulting solution was probed by FTIR and EPR spectroscopy, and the structural assignment supported by DFT calculations. We observed several difference between the FTIR spectra of $2\mathbf{b}^{2-}$ and $2\mathbf{b}$ - $[\text{Fe}_4\text{S}_4]$ -FdM (figure 4.2). The three important differences are:

- The disappearance of one terminal carbonyl band at 1908 cm^{-1} , which indicates the loss a terminal carbonyl. This is also observed during artificial maturation of CrHydA1. It is also chemically expected because what is effectively happening is a ligand substitution of a CO-ligand in $2\mathbf{b}^{2-}$ with a $[\text{Fe}_4\text{S}_4]$ -cluster.
- Appearance of a μ -CO band at 1792 cm^{-1} . The appearance of a μ -CO band is also observed during artificial maturation of HydA1 because the ligand substitution is accompanied by a rotation of the diiron centre of $2\mathbf{b}^{2-}$ and the formation of a bridging bond between one of the CO-ligands and the two iron ions to form a \mathbf{H}_{ox} -like state.
- Splitting of the cyanide bands in the FTIR spectrum. That is the loss of the cyanide band at 2056 cm^{-1} and the growth of two new bands at 2036 and 2078 cm^{-1} . This supports the idea of the loss of symmetry around the diiron centre of $2\mathbf{b}^{2-}$.

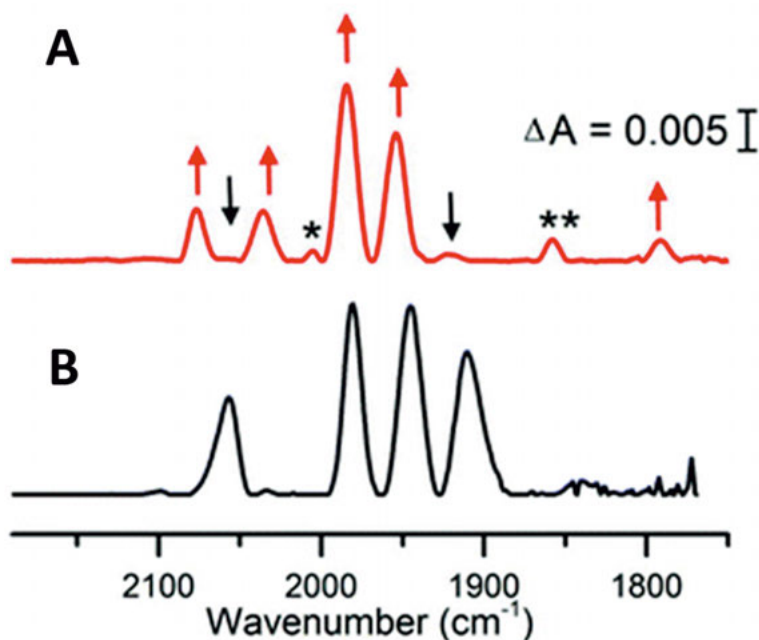


Figure 4.2. Changes in FTIR spectrum between **2b**²⁻ and **2b**-[Fe₄S₄]-FdM. **Panel A:** FTIR spectrum of the miniaturised hydrogenase **2b**-[Fe₄S₄]-FdM, the black arrows indicate the loss of the terminal carbonyl band at 1908 cm⁻¹ and the loss of a cyanide band at 2056 cm⁻¹ which is replaced by two new cyanide bands. The red arrows indicate new bands in the FTIR spectrum. Starred bands indicate bands that we were unable to firmly assign; **Panel B:** FTIR reference spectrum of **2b**²⁻. Reproduced from reference 56 with permission from the Royal Society of Chemistry.

The FTIR data is already rather compelling, and the presence of carbonyl and cyanide bands in the product FTIR spectrum demonstrates the continued presence of iron-carbon bonds in the complex. However, a competent chemist should never rely on just one spectroscopic method to characterise their compounds! For this reason, the formation of **2b**-[Fe₄S₄]-FdM was monitored by; observing changes in the EPR spectrum upon titration of **2b**²⁻ into [Fe₄S₄]⁺-FdM; by deoxyhemoglobin assay and UV-vis; and by monitoring the accompanying hydrogen production by gas chromatography.

2b²⁻ was titrated into freshly prepared samples of [Fe₄S₄]⁺-FdM and EPR samples were collected for the titrations points containing 0 eq, 0.5 eq and 1 eq of **2b**²⁻ relative to [Fe₄S₄]⁺-FdM (figure 4.3). The results showed that the rhombic signal described above was still present when 0.5 eq **2b**²⁻ was added, but had almost completely disappeared when stoichiometric amounts of **2b**²⁻ were added to [Fe₄S₄]⁺-FdM. This disappearance of the EPR signal indicated that the starting material, already assigned as a S = ½ species became an overall S = 0 species through the coupling of [Fe₄S₄]⁺-FdM to **2b**²⁻. During the coupling of [Fe₄S₄]⁺-FdM to **2b**²⁻ small amounts of H₂ were observed by GC,

implying that H^+ is an electron acceptor during this reaction. Further, this suggests that $\mathbf{2b}^{2-}$ is oxidised to mixed valent Fe(I)Fe(II) during the coupling process to create a species very similar to \mathbf{H}_{ox} in geometric (FTIR) structure. Albeit, the EPR spectra suggests that the electronic structure is closer to \mathbf{H}_{red} or $\mathbf{H}_{\text{red}}\mathbf{H}^+$ with a reduced $[\text{Fe}_4\text{S}_4]$ -cluster.

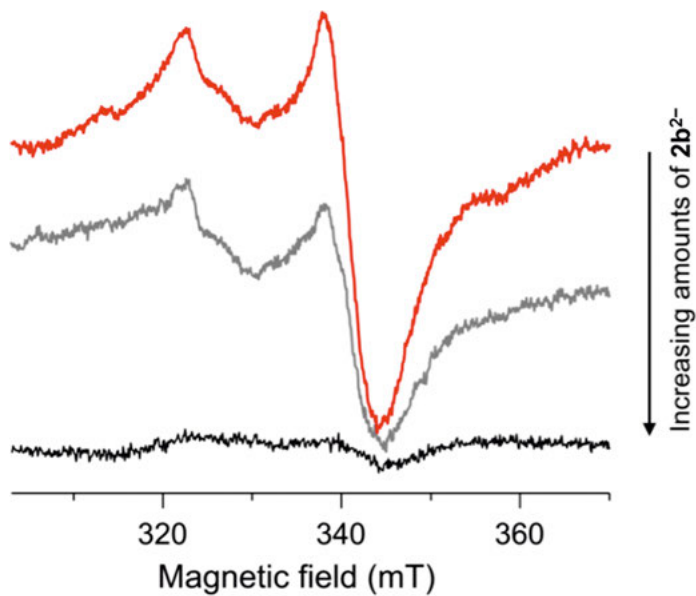


Figure 4.3. EPR spectra monitoring the formation of $\mathbf{2b}$ - $[\text{Fe}_4\text{S}_4]$ -FdM through titration of $\mathbf{2b}^{2-}$ into $[\text{Fe}_4\text{S}_4]^+$ -FdM. Titration points, 0 eq of $\mathbf{2b}^{2-}$ (red spectrum), 0.5 eq of $\mathbf{2b}^{2-}$ (grey spectrum), 1 eq of $\mathbf{2b}^{2-}$ (black spectrum). Reproduced from reference 56 with permission from the Royal Society of Chemistry.

CO is expected to be released during the ligand substitution that occurs upon mixing $\mathbf{2b}^{2-}$ and $[\text{Fe}_4\text{S}_4]^+$ -FdM. The amount of CO can be determined by observing the shift in the Soret band of deoxyhemoglobin caused by binding of CO to deoxyhemoglobin when it is added to the reaction mixture. The deoxyhemoglobin assay was carried out at various concentrations of $\mathbf{2b}^{2-}$ and $[\text{Fe}_4\text{S}_4]^+$ -FdM, and we observed that 0.67 mol of CO is released during the ligand substitution process, in agreement with the EPR data that showed that only 55 % of the as prepared $[\text{Fe}_4\text{S}_4]^{2+}$ -FdM was reduced by dithionite to the more nucleophilic $[\text{Fe}_4\text{S}_4]^+$ -FdM. All of this data together led us to propose the \mathbf{H}_{ox} -like structure shown in scheme 4.1, $\mathbf{2b}$ - $[\text{Fe}_4\text{S}_4]$ -FdM, although the EPR silent nature of the as prepared $\mathbf{2b}$ - $[\text{Fe}_4\text{S}_4]$ -FdM is suggestive of an overall oxidation state similar to \mathbf{H}_{red} or $\mathbf{H}_{\text{red}}\mathbf{H}^+$.

3.3 Activity of **2b**-[Fe₄S₄]-FdM

The activity of **2b**-[Fe₄S₄]-FdM for proton reduction was monitored by observing the reaction with reduced methylviologen (MV) which has a mild reduction potential of $E_{0MV^{+/2+}} = -0.45$ V vs SHE. **2b**-[Fe₄S₄]-FdM shows 10 turnovers over the course of 1 hour (figure 4.4, panel A), after which time, it decomposed as demonstrated by loss of carbonyl bands in the FTIR spectrum. This turnover number of 10 is modest as compared to HydA1, however **2b**²⁻ in isolation demonstrates no catalytic activity at all (figure 4.4, panel B). This result shows that introduction of an electron relay in the outer coordination sphere can enable catalytic activity of the dicyanide mimic **2b**²⁻.

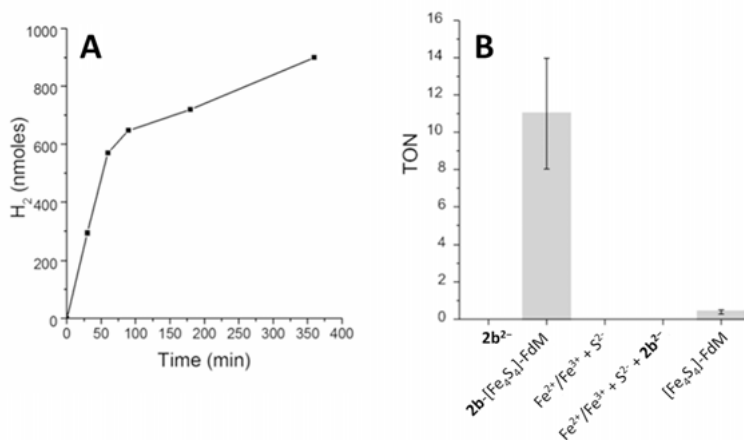


Figure 4.4. Testing the catalytic activity of **2b**-[Fe₄S₄]-FdM. **Panel A:** Hydrogen evolution activity of **2b**-[Fe₄S₄]-FdM monitored over 6 hours; **Panel B:** hydrogen evolution activity of **2b**-[Fe₄S₄]-FdM compared to **2b**²⁻, the [Fe₄S₄]²⁺ cluster in absence of FdM, A mixture of [Fe₄S₄]²⁺ and **2b**²⁻ in absence of FdM, and [Fe₄S₄]⁺-FdM in absence of **2b**²⁻. Reproduced from reference 56 with permission from the Royal Society of Chemistry.

3.4 Conclusions and outlook

In summary, we have reproduced the chemistry observed during artificial maturation of apo-HydA1 by coupling a pre-assembled [Fe₄S₄]⁺-cluster with **2b**²⁻ under reducing conditions to form the a synthetic H-cluster in a H_{ox}-like state. The complex displayed modest proton reduction activity. This was confirmed by FTIR, UV-vis and EPR spectroscopy and the results were supported by DFT calculations. Furthermore, we have demonstrated that the presence of the [Fe₄S₄]-cluster plays a role in imparting catalytic activity to **2b**²⁻. This result further informs on the importance of redox active ligands as a design consideration for [FeFe]-H₂ase cofactor mimics.

Using FdM maquettes to form the $[\text{Fe}_4\text{S}_4]$ -cluster enabled the formation of a water soluble molecular catalyst for proton reduction. Furthermore the use of FdM maquettes can provide new and exciting design pathways, including introducing mutations to the peptide (both natural amino acids and artificial amino acids), extending the peptide to include groups that may coordinate the cyanide ligands, and possibly even exchanging the iron or sulphur sites in the $[\text{Fe}_4\text{S}_4]$ -cluster.

Chapter 5: Paper III Protecting the Cyanide ligands

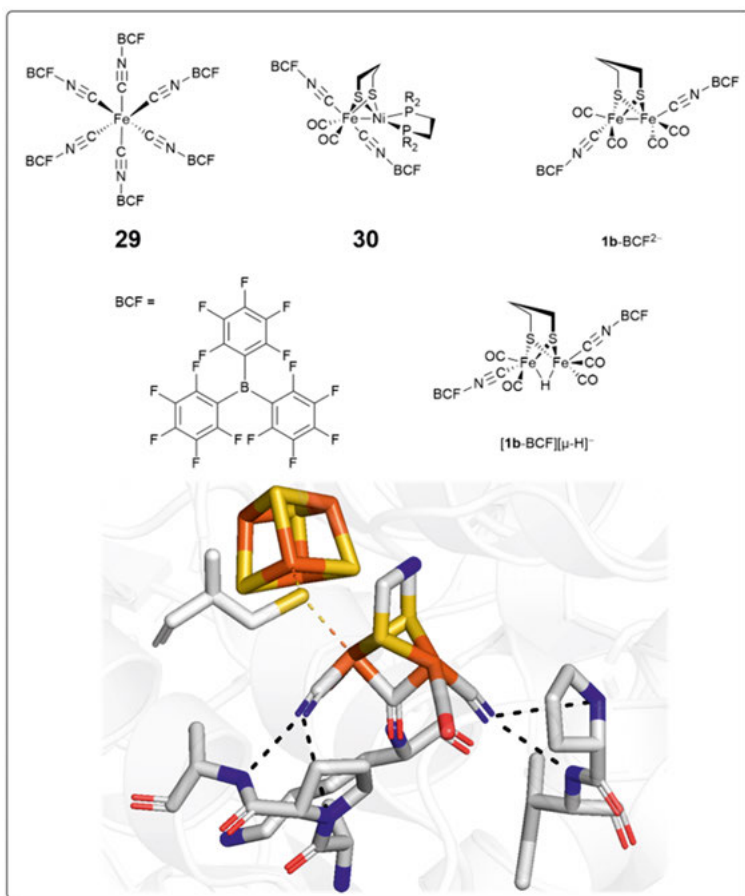
Introduction

As discussed in chapters 1 and 3, $\mathbf{2b}^{2-}$ is unstable in solution under acidic and reducing conditions, but when inserted into apo-[FeFe]-H₂ase it generates a semi-synthetic hydrogenase as active as the native enzyme. This finding highlights the importance of an outer coordination sphere for the function of $\mathbf{2b}^{2-}$ and related mimics.

The addition of Lewis acids has been reported to enable tuning of the electron density and catalytic properties of various cyanide and nitrile containing metal complexes. For example, the study of ferrocyanide by McNicholas *et al* demonstrated that it is possible to utilise the electron withdrawing effect of a bulky Lewis acid, such as tris(pentafluorophenyl)borane (BCF), to tune the reduction potential of such a complex over 2.1 V, without affecting outer-sphere electron transfer (complex **29**, scheme 5.1).¹⁵⁶

The coordination of the borane to the cyanide ligand mimics the hydrogen bonding of the protein to the cyanide ligands of the [FeFe]-H₂ase cofactor (scheme 5.1). Furthermore, this capping of the cyanide ligands was also shown to enable the synthesis of a cyanide containing [NiFe]-H₂ase mimic (complex **30**, scheme 5.1), which was electrocatalytically active for hydrogen oxidation.¹⁵⁷

In paper III we showed that the protection of the cyanide ligands enabled catalytic activity of the dicyanide [FeFe]-H₂ase cofactor mimic, $\mathbf{1b}^{2-}$, which has previously been challenging. We revisited the previously reported [FeFe]-H₂ase cofactor mimic in which the cyanide ligands of $\mathbf{1b}^{2-}$ are capped with BCF, to make $\mathbf{1b-BCF}^{2-}$ (scheme 5.1).^{57, 158} We chose the mimic with the carbon bridgehead in the bridging ligand, this allowed use to probe the mimic and its redox and hydride chemistry without interference from protonation from the nitrogen bridgehead of $\mathbf{2b}^{2-}$. As reported by Manor *et al*.¹⁵⁸ the borane caps the cyanide ligands, so that they are protected from decomposition by protonation. This approach also enabled formation of the corresponding bridging hydride complex ($[\mathbf{1b-BCF}][\mu\text{-H}]^-$, scheme 5.1).⁵⁷



Scheme 5.1. Some example of complexes that utilise borane caps to tune the electron density on the metal centre. **29** ferrocyanide capped with BCF ligand; **30** [NiFe]-H₂ase cofactor mimic where the cyanide ligands are capped with BCF; **1b-BCF²⁻**, **1b²⁻** capped with BCF; BCF: chemical structure of the capping ligand tris(pentafluorophenyl)borane; **[1b-BCF][μ-H]⁻**, bridging hydride observed in this study; bottom: crystal structure of the active site of a typical [FeFe]-H₂ase, adapted from crystal structure of the [FeFe]-H₂ase from *Desulfovibrio desulfuricans* in the H_{inact} state in the Protein Data Bank entry 6SG2,³⁹ the only covalent bond holding the cofactor in the active site pocket is provided by a cysteine bridging the cofactor and the [Fe₄S₄]-cluster. Hydrogen bonds also hold the cofactor in the active site pocket, and these are indicated by black dashed lines.

The aims of paper III were to:

- Revisit the already reported **1b**-BCF²⁻ in more detail and probe for proton reduction activity
- Investigate the oxidation chemistry of **1b**-BCF²⁻ and [**1b**-BCF][μ-H]⁻
- Investigate the reduction chemistry of **1b**-BCF²⁻ and [**1b**-BCF][μ-H]⁻
- Propose a reaction scheme for proton reduction catalysis by **1b**-BCF²⁻.

These aims were achieved through cyclic voltammetry and spectroscopic investigations using FTIR, UV-Vis, EPR and X-ray absorption spectroscopy.

5.1 Synthesis of borane capped mimic and formation of the bridging hydride

Upon capping the cyanide ligands of **1b**²⁻ with the BCF following the reported literature procedure, I was able to isolate an orange microcrystalline powder (**1b**-BCF²⁻, scheme 5.1) which displayed an FTIR spectrum matching that reported by Manor *et al*, in which the carbonyl bands shifted by around 30 cm⁻¹ compared to **1b**²⁻, from 1965-1886 cm⁻¹ to 1989-1920 cm⁻¹ (figure 5.1). This is expected because of the electron withdrawing effect of the Lewis acid, which is made more significant by the fluorine substitution on the phenyl rings; there are 15 fluorine groups on each BCF ligand. The cyanide band at 2071 cm⁻¹ in **1b**²⁻ was shifted to even higher wavenumbers to 2134 cm⁻¹ (figure 5.1). We attributed this more dramatic shift to the stronger influence of the BCF ligands on the cyanide ligands vibrational bands due to direct through bond interactions.

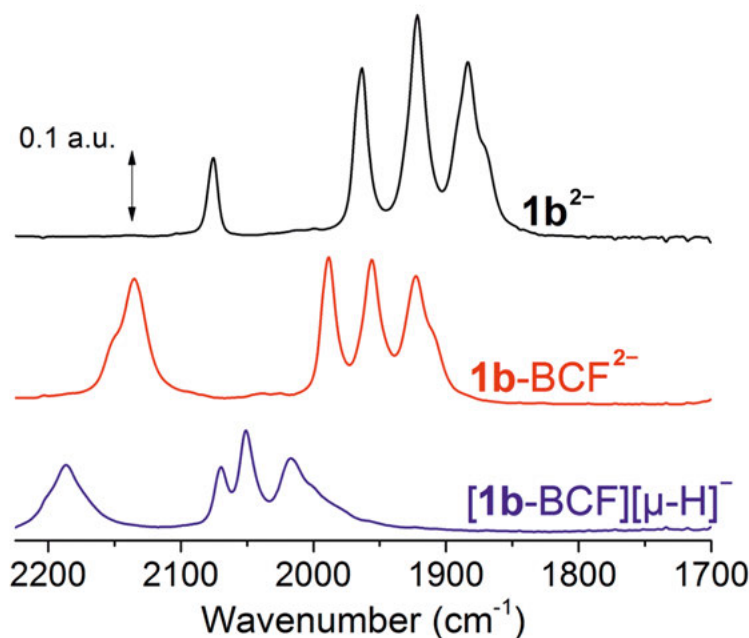


Figure 5.1. FTIR spectra of compounds reported in this study. 5 mM $\mathbf{1b}^{2-}$, (black spectrum) the dicyanide substituted [FeFe]-H₂ase cofactor mimic with the carbon bridgehead shown in figure 1.6 with the cyanide band at 2071 cm⁻¹ and carbonyl bands at 1924 cm⁻¹, 1924 cm⁻¹ and 1886 cm⁻¹; $\mathbf{1b-BCF}^{2-}$ (red spectrum) borane capped dicyanide [FeFe]-H₂ase mimic shows a clear shift in the cyanide and carbonyl bands to 2134 cm⁻¹, 1989 cm⁻¹, 1954 cm⁻¹, 1920 cm⁻¹; hydride species $[\mathbf{1b-BCF}][\mu\text{-H}]^-$ (blue spectrum) produced when 4 equivalents of HCl are added to $\mathbf{1b-BCF}^{2-}$, the cyanide band has moved to 2186 cm⁻¹ and the carbonyl bands have moved to 2070 cm⁻¹, 2050 cm⁻¹, and 2020 cm⁻¹, this hypsochromic shift in the wavenumber is indicative of oxidative addition of the hydrogen across the Fe-Fe bond. Reproduced from reference 57 with permission from the Royal Society of Chemistry.

Titration of HCl into a solution of $\mathbf{1b-BCF}^{2-}$ resulted in the formation of the diferrous bridging hydride, $[\mathbf{1b-BCF}][\mu\text{-H}]^-$ (figure 5.1). During the titration, the absorbance at 346 nm in the UV-vis spectrum disappeared. In agreement with previous reports of bridging hydride formation of some phosphine substituted [FeFe]-H₂ase cofactor mimics.¹⁵⁹ The FTIR spectrum showed a hypsochromic shift of 90 cm⁻¹, suggestive of oxidative addition of the proton across the [FeFe] bond to form the bridging hydride with oxidation states [Fe(II)Fe(II)]. This is an important observation because bridging hydrides are present in some of the proposed intermediate states of the catalytic cycle B (figure 1.4). It is also an unusual example of a bridging hydride observed in a dicyanide [FeFe]-H₂ase cofactor mimic. $[\mathbf{1b-BCF}][\mu\text{-H}]^-$ was stable in solution on a few hours time scale, which allowed use to explore its properties using X-ray absorption spectroscopy (figure 5.2). The consistent shape of the

XANES spectra among the samples **1b**-BCF²⁻ and [**1b**-BCF][μ -H]⁻ as compare to the reference compounds **1a** and **1b**²⁻ indicates the molecular integrity of the complexes in the XAS samples. Both **1b**-BCF²⁻ and [**1b**-BCF][μ -H]⁻, and the reference complexes display similar K-edge values, even among the samples containing the hydride ligand. The latter are formally diferrous Fe(II)Fe(II), hydride formation is accompanied by a large shift in the carbonyl and cyanide bands in the FTIR spectra (figure 5.2). This phenomenon was observed in the analogous diphosphine complex **8**, and may be explained by the protic nature μ -hydride ligand in the hydride of complex **8**, as shown by the DFT calculations displaying almost zero Mulliken charge on the hydrogen.^{76, 121}

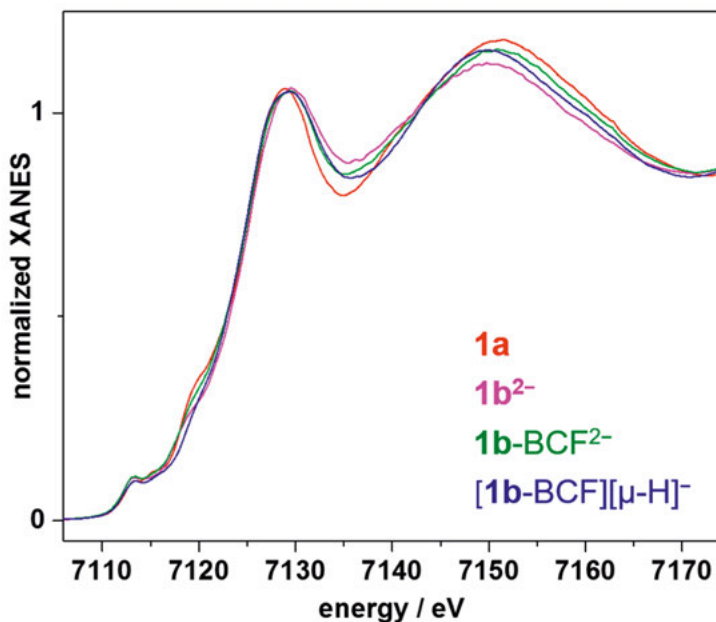


Figure 5.2. X-ray absorption spectra in the XANES region. Spectra show **1a** (red spectrum), **1b**²⁻ (magenta spectrum), **1b**-BCF²⁻ (green spectrum), [**1b**-BCF][μ -H]⁻ (blue spectrum). Prepared at Uppsala University by me with a total iron concentration of 10 mM, and measured at beamline KMC-3 at the BESSY-II synchrotron by Michael Haumann. Reproduced from reference 57 with permission from the Royal Society of Chemistry.

5.2 Oxidation chemistry

Cyclic voltammetry of **1b**-BCF²⁻ showed that there is an irreversible electrochemical oxidation at -0.76 V vs SHE (reported as -0.12 V vs Fc^{+/0}) (figure 5.3, panel A). We attribute this to the oxidation of the complex from Fe(I)Fe(I) to Fe(I)Fe(II), which is likely accompanied by a chemical change as in-

indicated by the irreversible oxidation. Both of these oxidation states are biologically relevant and proposed in the catalytic Cycles A and B, figures 1.4 and 1.5. As HCl is added to form $[\mathbf{1b}\text{-BCF}][\mu\text{-H}]^-$ in situ as demonstrated by the spectroscopy presented above, we observe that the oxidation at -0.12 V diminishes and a reversible oxidation at -0.48 V is observed (figure 5.3, panel A). We assign this reversible oxidation as the oxidation of the bridging hydride from Fe(II)Fe(II) to Fe(II)Fe(III). However, despite repeated efforts I was unable to observe this proposed mixed valence species spectroscopically.

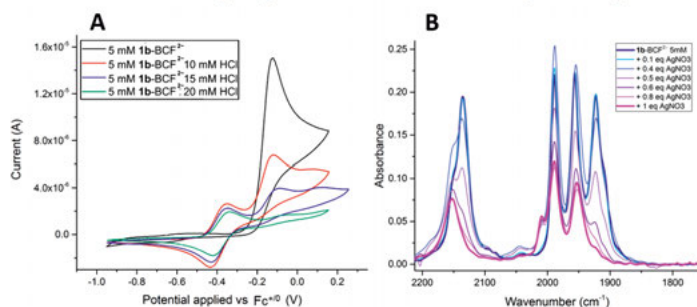


Figure 5.3. Oxidation chemistry of $\mathbf{1b}\text{-BCF}^{2-}$. **Panel A:** CVs of the oxidation of $\mathbf{1b}\text{-BCF}^{2-}$ in acetonitrile in the range -0.9 V vs $\text{Fc}^{+/0}$ to $+0.2$ V vs $\text{Fc}^{+/0}$; 5 mM $\mathbf{1b}\text{-BCF}^{2-}$ (black trace); $\mathbf{1b}\text{-BCF}^{2-}$ and 10 mM HCl (red trace); 5 mM $\mathbf{1b}\text{-BCF}^{2-}$ 15 mM HCl (blue trace); 5 mM $\mathbf{1b}\text{-BCF}^{2-}$ 20 mM HCl (green trace). **Panel B:** 5 mM $\mathbf{1b}\text{-BCF}^{2-}$ (thick blue trace) to 5 mM $\mathbf{1b}\text{-BCF}^{2-}$ and 5 mM AgNO_3 (thick magenta trace) shows that only 1 eq of AgNO_3 is needed for full oxidation from $\mathbf{1b}\text{-BCF}^{2-}$ to $\mathbf{31}$. Reproduced from reference 57 with permission from the Royal Society of Chemistry.

I was able to collect spectroscopic data on the oxidation of $\mathbf{1b}\text{-BCF}^{2-}$. Based on the cyclic voltammogram, silver nitrate was selected as a chemical oxidant ($E(\text{Ag}|\text{Ag}^+) = +0.04$ V vs $\text{Fc}^{+/0}$). When silver nitrate was titrated into a solution of $\mathbf{1b}\text{-BCF}^{2-}$, a new complex ($\mathbf{31}$) was formed, with wavenumbers 2009 cm^{-1} , 1989 cm^{-1} , 1953 cm^{-1} , 2151 cm^{-1} (figure 5.3, panel B). A distinct shift in K-edge was observed in the XAS spectra when $\mathbf{1b}\text{-BCF}^{2-}$ was oxidised to $\mathbf{31}$, which is in agreement with more oxidised Fe centres (figure 5.4). The reported FTIR and XAS spectra of $\mathbf{31}$ are indicative of oxidation; however, we were unable to structurally assign $\mathbf{31}$. The observation of a chemically different species upon oxidation by AgNO_3 is in agreement with the observed irreversible electrochemical oxidation in the CV trace of $\mathbf{1b}\text{-BCF}^{2-}$. Complex $\mathbf{31}$ is EPR silent which does not match with our initial assignment of a one electron oxidation to yield $\mathbf{1b}\text{-BCF}^-$, however titration of silver nitrate into $\mathbf{1b}\text{-BCF}^{2-}$ showed that only 1 eq of oxidant is needed to form $\mathbf{31}$. So this means that the 1 electron oxidation of $\mathbf{1b}\text{-BCF}^{2-}$ is likely accompanied by a rapid chemical change to $\mathbf{31}$.

Subsequently, I carried out a trapping experiment where I mixed $\mathbf{1b}\text{-BCF}^{2-}$ and silver nitrate at -70°C . This revealed a potential intermediate with an isotropic EPR signal at $g = 2.02$. We very tentatively assigned this to Fe(I)Fe(II)

which then at room temperature goes on to form complex **31**. When **31** was exposed to the strong chemical reductant CoCp*, **1b-BCF**²⁻ was partially re-formed as shown by FTIR. This demonstrates that although the oxidation of **1b-BCF**²⁻ is electrochemically irreversible, there is some chemical reversibility.

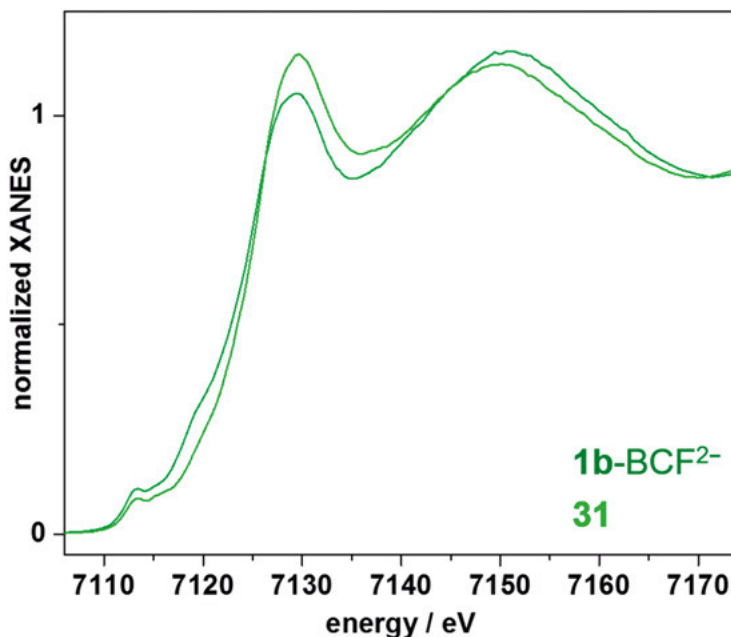


Figure 5.4. X-ray absorption spectra in the XANES region. Spectra show **1b-BCF**²⁻ (dark green spectrum), and the oxidation product, **31** (light green spectrum). Prepared at Uppsala University by me with a total iron concentration of 10 mM, and measured at beamline KMC-3 at the BESSY-II synchrotron by Michael Haumann. Reproduced from reference 57 with permission from the Royal Society of Chemistry.

5.3 Reduction chemistry

The oxidation chemistry of this complex is unusual, but we also wanted to elucidate the reduction chemistry and probe the possibility of electrochemical proton reduction (Figure 5.5, panel A). The reduction of **1b-BCF**²⁻ shows two pseudo reversible reductions at -2.15 V vs SHE (reported as -1.51 V vs $\text{Fc}^{+/0}$) and -2.25 V vs SHE (reported as -1.71 V vs $\text{Fc}^{+/0}$). Which we assign to reduction from Fe(I)Fe(I) to Fe(I)Fe(0) and then Fe(0)Fe(0) . Titration of HCl into the electrochemical cell resulted in an increase in the reductive current, which we attribute to proton reduction. This was accompanied by a positive shift in the onset potential from -2.04 V to -1.89 V vs SHE (reported as -1.40 V to -1.25 V vs $\text{Fc}^{+/0}$). This shift in onset potential suggested that $[\mathbf{1b-BCF}][\mu\text{-H}]^-$ is a catalytically relevant species. The current response continued to increase until 20 eq HCl were added. Comparison of FTIR Spectra of **1b-**

BCF][$\mu\text{-H}$] $^-$ at the start and end of the cyclic voltammetry experiments demonstrate that $[\mathbf{1b}\text{-BCF}][\mu\text{-H}]^-$ is still present and stable under electrocatalytic conditions, even in the presence of up to 100 mM HCl.

In order to search for possible intermediates of catalytic proton reduction, we tried to observe the reduction chemistry of $[\mathbf{1b}\text{-BCF}][\mu\text{-H}]^-$ spectroscopically. Chemical reduction of $[\mathbf{1b}\text{-BCF}][\mu\text{-H}]^-$ with CoCp^*_2 resulted in the reformation of $\mathbf{1b}\text{-BCF}^{2-}$, we observe a possible intermediate in the FTIR spectrum, which we probed further by another EPR trapping experiment. At -40°C , $[\mathbf{1b}\text{-BCF}][\mu\text{-H}]^-$ was mixed with CoCp^*_2 . The measured EPR spectrum displayed a mixture of signals which were elucidated by simulations to show a mixture of rhombic and axial signals in a 3:1 ratio, quantified through fitting using EasySpin (figure 5.5, panel B).^{160, 161} The rhombic signal displayed apparent g-values $g_1 = 2.039$, $g_2 = 2.015$ and $g_3 = 2.004$. The axial signal displayed g-values $g_{\parallel} = 2.027$ and $g_{\perp} = 2.033$. This is in agreement with the reported NMR spectra of $[\mathbf{1b}\text{-BCF}][\mu\text{-H}]^-$, which suggest that there were two major isomers of $[\mathbf{1b}\text{-BCF}][\mu\text{-H}]^-$ present in solution. We thus concluded that the species observed in the EPR Spectrum was the one electron reduced species $[\mathbf{1b}\text{-BCF}][\mu\text{-H}]^-$.

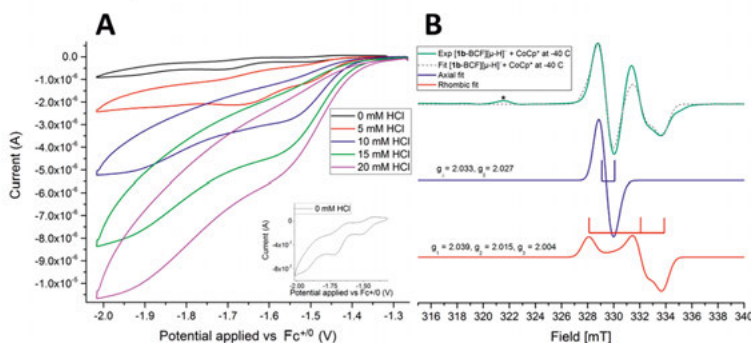
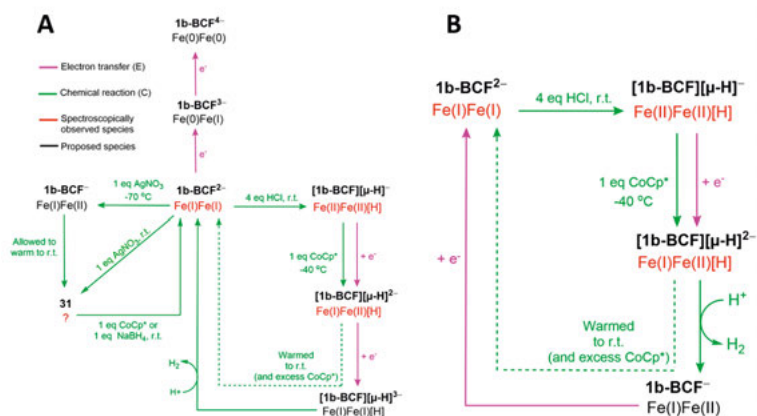


Figure 5.5. Reduction chemistry of $\mathbf{1b}\text{-BCF}^{2-}$ and $[\mathbf{1b}\text{-BCF}][\mu\text{-H}]^-$. **Panel A:** CVs of the reduction of $\mathbf{1b}\text{-BCF}^{2-}$ showing the change in reduction current and potential with addition of HCl. **Panel B:** EPR spectra showing the reduction of $[\mathbf{1b}\text{-BCF}][\mu\text{-H}]^{2-}$. Top: experimental spectrum shows a mixture of signals (green spectrum), supported by a simulated fit (grey dashed lines) demonstrates a mixture of axial signal (blue fit) and rhombic signal (red fit). Reproduced from reference 57 with permission from the Royal Society of Chemistry.

5.4 Conclusions and outlook

In paper III we showed that the binding of BCF to $\mathbf{1b}^{2-}$ generates an electrocatalyst for H_2 production. The change in Fe electron density following protonation of the Fe(I)Fe(I) complex to form the diferrous hydride was also probed by FTIR spectroscopy, and additionally X-ray spectroscopy. Through a combination of spectroscopy and cyclic voltammetry we investigated the oxidation and reduction chemistry of this compound and proposed that the

catalytic cycle includes Fe(I)Fe(I), Fe(I)Fe(II) and Fe(II)Fe(II) intermediates, scheme 5.2. These results for the dicyanide complex **1b**-BCF²⁻ illustrate the importance of hydrogen bonding to the cyanide ligands in the active-site pocket. Biologically relevant oxidation states are proposed in the suggested catalytic cycle(s), and even though bridging hydrides are present, this provides a strong biomimetic angle. Revisiting this complex highlights the possibility that Lewis acids could be used to tune the electron density on [FeFe]-H₂ase mimics, and maybe a capping borane could even be designed in such a way as to trap the rotated structure of the complex mimicking the [FeFe]-H₂ase co-factor within the active site pocket. This would increase the biomimetic relevance, promote terminal hydride formation and provide a very nice spectroscopic model.



Scheme 5.2. Possible catalytic cycles for **1b**-BCF²⁻. **Panel A:** Scheme summarising the observed redox and protonation chemistry of **1b**-BCF²⁻. The chemical reagents employed to trigger a specific reaction are shown in green, while an electrochemical redox process is indicated by “e⁻” and a pink arrow. **Panel B:** Alternative mechanism that was not ruled out by this study. Reproduced from reference 57 with permission from the Royal Society of Chemistry.

Chapter 6: Paper IV Metal exchange

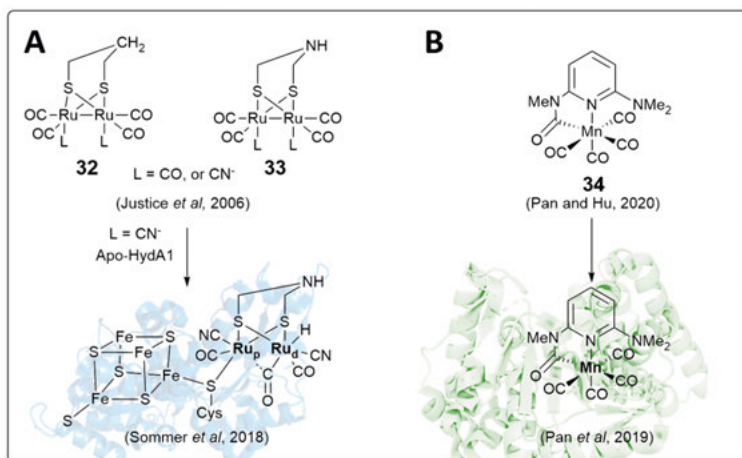
Introduction

Thus far I have looked at [FeFe]-H₂ase cofactor mimics from different angles; the bridgehead ligand; introduction of a redox active ligand ([Fe₄S₄]-cluster); and the effect of capping ligands on the terminal cyanides. All of these aspects provide exciting design pathways towards diverse [FeFe]-H₂ase cofactor mimics. Over 1000 [FeFe]-H₂ase cofactor mimics have been reported in the Cambridge crystallographic data centre, however, a very important aspect of the H-cluster that is yet to be explored to such a great extent is the replacement of iron with non-native metals while retaining the ligand coordination sphere in the [FeFe]-H₂ase cofactor mimics (from here on referred to as metal-exchange mimics). This is an exciting synthetic challenge, and it is becoming of greater interest in the hydrogenase field.

A landmark example of a metal-exchange mimic is the ruthenium based mimic ([RuRu] cofactor). The [RuRu] cofactor with the carbon bridgehead (**32**, scheme 6.1, panel A) was first synthesised in 2006 by Justice *et al.*,¹⁶² they demonstrated that electrochemical production of hydrogen using this complex is very unfavourable due to its very negative reduction potential of -1.99 V vs SHE (reported as -1.80 V vs Ag|AgCl). Nevertheless, the story moved further several steps in 2018, when Sommer *et al.*¹⁶³ reported the synthesis of a [RuRu] cofactor with a nitrogen bridgehead (**33**, scheme 6.1, panel A) and inserted the dicyanide derivative into the apo-HydA1 from *Chlamydomonas reinhardtii* (scheme 6.1, panel A). In my opinion this result is remarkable because it confirms that artificial maturation of apo-[FeFe]-H₂ases can be applied using a complex in which the ligands of the [FeFe]-H₂ase cofactor mimic are left intact but the metal is changed to a non-native metal. Despite this result, the semi-synthetic [RuRu]-H₂ase is not capable of proton reduction. This is because of the aforementioned unfavourable reduction potential. However, Sommer *et al.* were able to use the [RuRu]-H₂ase to trap the terminal hydride state.

A second example where complexes based on non-native metals have been shown to artificially mature an enzyme is in the case of the [Fe]-H₂ase (figure 1.1 panel B). Xile Hu and Seigo Shima have, in collaboration, synthesised a manganese based mimic of the [Fe]-H₂ase cofactor and inserted it into an apo-[Fe]-H₂ase to make a [Mn]-H₂ase (scheme 6.1, panel B).^{164, 165} Extraordinarily, they were able to show that the [Mn]-H₂ase demonstrated enhanced

activity over an analogous semi-synthetic [Fe]-H₂ase. These results demonstrated that catalytic functionality of a manganese based active site in a hydrogenase is viable. And if it is possible to make a [RuRu]-H₂ase and a [Mn]-H₂ase, then why not a [MnMn]-H₂ase? And would such a hydrogenase be functional?



Scheme 6.1. Artificial maturation of hydrogenases using non-native metals. **Panel A:** Metal-exchange complexes **32** and **33**, ruthenium based [FeFe]-H₂ase cofactor mimics and their insertion into apo-HydA1; **Panel B:** Manganese based [Fe]-H₂ase metal-exchange mimic (**34**) and insertion into apo-Hmd.

In addition to the synthetic challenge and the potential novel reactivity that may be found when investigating the metal-exchange mimics, there is also a biological perspective that may be gained from investigations of manganese based [FeFe]-H₂ase cofactor mimics. There are multiple enzymes in nature in which both manganese and iron are able to perform the same chemical transformations. Examples of this are superoxide dismutase, and catalase.¹⁶⁶

Superoxide dismutase is an enzyme that converts superoxide to molecular oxygen and hydrogen peroxide, protecting cells from oxidative damage. There are metal specific superoxide dismutases or cambialistic superoxide dismutases which can function either with Mn or Fe.^{166, 167}

Catalases catalyse the decomposition of hydrogen peroxide to oxygen and water. They exist as iron based heme proteins and also as non-heme manganese catalases that contain a binuclear manganese centre.¹⁶⁸

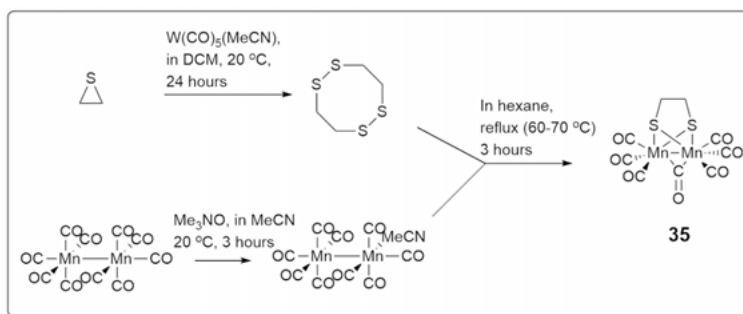
The aims of this project were to:

- Synthesise a dimanganese dithiolato carbonyl complex (referred to as [MnMn] when not discussing a specific complex).
- Investigate its substitution chemistry.
- Investigate the redox chemistry of the [MnMn] complexes, and probe for proton reduction activity.

6.1 Synthesis of a manganese metal-exchange [FeFe]-H₂ase cofactor mimic

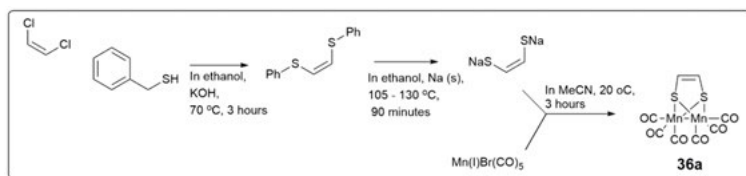
There were several possible routes to the [MnMn] metal-exchange mimic that I could have taken. At the start of the project, there were two clear routes to follow to make a dimanganese dithiolato carbonyl complex. The first option, summarised in scheme 6.2, was to synthesise 1,2,5,6-tetrathiacyclooctane and react that with $\text{Mn}_2(\text{CO})_9(\text{MeCN})$ to form $\text{Mn}_2(\mu\text{-edt})(\mu\text{-CO})(\text{CO})_6$.^{169, 170} After attempting to make the required sulphur containing macrocycle from thiirane and a tungsten carbonyl catalyst,^{171, 172} it was evident that this route could not be pursued and fully investigated within the timescale of the PhD, so I decided to pursue a second route to a [MnMn] complex.

The second synthesis option was more successful, and is summarised in scheme 6.3. Starting from cis-dichloroethene, benzylmercaptan substituted chlorine for a thiobenzyl group to form cis-bis(benzylthio)ethene. This was then reacted with sodium to form a white fluffy powder, disodium bis(thiolato)ethene.¹⁷³ Disodium bis(thiolato)ethene was then mixed with manganese(I)pentacarbonyl bromide, the reaction mixture changed from a yellow-orange suspension to a bright red suspension. Following a silica column with pentane eluent, $\text{Mn}_2(\mu\text{-S}_2\text{C}_2\text{H}_2)(\text{CO})_6$ could be isolated in 7 % yield.¹⁷⁴ One side product was identified as the bright yellow $\text{Mn}_2(\text{CO})_{10}$. All of these transformations were carried out under anaerobic conditions on the Schlenk line.



Scheme 6.2. Synthetic route to complex **35** from Adams and co-workers. A tungsten carbonyl catalyst converted thiirane to 1,2,4,6-tetrathiacyclooctane, and $\text{Mn}_2(\text{CO})_{10}$ was activated by substituting a carbonyl ligand with acetonitrile. The two products were then reacted with each other to form the dimanganese pentacarbonyl complex with the -edt- bridging ligand, that contains a bridging carbonyl ligand.^{169, 171, 172}

The FTIR was recorded in dichloromethane and showed to match that reported already, with carbonyl bands at 2056 cm^{-1} , 2021 cm^{-1} , 1972 cm^{-1} , 1943 cm^{-1} , see figure 6.1.¹⁷⁴ I was also able to isolate crystals, which were analysed by X-ray crystallography and we were able to confirm the structure which was first proposed in 1963 and matches the crystal structure of a similar compound, $\text{Mn}_2(\mu\text{-S}_2\text{C}_2\text{Ph}_2)(\text{CO})_6$, reported by Lindner *et al*, figure 6.2.¹⁷⁵



Scheme 6.3. Synthetic route to **36a** from King and Eggers. Starting from cis-dichloroethylene, the bridging ligand was synthesised in two steps. First benzylmercaptan substituted the chlorine atom in cis-dichloroethylene for a thiophenol group to make cis-bis(benzylthio)ethylene. This ligand was then reacted with Mn(I)Br(CO)_5 over 3 hours to form the target complex $[\text{Mn}_2(\mu\text{-S}_2\text{C}_2\text{H}_2)(\text{CO})_6]$ ^{173, 174, 176}

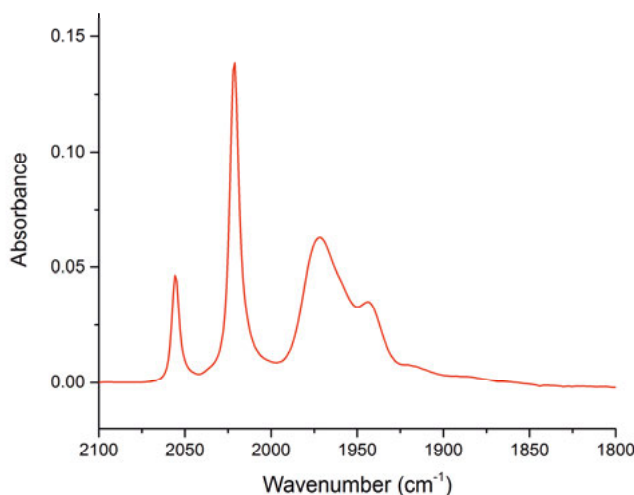


Figure 6.1. FTIR of 1mM **36a** in dichloromethane, with peaks at 2056 cm^{-1} , 2021 cm^{-1} , 1972 cm^{-1} , 1943 cm^{-1} .

The crystal structure, which has also been predicted based on DFT calculations by Radu *et al.*¹⁷⁷ shows a Mn1-Mn2 bond of 2.7802(5) Å. Interestingly, the alkene bond coordinates to one of the manganese ions (Mn2), and this creates asymmetry in the complex. The Mn2-C1/C2 distance to the alkene is 2.144(1) Å and 2.151(1) Å respectively, while the Mn1-C1/C2 distance is 3.209(1) Å and 3.213(1) Å respectively. In the crystal structure the complex appears to adopt a rotated structure in which the basal carbonyl ligand of Mn2 is approaching a bridging position. Figure 6.2, panel C highlights this and also shows the staggered conformation of the carbonyl ligands. Additionally, the complex, when viewed from the side, appears to be a pianostool type complex, figure 6.1, panel B. Based on the ligand sphere observed in the crystal structure, I was able to assign the d-electron configuration as d^5 for Mn01 and d^7 for Mn02. This makes complex **36a** an overall spin $S=0$ system because the

unpaired electron on each manganese antiferromagnetically couple to one another. And this is confirmed by the silent EPR spectrum of the complex (figure 6.9).

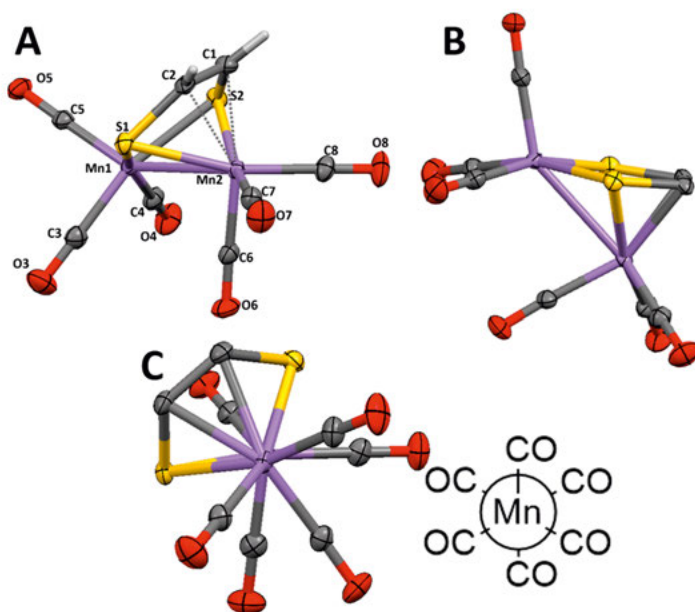
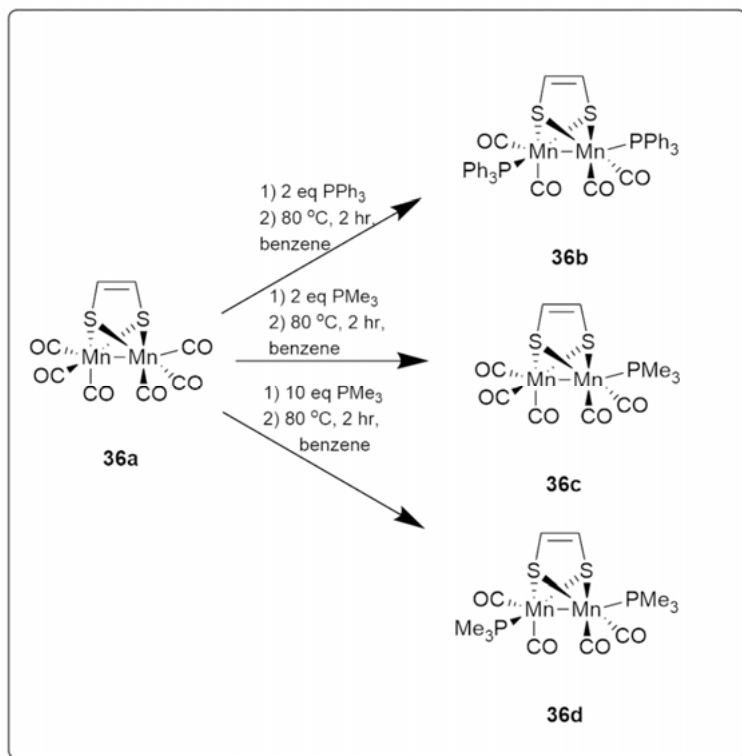


Figure 6.2. Crystal structure of **36a** viewed from 3 different angles. The crystal structure has been reported in the Cambridge crystallographic data centre under deposition number: 2162569. **Panel A:** Front on view illustrates the asymmetry induced by the coordination of the alkene to Mn2. **Panel B:** viewed from an angle to illustrate the piano-stool structure. **Panel C:** Side on view shows the staggered arrangement of the carbonyl ligands along the Mn-Mn bond, further illustrated by the Newman diagram.

6.2 Ligand substitution chemistry of **36a**

[FeFe]-H₂ase cofactor mimics are able to undergo ligand substitution reactions as in the synthesis of **1b**²⁻ or **2b**²⁻. One of the goals of this project is to find out if a dimanganese complex could be inserted into an apo-hydrogenase to make a semi-synthetic [MnMn]-H₂ase. For this, cyanide ligands are needed for two reasons. The first reason is to create the most biomimetic complex possible, as discussed throughout this thesis, cyanide ligands on the [FeFe]-H₂ase cofactor enable hydrogen bonding of the cofactor to the protein backbone within the active site pocket. The second reason is that the complex should be water soluble in order to be compatible with the artificial maturation process.^{51, 151} However, the carbonyl ligands are also often substituted for phosphine ligands, as in compounds **7-10** in scheme 1.2. Phosphine ligands, like cyanide ligands are strong σ -donors, and coordination to the iron centres produces an electron rich metal that is difficult to reduce, but often more prone

to protonation. It has even been argued that cyanides are nature's trimethylphosphane.⁷⁵ For these reasons I wanted to probe the substitution chemistry of the complex **36a**, starting with phosphine substitutions, which I have summarised in scheme 6.4.



Scheme 6.4. Summary of the phosphine substitution reactions investigated for **36a**.

The disubstituted triphenylphosphine complex **36b** had already been reported by King and Eggers.¹⁷⁴ The synthesis was replicated and the product was initially characterised by FTIR. **36b** showed carbonyl bands at 1963 cm^{-1} , 1927 cm^{-1} , 1899 cm^{-1} , 1872 cm^{-1} which matched the reported FTIR data, figure 6.3. **36b** could be purified on a silica column, elemental analysis confirmed the expected ratios of CHNS, and ^{31}P -NMR spectroscopy confirmed the presence of phosphine ligands in the complex.

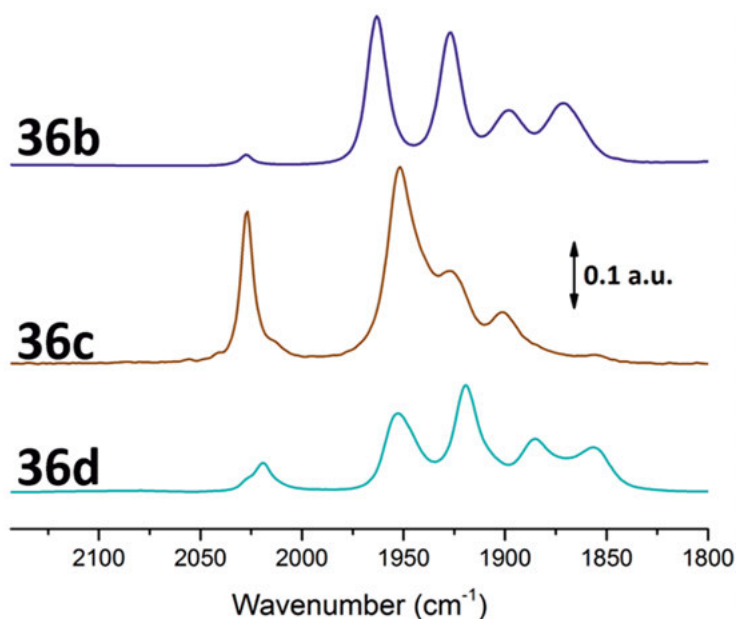


Figure 6.3. FTIR spectra of complexes 5 mM **36b** (blue spectrum), 5 mM **36c** (brown spectrum) and 5 mM **36d** (cyan spectrum) in dichloromethane.

^{31}P -NMR spectra recorded at 0 °C showed two singlets 1:1 ratio. $\delta_{s1} = 96.27$, $\delta_{s2} = 79.05$. At -90 °C the singlet at resolved to four singlets at $\delta_{s1}^{-90} = 96.06$ ppm, $\delta_{s2}^{-90} = 83.77$ ppm, $\delta_{s3}^{-90} = 80.43$ ppm, $\delta_{s4}^{-90} = 77.55$ ppm. These variable temperature NMR experiments demonstrate that multiple isomers **36b** are possible. ^{31}P -NMR studies on [FeFe]-H₂ase mimics have also demonstrated this fluxional behaviour of the phosphine ligands in solution.¹⁷⁸⁻¹⁸⁰

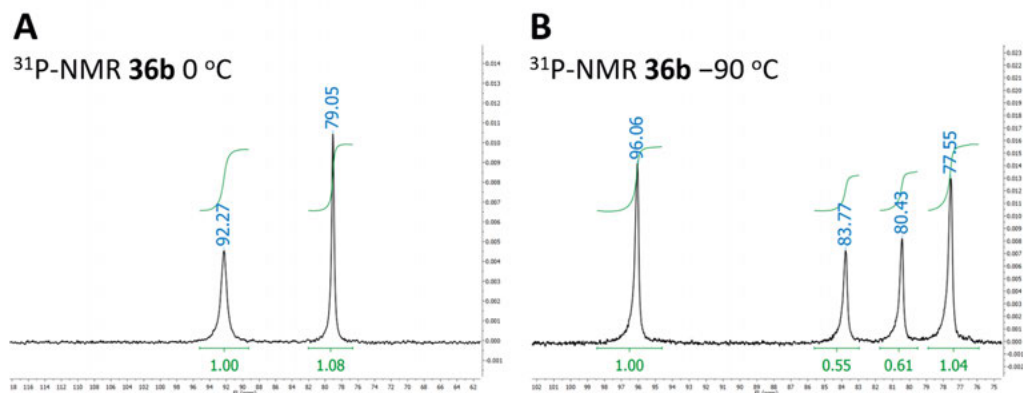


Figure 6.4. Variable temperature ^{31}P -NMR experiments of **36b**. **Panel A:** ^{31}P -NMR of **36b** recorded at 0 °C. **Panel B:** ^{31}P -NMR -90 °C. Showing how the singlets at $\delta_{\text{P}} = 96.27$, $\delta_{\text{P}} = 79.05$ resolves at -90 °C to reveal four new singlets at $\delta_{\text{P}} = 96.06$ ppm, $\delta_{\text{P}} = 83.77$ ppm, $\delta_{\text{P}} = 80.43$ ppm, $\delta_{\text{P}} = 77.55$ ppm.

Each isomer results in a different phosphorous environment, which is visible in the NMR. From the currently presented experiments we can only say that at least four phosphine environments are visible in the ^{31}P -NMR spectra of **36b**; however, to probe this, further NMR experiments may be carried out. Two such experiments are spin echo to observe the dynamics of phosphorous exchange and 2D HMBC experiment to observe precisely which ^{31}P signals belong to the same molecule. These experiments will help in assigning which signal arises from which isomer of **36b**.

Two mole equivalents of trimethylphosphine were added to a solution of **36a** in benzene and the reaction was heated to 80 °C. This resulted in the synthesis of the mono-phosphine of **36c**. The reported reaction procedure was actually an attempt to form **36d**, however I did not take into account the boiling point of trimethylphosphine in the first experiments. It is likely that much of the trimethylphosphine actually evaporated which meant that there was a limited amount of trimethylphosphine in the reaction mixture and, happily, **36c** formed instead. **36c** was purified by silica column with DCM:pentane eluent. Two bands eluted, the first band was **36c** and the second band was unreacted **36a**. Unfortunately, at the time of writing, not enough **36c** has been isolated for a full characterisation, however the FTIR spectrum has been measured, figure 6.3, and upon comparing with a [FeFe]-H₂ase cofactor mimic that is monosubstituted with cyanide,¹⁸¹ I found that the carbonyl band pattern matches. This has led to an initial and very tentative assignment as the mono-phosphine **36c**. However, additional data, including a crystal structure, is critical to fully identify this compound.

Moving on to the intended product, the disubstituted trimethylphosphine complex **36d**. The hexacarbonyl complex **36a** was treated with 10 eq trimethyl

phosphine in benzene at 80 °C. **36d** could be purified by silica plug with pentane eluent, and the product was isolated as a dark brown powder after removal of the solvent. The FTIR spectrum obtained was shifted to slightly lower wavenumbers relative to **36b**, and the carbonyl vibrational band pattern is very similar, indicating a similarly symmetric compound with slightly higher electron density on the manganese centres, figure 6.3. CHNS elemental analysis supports our assignment of **36d**. Variable temperature ^{31}P -NMR experiments were carried out analogously to those carried out for **36b**, figure 6.5. In this case the ^{31}P -NMR spectrum recorded at 0 °C shows one broad peak at $\delta_{\text{s1}} = 40.45$ ppm, with a small shoulder at $\delta_{\text{sh}} \sim 37.93$ ppm, this confirms the presence of phosphorous in **36d**. Upon cooling to -90 °C the singlet at $\delta_{\text{s1}} = 40.45$ ppm resolved into a much more complicated spectrum, indicative of a more complicated mixture of isomers of the complex. The new ^{31}P -NMR spectrum displayed seven singlets, $\delta_{\text{s1}}^{-90} = 57.95$ ppm, $\delta_{\text{s2}}^{-90} = 44.38$ ppm, $\delta_{\text{s3}}^{-90} = 42.00$ ppm, $\delta_{\text{s4}}^{-90} = 40.11$ ppm, $\delta_{\text{s5}}^{-90} = 39.50$ ppm, $\delta_{\text{s6}}^{-90} = 36.42$ ppm, $\delta_{\text{s7}}^{-90} = 33.30$ ppm. The singlets at $\delta_{\text{s4}}^{-90} = 40.11$ ppm, $\delta_{\text{s5}}^{-90} = 39.50$ ppm appear to resolve from the shoulder ($\delta_{\text{sh}} \sim 37.93$ ppm) in the 0 °C measurement, and are thus unassigned and marked with an asterisk (*). This more complicated ^{31}P -NMR spectrum reflects the higher possibility of isomers relative to **36b** because trimethylphosphine complexes are less sterically hindered than triphenylphosphine. 2D HMBC ^{31}P -NMR would be particularly helpful here to establish which peaks belong to each isomer.

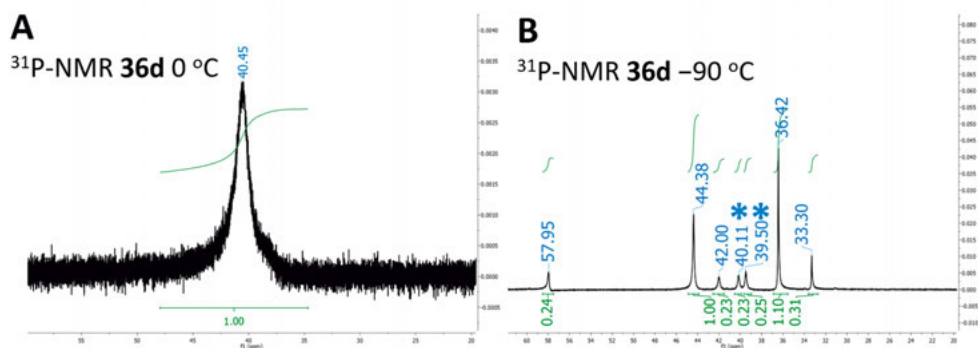


Figure 6.5. Variable temperature ^{31}P -NMR experiments of **36d**. **Panel A:** ^{31}P -NMR of **36d** measured at 0 °C, showing one broad peak at $\delta_{\text{s1}} = 40.45$ ppm, with a small shoulder at $\delta_{\text{sh}} \sim 37.93$ ppm. **Panel B:** ^{31}P -NMR of **36d** measured at -90 °C showing 7 singlets, $\delta_{\text{s1}}^{-90} = 57.95$ ppm, $\delta_{\text{s2}}^{-90} = 44.38$ ppm, $\delta_{\text{s3}}^{-90} = 42.00$ ppm, $\delta_{\text{s4}}^{-90} = 40.11$ ppm, $\delta_{\text{s5}}^{-90} = 39.50$ ppm, $\delta_{\text{s6}}^{-90} = 36.42$ ppm, $\delta_{\text{s7}}^{-90} = 33.30$ ppm. Unassigned peaks are indicated with an asterisk.

Thus far, crystallisation attempts of **36b-d** have been unsuccessful, however more attempts are underway. Further ^{31}P -NMR studies are necessary for optimal solution characterisation. The presence of manganese as the metal centre

of these complexes creates some challenges for NMR characterisation of these compounds using conventional nuclei (^1H and ^{13}C).¹¹² The heavy metal centre shortens the spin-spin relaxation time, making the signal observed in the NMR spectrum weaker and/or broader, which means that more scans are required to detect the signal, and that any coupling constants are difficult to resolve. One reason for fast relaxation is the presence of heavy $I \geq \frac{1}{2}$ nuclei, and this is also known for iron ($I = 1/2$) based carbonyl complexes. The problem is exacerbated by the quadrupole moment caused by the nuclear spin ($I = 5/2$) of the manganese centre, this results in faster relaxation and thus broadening of the observed NMR signal. For the already spin dilute ^{13}C -NMR, this means that well over 10s of thousands of scans are required to observe the signals attributable to the carbon atoms coordinated directly to the metal centre. This broadening of the NMR spectrum is also observed in ^1H -NMR, while proton signals are still observed, the signals appear very broad and any coupling cannot be resolved. Additionally, the broadening is also observed in ^{31}P -NMR, however, the range observed in ^{31}P -NMR is much larger than that of ^1H -NMR, 100s of ppm for ^{31}P -NMR compared to 10s of ppm for ^1H -NMR, so in the case of ^{31}P -NMR coupling constants can be more readily resolved.

6.3 Electrochemistry of **36a**

In parallel to the characterisation of compounds **36a-d**, I also characterised them electrochemically and investigated them for proton reduction activity.

Cyclic voltammetry of **36a** in DCM showed a reduction current with onset potential -2.09 V vs SHE (reported as -1.41 V vs $\text{Fc}^{+/0}$), and peak cathodic potential at $E_{p,c} = -2.28$ V vs SHE (reported as -1.603 V vs $\text{Fc}^{+/0}$), figure 6.6, panel A. The reduction potential of **36a** is slightly less negative than that of **1a** suggesting that **36a** may accept electrons more easily than its Fe-based counterpart. Observing the dependence of $i_{p,c}$ of **36a** on square route of scan rate demonstrated that the reduction is diffusion controlled which suggests that the reduced species is in solution, rather than a residue on the electrode. Addition of 1 eq TFA to **36a** results in an increase in current in line with proton reduction activity. In addition to this, the partial oxidation peak at -1.81 V vs SHE (reported as -1.12 V vs $\text{Fc}^{+/0}$) disappears, indicating that the partial reduction products of **36a** are not present on the return scan, figure 6.6, panel B. After the addition of 5 eq of TFA, the onset potential shifted by approximately 80 mV to milder potentials, -2.01 V vs SHE (reported as -1.33 V vs $\text{Fc}^{+/0}$). Control experiments comparing the FTIR of **36a** at the start of the titration and after the addition of 50 eq TFA show that the complex does not protonate under acidic conditions. These data together can provide some insight into the proton reduction, the current and onset potential response, along with the unchanged FTIR after the addition of TFA suggest that the initial steps of proton reduction occur via an EC-type mechanism. That is a reduction, followed by

a chemical step (protonation). This could be confirmed by FTIR spectroelectrochemical studies.

After addition of higher equivalents of TFA, the cyclic voltamogram adopted a new trace shape, and the catalytic current did not increase anymore. This result could be caused by two things; 1) decomposition of **36a** under highly acidic and reducing conditions; or 2) the electrochemical system has entered a regime that is independent of proton concentration, i.e. the proton concentration is no longer the limiting factor in catalysis. The control experiments comparing the FTIR of **36a** at the start of the titration and after the addition of 50 eq TFA show that the complex does not protonate under acidic conditions, which supports the second hypothesis. It should be noted that current is passed when TFA is added to a blank electrochemical cell. Still, the observed current at -1.6 V vs $\text{Fc}^{+/0}$ in the blank cell containing 25 mM TFA is only 6 % of that observed at the same potential in the cell containing 5 mM **36a** and 25 mM TFA. We are thus confident that **36a** is active for proton reduction.

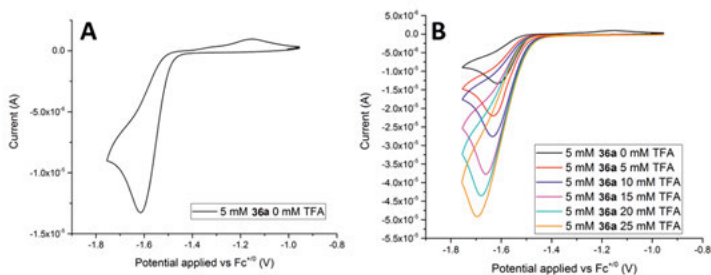


Figure 6.6. Panel A: cyclic voltamogram of 5 mM **36a** measured at 0.1 V s^{-1} in dichloromethane with 0.1 M TBAPF₆. Panel B: cyclic voltammograms of 5 mM **36a** and 0–25 mM TFA in an acid titration measured at 0.1 V s^{-1} in dichloromethane with 0.1 M TBAPF₆.

6.4 Electrochemistry of **36b-d**

The electrochemistry of **36b**, **36c** and **36d** was also investigated, figure 6.7, Panel A. As suggested above, the phosphine ligands push electron density onto the metal centres, making reduction less favourable. Indeed, the reduction of complexes **36b-d** occurred at much more negative potentials than **36a**. **36b** reduces at the most negative potential of the series of compounds -2.83 V vs SHE (reported as -2.15 V vs $\text{Fc}^{+/0}$), figure 6.7 Panel B. **36c** has a reduction potential at -2.77 V vs SHE (reported as -2.09 V vs $\text{Fc}^{+/0}$), figure 6.7 Panel C, and **36d** -2.61 V vs SHE (reported as -1.93 V vs $\text{Fc}^{+/0}$), figure 6.7 Panel D, more positive than **36c**, albeit with much lower currents. The lower currents observed upon reduction of **36c** and **36d** suggest that they are not fully reduced within the potential window, and the true reductive event may

be hiding beyond the scan window. Nevertheless, the reducing currents beyond -2.91 V vs SHE (-2.23 V vs $\text{Fc}^{+/0}$) were not explored due to the risk of interference from increasing background currents. Addition of 1 eq TFA to a solution of **36b** (figure 6.7 panel D) resulted in small current enhancement, however upon addition of a 2nd equivalent the CV trace changed shape and showed some curve crossing, indicative of a slightly more active species on part of the return scan (possibly through degradation of **36b** to form a film on the electrode, although this has not been proven here). An FTIR spectrum after the addition of TFA indicated no change in the carbonyl bands of **36b**. Similar acid titration experiments were carried out using **36c** and **36d** (figure 6.7, panel C and panel D respectively). Neither of these experiments showed clear support for proton reduction catalysis. Additionally the FTIR spectra of **36c** and **36b** after the addition of TFA demonstrated no change in the carbonyl bands indicative of no protonation of the complexes. It is surprising that none of the phosphine substituted complexes, **36 b-d**, could be protonated by TFA.

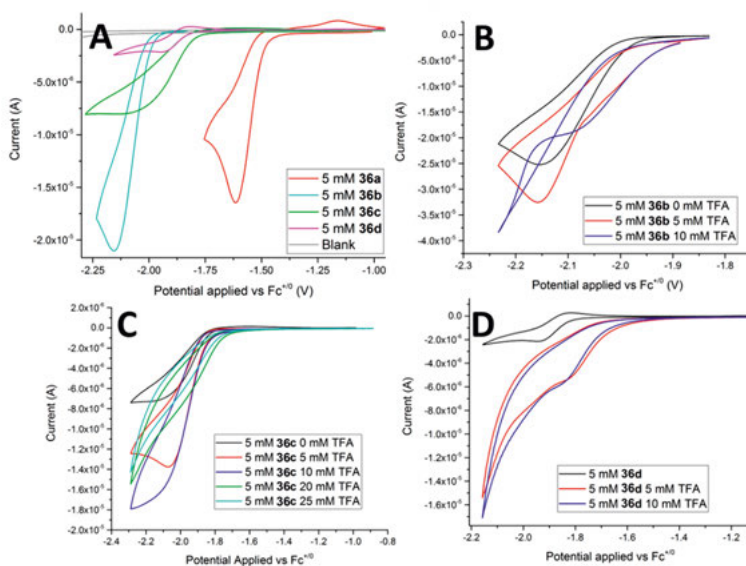


Figure 6.7. Cyclic voltammetry responses and catalytic assays of **36a-d**. **Panel A:** CVs of 5 mM **36a** (red trace), 5 mM **36b** (cyan trace), 5 mM **36c** (green trace) and 5 mM **36d** (magenta trace) measured at 0.1 V s^{-1} in dichloromethane with 0.1 M TBAPF₆. **Panel B:** CVs of 5 mM **36b** and 0-10 mM TFA) measured at 0.1 V s^{-1} in dichloromethane with 0.1 M TBAPF₆. **Panel C:** CVs of 5 mM **36c** and 0-25 mM TFA) measured at 0.1 V s^{-1} in dichloromethane with 0.1 M TBAPF₆. **Panel D:** CVs of 5 mM **36d** and 0-10 mM TFA) measured at 0.1 V s^{-1} in dichloromethane with 0.1 M TBAPF₆.

6.5 Chemical reduction of **36a-d**

Chemical reduction of **36a-d** was investigated and monitored spectroscopically by FTIR. CoCp*₂ was chosen as it is a relatively strong reductant, -2.58 V vs SHE (reported as -1.94 V vs Fc^{+/0}). Despite the very negative reduction potential of CoCp*₂, many mole equivalents were needed in order to observe a change in the FTIR spectra of **36a-d**.

For the reduction of **36a**, at least 20 mole equivalents of CoCp*₂ were needed relative to **36a**, figure 6.8, Panel A. This resulted in a spectrum that was a mixture of **36a** and other species. Spectral subtraction resulted in a spectrum that suggest a possible mixture of two products. Figure 6.8, Panel B shows carbonyl bands at 2031 cm^{-1} , 2005 cm^{-1} and 1984 cm^{-1} and broader carbonyl bands at 1952 cm^{-1} , 1920 cm^{-1} and 1984 cm^{-1} . The two species have not been structurally assigned at the time of writing, however, based on the shift to lower wavenumbers as compared to **36a**, we attribute the carbonyl bands to one or more reduction products. The EPR spectrum observed for samples of **36a** treated with CoCp*₂ supports the idea that a one electron reduction occurred to produce a paramagnetic Mn(0) species (figure 6.9).

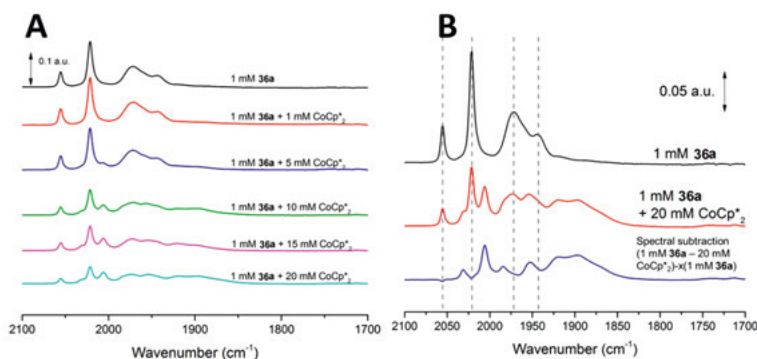


Figure 6.8. Chemical reduction of **36a** monitored by FTIR. Panel A: FTIR spectra measured during titration of CoCp*₂ into **36a**. Panel B: comparison of 1 mM **36a** (black spectrum) with 1 mM **36a** and 20 mM CoCp*₂ (red spectrum) and the result of spectral subtraction (blue line).

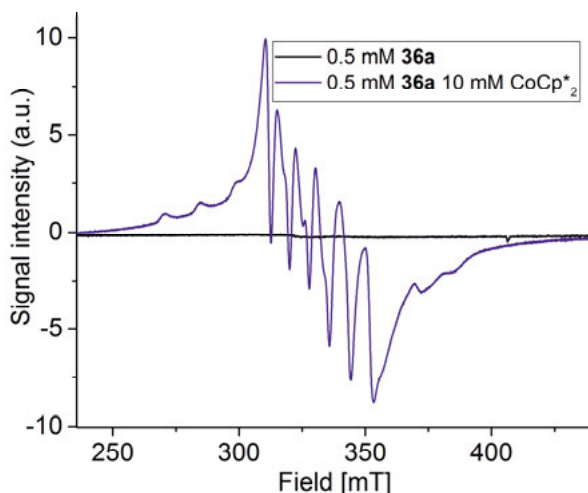


Figure 6.9. EPR spectra of 0.5 mM **36a** (black spectrum) demonstrates that the two manganese ions are antiferromagnetically coupled, and the EPR spectrum of 0.5 mM **36a** and 10 mM CoCp*₂ (blue spectrum) the six-line spectrum in the $g = 2$ region indicates the presence of a paramagnetic manganese species. The species was formed under reducing conditions, and we therefore tentatively assign it as a Manganese (0) species.

The titration experiments were repeated for compounds **36b-d**. As expected due to their much more negative reduction potential relative to **36a**, high equivalents of CoCp*₂ were needed to see changes in the FTIR spectra. For example, **36b** required 50 mole equivalents of CoCp*₂ relative to **36b**, figure 6.10, panel A. The resulting FTIR spectrum shows a mixture of **36b** and another product at lower wavenumbers, suggestive of successful reduction by CoCp*₂. Spectral subtraction was done to elucidate the new peaks at 1908 cm⁻¹, 1891 cm⁻¹, 1869 cm⁻¹, 1824 cm⁻¹, and 1805 cm⁻¹. These peaks reflect the presence of one or more reduced products. **36d** was not reduced even in the presence of 50 mole equivalents of CoCp*₂, figure 6.10 panel B.

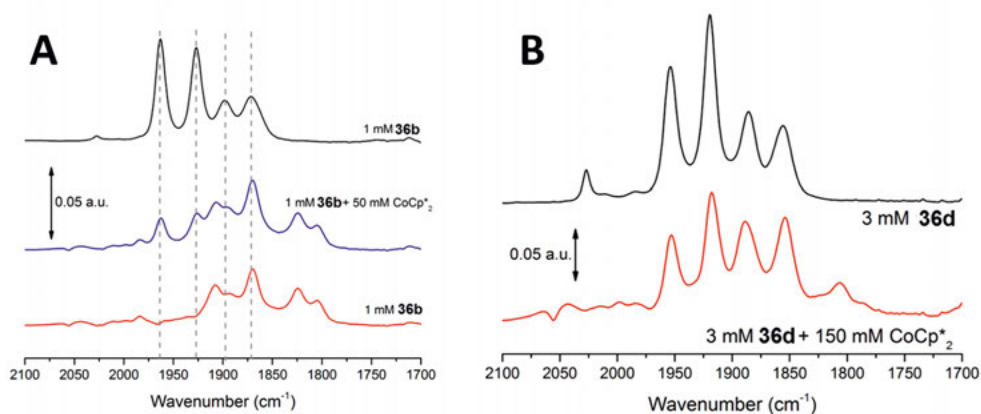


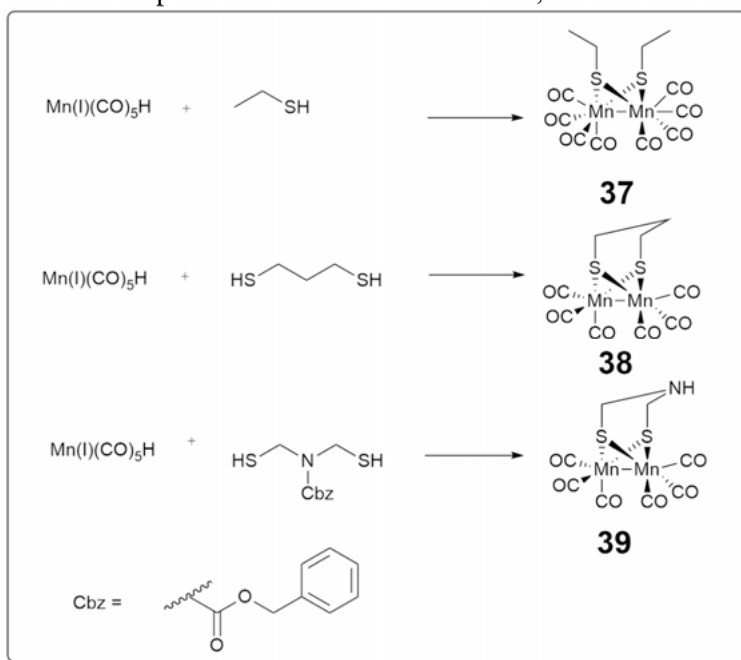
Figure 6.10. Chemical reduction of **36b** and **36d** **Panel A:** FTIR spectra comparing 1 mM **36b** (black spectrum) and 1 mM **36b** and 50 mM CoCp*₂ (blue spectrum) and the result of spectral subtraction (red line). **Panel B:** FTIR spectra comparing 3 mM **36d** (black spectrum) and 3 mM **36d** and 150 mM CoCp*₂ (red spectrum).

6.6 Conclusions and outlook

This work has shown that this family of Mn complexes can provide a path towards Mn based analogues of the [FeFe]-H₂ase cofactor. I have revisited two complexes previously reported (**36a** and **36b**) and have studied them in the context of proton reduction. I have synthesised two new compounds (**36c** and **36d**) and investigated these for proton reduction as well. The crystal structure of **36a** is confirmed, and we observe a rotated structure of the CO-ligands and coordination of the alkene ligand to one of the manganese ions to create a very unsymmetric complex. The diphosphine compounds were synthesised in high enough yields to carry out variable temperature ³¹P-NMR experiments which confirmed the presence of phosphorous and demonstrated the fluxional behaviour of the phosphine ligands which is also observed for analogous [FeFe]-H₂ase cofactor mimics. Still, I recognise that more characterisation of complexes **36b-d** especially should be carried out to confirm their structures. The available substitution reactions for these complexes indicate that cyanides may be able to substitute carbonyl ligands to make water soluble [MnMn]-cofactor complexes that can be used for artificial maturation (appendix 2). The [MnMn]-cofactors were investigated electrochemically and tested for proton reduction. **36a** is a modest proton reduction catalyst. As expected **36b-d** exhibit significantly more negative reduction potentials as compared to **36a**. However, in contrast to what is often observed for related phosphine substitute iron complexes, they did not appear to readily protonate. Moreover, the phosphine substituted complexes did not show any definite response for catalytic

proton reduction under my tested conditions. Chemical reduction experiments similar to those discussed in chapter 3 were carried out. These efforts showed that reduction does yield new products. However, the exact nature of these products remains to be elucidated, and especially in the case of **36a** further characterization could provide critical insight into the catalytic mechanism.

The project demonstrates that [MnMn] complexes may be viable mimics for [FeFe]-H₂ases because **36a** is able to reduce protons, albeit at rather negative reduction potentials, and at limited concentrations of TFA. Nevertheless this demonstrates that [MnMn] complexes are an interesting route to follow to make a [MnMn] cofactor for artificial maturation of apo-[FeFe]-H₂ases. Future synthesis routes will include formation of closer structural mimics [Mn₂(μ-pdt)(CO)₆] (**38**) and [Mn₂(μ-adt)(CO)₆] (**39**) and their substituted derivatives. I propose a potential synthetic route to these complexes in scheme 6.5. Adapting Treichel's procedure from 1963, which makes [Mn₂(μ-SC₂H₅)₂(CO)₆](**37**), under strict anaerobic conditions manganese(I) pentacarbonyl hydride and 1,3-propanedithiol should be distilled in to a Schlenk bulb which has been cooled in liquid nitrogen. The mixture should then be allowed to warm to room temperature and stirred for 12 hours, scheme 6.5.¹⁸²



Scheme 6.5. Proposed synthetic routes to complexes **37**, **38** and **39**.

Chapter 7: Concluding remarks

It is clear that a sustainable source of energy is needed to meet global demands and to soften the effects of climate change. A large proportion of this renewable energy will come from hydrogen, and [FeFe]-H₂ases are an important part of that. The H-cluster is the site of catalysis within the enzyme, and this has been shown to have very complex chemistry. Understanding this chemistry inspires molecular design of new catalysts, and over 1000 diironedithiolato complexes have been deposited in the Cambridge crystallographic data centre. Some of these structures have been discussed in the introduction to this thesis.

In this thesis I have examined various aspects of the H-cluster. Investigating how molecular design of H-cluster mimics may aid our understanding of the hydrogenase enzyme, or hydrogen production in general.

Paper I closely investigates the importance of the second coordination sphere (the bridgehead) on the oxygen tolerance of two structural mimics of the [FeFe]-H₂ase cofactor. I compared the reactivity of the two mimics with oxygen and ROS under neutral, reducing and acidic conditions. The results of the study support the hypothesis that the amine group in the bridging ligand plays a vital role in protecting both [FeFe]-H₂ase mimics and the [FeFe]-H₂ase cofactor in the native enzyme from decomposition by oxygen attack.

The role of the redox active ligand was addressed in paper II. The [Fe₄S₄]-cluster is an important aspect of the [FeFe]-H₂ase active site that is not present in most mimics due to the synthetic challenge accompanying the synthesis of artificial [Fe₄S₄]-clusters. Using a 16 amino acid oligopeptide, we were able to reproduce the chemistry of artificial maturation to make a miniaturised hydrogenase. The as-prepared miniaturised hydrogenase was in a H_{ox}-like state, highlighting the importance of the redox active ligand in the formation of the bridging carbonyl structure. The miniaturised hydrogenase demonstrated modest proton reduction activity. This study opened up new design pathways for novel H-cluster mimics by introducing possible modifications to the [Fe₄S₄]-cluster or introducing mutations to the oligopeptide.

Tuning the electron density of the Fe centres through modifications to the second/outer coordination sphere was further explored in paper III. Capping the cyanide ligands of a structural [FeFe]-H₂ase mimic enabled proton reduction catalysis at biologically relevant formal oxidation states. The borane based Lewis acids counteracted the sigma donating effect of the cyanide ligands by drawing electron density away from the iron centres, which allowed

for reduction at milder potentials than the parent complex. Furthermore the capping of the cyanide ligands with the Lewis acids likely mimicked the hydrogen bonding of the [FeFe]-H₂ase cofactor to the protein backbone of the active site pocket. This protection by the Lewis acid allowed for proton reduction catalysis, which was previously not possible in the dicyanide parent complex due to decomposition caused by proton attack at the cyanide ligands. Borane capping ligands allowed for the study of proton reduction in a biomimetic [FeFe]-H₂ase mimic, but modifications to the borane capping ligand that force a rotated structure observed in the native enzyme may provide further insights into the mechanism of proton reduction or encourage the formation of the not too often observed terminal hydride. Possible modifications to the borane Lewis acid R-groups is also an interesting design pathway that should be explored further.

A relatively unexplored avenue for [FeFe]-H₂ase mimics is metal-exchange cofactor mimics, in which the iron is replaced with a non-native metal while the primary coordination sphere remains intact. In paper IV I chose to investigate manganese metal exchange mimics because of the fun synthetic task and to explore the possibility that a dimanganese complex may be capable of proton reduction. Due to the presence of both iron and manganese in enzymes that carry out the same chemical transformations (such as superoxide dismutases), this study may provide interesting new perspectives for the evolutionary biology of [FeFe]-H₂ases. i.e. Is it possible there ever existed a [MnMn]-H₂ase in nature?

I revisited a previously reported dimanganese dithiolato carbonyl complex, confirmed its structure using crystallography, and demonstrated that the complex is indeed capable of reducing protons. Additionally I explored the substitution chemistry and synthesised two new phosphine substituted dimanganese complexes. The phosphine substituted complexes (**36b-d**) did not display clear proton reduction catalysis within the studied potential window. This was attributed to the significant negative shift in reduction potential compared to **36a**, and the surprising lack of protonation of the complexes in the presence of acid. Moreover, I recently attempted to synthesise a dicyanide substituted mimic and utilise it in artificial maturation of apo-HydA1. I was able to show that the complex does bind to the protein, as demonstrated through the presence of FTIR signatures after size-exclusion chromatography. (appendix 2). This project is ongoing, and more data should be collected to verify the structures of the new complexes.

The projects presented herein span many aspects of the H-cluster, and I hope that they provide some insight into important aspects when designing [FeFe]-H₂ase mimics, or [FeFe]-H₂ase inspired proton reduction catalysts. All of the results together ultimately show that every aspect of the H-cluster is important for successful proton reduction.

- A nitrogen bridgehead should be favoured for oxygen tolerance.

- A redox active ligand allows stabilisation of the redox states observed during catalysis, by spreading the electron density over multiple metal sites.
- Electron withdrawing ligands should be chosen to tune electron density such that the reduction occurs at mild potentials.
- Lewis acids can cap cyanide ligands, protecting them from proton attack during catalysis.
- Iron is an important metal for proton reduction in biology, however it is possible to reduce protons using a manganese metal exchange mimic.

Popular science description

In order to mitigate the effects of climate change and to meet global energy demands, sustainable sources of energy must be used. One promising tool to reach this goal is hydrogen. Hydrogen is recognised as the energy carrier of the future and a necessary aspect of the energy transition to a carbon-free economy.

An important question facing scientists today is “how can hydrogen be produced from sustainable sources?” And this is where hydrogenase enzymes can provide an answer. There are three types of hydrogenase, all of them use iron in their transformations of hydrogen or protons, in some cases in combination with nickel. Diiron hydrogenases are reported to interconvert hydrogen and protons at extremely high rates.

Hydrogenases have inspired the design and investigation of artificial hydrogenase mimics and other catalysts that convert protons to hydrogen or vice versa, and there are many design pathways to explore. Through the four projects presented in this thesis, I aim to investigate some of the components of the active site of the diiron hydrogenase.

The first project aims to investigate the differences in reactivity of two diiron hydrogenase mimics, and why one mimic may be more tolerant to decomposition caused by oxygen than the other mimic. In the second project a synthetic enzyme was made, and a component was added that enables the diiron cofactor mimic to gain or lose electrons. This project along with the third project aimed to investigate how the iron centres can be tuned in order to enable hydrogen production. Additionally, the third project investigated how vulnerable aspects of the diiron catalyst could be protected to enable hydrogen production. Finally the fourth project explored what happens if we replace the diiron centre with manganese, another Earth abundant metal, which is next to iron in the periodic table.

The work presented in this thesis demonstrates the promising aspects of synthetic diiron hydrogenase mimics for hydrogen production. The pitfalls of the diiron hydrogenase are highlighted and several routes for improvement are closely investigated.

Svensk Sammanfattning

För att mildra effekterna av klimatförändring och möta de globala energibehoven måste hållbara energikällor användas, till exempel vätgas. Vätgas är anses vara en av framtidens energibärare och är en nödvändig del av energiomställningen till en koldioxidfri ekonomi.

En viktig fråga för forskare idag är ”hur kan vätgas produceras från hållbara källor?” Det är här enzymen hydrogenas kan ge ett svar. Det finns tre typer av hydrogenas som alla använder järn (i vissa fall i kombination med nickel) för att omvandla protoner och elektroner till vätgas, och vätgas till protoner och elektroner. Di-järn-hydrogenas som bara innehåller järn har rapporterats utföra dessa kemiska omvandlingar med väldigt höga hastigheter.

Dessa enzym har inspirerat designen och utforskningen av artificiella hydrogenas-liknande katalysatorer och andra typer av katalysatorer som härmar de naturliga hydrogenasernas funktion att omvandla protoner till vätgas, och vätgas till protoner. Det finns många designvägar att utforska, och genom de fyra projekten presenterade i denna avhandling har mitt mål varit att undersöka några av beståndsdelarna i di-järn-hydrogenasets aktiva sätet.

I det första projektet undersöktes skillnaderna i reaktivitet av två olika artificiella katalysatorer som härmar di-järn-hydrogenas, och varför en av dem är mer resistent mot nedbrytning av syre än den andra artificiella katalysatorn. I det andra projektet byggdes ett artificiellt miniatyrhydrogenas, där en komponent lades till som kan acceptera eller donera elektroner. Det andra projektet tillsammans med det tredje projektet utforskade hur järnsäten kan finjusteras för att tillåta vätgasproduktion. I det tredje projektet undersöktes även hur känsliga delar av järnsäten kan skyddas för att förbättra vätgasproduktionen. Slutligen så undersöktes det i det fjärde projektet vad som sker när vi byter ut de två järnjonerna med manganjoner, en annan i jordskorpan rikligt förekommande metall som återfinns precis bredvid järn i det periodiska systemet.

Arbetet som presenteras i denna avhandling visar de lovande aspekterna av artificiella hydrogenas-liknande katalysatorer för vätgasproduktion. Fallgröparna associerade med di-järn-hydrogenas diskuteras och flera olika metoder för att förbättra deras vätgasproduktion har nära undersökts.

Acknowledgements

This was the most difficult thing I ever did. I could not have finished without the support I have received, and I have many people to thank for getting me here.

The first and most important people to thank are my very supportive family **Mum, Dad, James, Lucy, Granny P, Gramps, Grandma Wendy**. Especially to **Mum** and **Dad** for listening to me complain about the thesis writing and being so understanding and encouraging throughout the whole PhD and sending pictures of **Jerry2**.

Thank you to **Mark** for living with me and supporting me through the thesis writing process and for just being a really nice boyfriend.

Next I would like to thank all of my friends in the UK most of whom I know from my time in Sheffield. Thank you especially to **Hannah Fowler, Tom Blundell, Alex Matthews, Rike Dannheim, and Jess Whatley** for making me laugh, supporting me, providing words of encouragement and advice, and also for visiting me in Swedenland during my PhD.

Thanks also to **Mira Gamache, Liam Marshall, Sigrid Berglund, Robin Dürr** and **Tom Roseveare** for proofreading sections of my thesis and providing really helpful feedback.

Now it's time to thank all the amazing people I met in Uppsala. I will start with my immediate research group:

Thank you **Gustav** for giving me the opportunity to do my PhD here at Uppsala University and guiding me through the PhD process.

Thanks **Michael Cheah** for becoming my supervisor part way through my PhD.

Thank you **Sascha Ott** for being another supervisor, and an understanding and friendly presence in the synthetic chemistry labs (where I did most of my work!).

Thanks **Marco Lorenzi** for the positive vibes and moral support with EPR, and for sharing in the stresses of our parallel thesis writing

Thank you **Princess Cabotaje** bringing so much motivation and enthusiastic energy into the office and the green lab.

Thanks **Afridi** for being a kind colleague and fellow synthetic chemist in the group, and for your lovely sense of humour.

Thank you **Livia Meszaros** for Support with EPR and for keeping the lab in nice order.

Thanks **Moritz Senger** for the fun conversations and for supporting me with my FTIR experiments.

Thanks **Henrik Land** for the kind support during the PhD and for providing useful advice when I needed to try out new techniques in the green labs.

I would also like to thank the previous members of the group who have helped to move this research forward.

Thanks also to the BBC program for providing a nice work environment, and providing useful feedback in group meetings. Especially thanks to **Professor Johannes Messinger** for leading the program, and providing constructive feedback when needed. Thank you to **Professor Fikret Mamedov** and **Dr. Ping Huang** for their support with measuring and maintaining the EPR facilities, it would not be possible without your expertise.

Now I need to thank the people I worked with in the synthetic labs. Thank you **Ashleigh Castner** for being the best lab neighbor ever, and for letting me listen to my music in the lab, even when it was very emo...or techno. Thanks to **Brian McCarthy** for the same, and for being a really good friend and a big support through some of the tougher parts of the PhD. Thanks **Jordann Wells** and **Josh Green** for coming to work here, and teaching me so much about practical air-sensitive techniques, thanks also for being kind and funny co-workers. Thanks to **Andreas Orthaber** for helping me with crystals and NMR!

Thanks to **Anna Arkhypchuk** for assistance with NMR, and for being a very calm, fair and helpful person in the labs. Thanks to **Thuan, Rohan** and **Monika** for your help with maintaining the glovebox, especially that last few months! Thanks **Starla** for the nice conversations we have had, they have been helpful!

Thanks also to everyone else I have met in the department for making this such a nice place to work! Thanks **Nina** for all of the cake! And much needed Fika breaks!

Thank you to everyone I met in Sweden who made my time here so nice. Thanks to **Malin, Pia, Martyna, Julia, Emma** for providing me much needed relief from PhD stresses in the form of rowing.

References

1. N. Oreskes, in *Climate Modelling: Philosophical and Conceptual Issues*, eds. E. A. Lloyd and E. Winsberg, Springer International Publishing, Cham, 2018, DOI: 10.1007/978-3-319-65058-6_2, pp. 31-64.
2. R. E. Smalley, *MRS Bulletin*, 2005, **30**, 412-417.
3. D. G. Nocera, *ChemSusChem*, 2009, **2**, 387-390.
4. R. M. Bullock, J. G. Chen, L. Gagliardi, P. J. Chirik, O. K. Farha, C. H. Hendon, C. W. Jones, J. A. Keith, J. Klosin, S. D. Minteer, R. H. Morris, A. T. Radosevich, T. B. Rauchfuss, N. A. Strotman, A. Vojvodic, T. R. Ward, J. Y. Yang and Y. Surendranath, *Science*, 2020, **369**, eabc3183.
5. J. B. Goodenough and Y. Kim, *Chemistry of Materials*, 2010, **22**, 587-603.
6. J. B. Quinn, T. Waldmann, K. Richter, M. Kasper and M. Wohlfahrt-Mehrens, *Journal of The Electrochemical Society*, 2018, **165**, A3284-A3291.
7. I. Hore-Lacy, in *Nuclear Energy in the 21st Century*, ed. I. Hore-Lacy, Academic Press, Burlington, 2007, DOI: <https://doi.org/10.1016/B978-012373622-2/50004-0>, pp. 11-19.
8. F. c. a. hydrogen, 2019.
9. B. G. D. R. S. Zheng, *International council on clean transportation*, 2020.
10. J. M. Ogden, *Annual Review of Energy and the Environment*, 1999, **24**, 227-279.
11. S. P. S. Badwal, S. Giddey and C. Munnings, *WIREs Energy and Environment*, 2013, **2**, 473-487.
12. P. C. K. Vesborg and T. F. Jaramillo, *RSC Advances*, 2012, **2**, 7933-7947.
13. M. Hambourger, M. Gervaldo, D. Svedruzic, P. W. King, D. Gust, M. Ghirardi, A. L. Moore and T. A. Moore, *Journal of the American Chemical Society*, 2008, **130**, 2015-2022.
14. W. Lubitz, H. Ogata, O. Rüdiger and E. Reijerse, *Chemical Reviews*, 2014, **114**, 4081-4148.
15. J. T. Kleinhaus, F. Wittkamp, S. Yadav, D. Siegmund and U.-P. Apfel, *Chemical Society Reviews*, 2021, **50**, 1668-1784.

16. A. Volbeda, M.-H. Charon, C. Piras, E. C. Hatchikian, M. Frey and J. C. Fontecilla-Camps, *Nature*, 1995, **373**, 580-587.
17. Y. Higuchi, T. Yagi and N. Yasuoka, *Structure*, 1997, **5**, 1671-1680.
18. R. P. Happe, W. Roseboom, A. J. Pierik, S. P. J. Albracht and K. A. Bagley, *Nature*, 1997, **385**, 126-126.
19. S. Dementin, B. Burlat, A. L. De Lacey, A. Pardo, G. Adryanczyk-Perrier, B. Guigliarelli, V. M. Fernandez and M. Rousset, *Journal of Biological Chemistry*, 2004, **279**, 10508-10513.
20. I. Fdez. Galván, A. Volbeda, J. C. Fontecilla-Camps and M. J. Field, *Proteins: Structure, Function, and Bioinformatics*, 2008, **73**, 195-203.
21. E. Szöri-Dorogházi, G. Maróti, M. Szöri, A. Nyilasi, G. Rákhely and K. L. Kovács, *PLOS ONE*, 2012, **7**, e34666.
22. H. Ogata, *J-Stage*, 2015, **57**, 344-349.
23. T. Krämer, M. Kampa, W. Lubitz, M. van Gastel and F. Neese, *ChemBioChem*, 2013, **14**, 1898-1905.
24. R. K. Thauer, A.-K. Kaster, M. Goenrich, M. Schick, T. Hiromoto and S. Shima, *Annual Review of Biochemistry*, 2010, **79**, 507-536.
25. Y. Nicolet, *Nature Catalysis*, 2019, **2**, 481-482.
26. G. Huang, T. Wagner, M. D. Wodrich, K. Ataka, E. Bill, U. Ermler, X. Hu and S. Shima, *Nature Catalysis*, 2019, **2**, 537-543.
27. A. Volbeda, P. Amara, C. Darnault, J.-M. Mouesca, A. Parkin, M. M. Roessler, F. A. Armstrong and J. C. Fontecilla-Camps, *Proceedings of the National Academy of Sciences*, 2012, **109**, 5305-5310.
28. C. Madden, M. D. Vaughn, I. Díez-Pérez, K. A. Brown, P. W. King, D. Gust, A. L. Moore and T. A. Moore, *Journal of the American Chemical Society*, 2012, **134**, 1577-1582.
29. E. M. Shepard, F. Mus, J. N. Betz, A. S. Byer, B. R. Duffus, J. W. Peters and J. B. Broderick, *Biochemistry*, 2014, **53**, 4090-4104.
30. A. Silakov, B. Wenk, E. Reijerse and W. Lubitz, *Physical Chemistry Chemical Physics*, 2009, **11**, 6592-6599.
31. J. W. Peters, W. N. Lanzilotta, B. J. Lemon and L. C. Seefeldt, *Science*, 1998, **282**, 1853-1858.
32. Y. Nicolet, C. Piras, P. Legrand, C. E. Hatchikian and J. C. Fontecilla-Camps, *Structure*, 1999, **7**, 13-23.
33. P. E. M. Siegbahn and R.-Z. Liao, *The Journal of Physical Chemistry A*, 2020, **124**, 10540-10549.
34. M. Haumann and S. T. Stripp, *Accounts of Chemical Research*, 2018, **51**, 1755-1763.
35. H. Ogata and W. Lubitz, in *Reference Module in Life Sciences*, Elsevier, 2020, DOI: <https://doi.org/10.1016/B978-0-12-809633-8.21396-4>.
36. M. A. Martini, O. Rüdiger, N. Breuer, B. Nöring, S. DeBeer, P. Rodríguez-Maciá and J. A. Birrell, *Journal of the American Chemical Society*, 2021, **143**, 18159-18171.

37. J. Duan, M. Senger, J. Esselborn, V. Engelbrecht, F. Wittkamp, U.-P. Apfel, E. Hofmann, S. T. Stripp, T. Happe and M. Winkler, *Nature Communications*, 2018, **9**, 4726.
38. M. Senger, S. Mebs, J. Duan, O. Shulenina, K. Laun, L. Kertess, F. Wittkamp, U.-P. Apfel, T. Happe, M. Winkler, M. Haumann and S. T. Stripp, *Physical Chemistry Chemical Physics*, 2018, **20**, 3128-3140.
39. P. Rodríguez-Maciá, L. M. Galle, R. Bjornsson, C. Lorent, I. Zebger, Y. Yoda, S. P. Cramer, S. DeBeer, I. Span and J. A. Birrell, *Angewandte Chemie International Edition*, 2020, **59**, 16786-16794.
40. J. A. Birrell, P. Rodríguez-Maciá, E. J. Reijerse, M. A. Martini and W. Lubitz, *Coordination Chemistry Reviews*, 2021, **449**, 214191.
41. C. Lorent, S. Katz, J. Duan, C. J. Kulka, G. Caserta, C. Teutloff, S. Yadav, U.-P. Apfel, M. Winkler, T. Happe, M. Horch and I. Zebger, *Journal of the American Chemical Society*, 2020, **142**, 5493-5497.
42. C. F. Megarity, J. Esselborn, S. V. Hexter, F. Wittkamp, U.-P. Apfel, T. Happe and F. A. Armstrong, *Journal of the American Chemical Society*, 2016, **138**, 15227-15233.
43. G. Caserta, L. Pecqueur, C. Papini and M. Fontecave, in *Encyclopedia of Inorganic and Bioinorganic Chemistry*, DOI: <https://doi.org/10.1002/9781119951438.eibc2472>, pp. 1-18.
44. O. Lampret, J. Esselborn, R. Haas, A. Rutz, R. L. Booth, L. Kertess, F. Wittkamp, C. F. Megarity, F. A. Armstrong, M. Winkler and T. Happe, *Proceedings of the National Academy of Sciences*, 2019, **116**, 15802-15810.
45. A. S. Byer, E. M. Shepard, M. W. Ratzloff, J. N. Betz, P. W. King, W. E. Broderick and J. B. Broderick, *JBIC Journal of Biological Inorganic Chemistry*, 2019, **24**, 783-792.
46. E. M. Shepard, S. Impano, B. R. Duffus, A. Pagnier, K. S. Duschene, J. N. Betz, A. S. Byer, A. Galambas, E. C. McDaniel, H. Watts, S. E. McGlynn, J. W. Peters, W. E. Broderick and J. B. Broderick, *Dalton Transactions*, 2021, **50**, 10405-10422.
47. D. W. Mulder, D. O. Ortillo, D. J. Gardenghi, A. V. Naumov, S. S. Ruebush, R. K. Szilagyi, B. Huynh, J. B. Broderick and J. W. Peters, *Biochemistry*, 2009, **48**, 6240-6248.
48. D. W. Mulder, E. S. Boyd, R. Sarma, R. K. Lange, J. A. Endrizzi, J. B. Broderick and J. W. Peters, *Nature*, 2010, **465**, 248-251.
49. P. W. King, M. C. Posewitz, M. L. Ghirardi and M. Seibert, *Journal of Bacteriology*, 2006, **188**, 2163-2172.
50. G. Berggren, A. Adamska, C. Lambertz, T. R. Simmons, J. Esselborn, M. Atta, S. Gambarelli, J. M. Mouesca, E. Reijerse, W. Lubitz, T. Happe, V. Artero and M. Fontecave, *Nature*, 2013, **499**, 66-69.
51. J. Esselborn, C. Lambertz, A. Adamska-Venkatesh, T. Simmons, G. Berggren, J. Noth, J. Siebel, A. Hemschemeier, V. Artero, E. Reijerse,

- M. Fontecave, W. Lubitz and T. Happe, *Nature Chemical Biology*, 2013, **9**, 607-609.
52. S.-A. Freibert, B. D. Weiler, E. Bill, A. J. Pierik, U. Mühlenhoff and R. Lill, in *Methods in Enzymology*, ed. S. S. David, Academic Press, 2018, vol. 599, pp. 197-226.
 53. A. Le Cloirec, S. C. Davies, D. J. Evans, D. L. Hughes, C. J. Pickett, S. P. Best and S. Borg, *Chemical Communications*, 1999, DOI: 10.1039/A906391I, 2285-2286.
 54. E. J. Lyon, I. P. Georgakaki, J. H. Reibenspies and M. Y. Darensbourg, *Angewandte Chemie International Edition*, 1999, **38**, 3178-3180.
 55. F. Zhang, C. P. Richers, T. J. Woods and T. B. Rauchfuss, *Angewandte Chemie International Edition*, 2021, **60**, 20744-20747.
 56. C. Esmieu, M. Guo, H. J. Redman, M. Lundberg and G. Berggren, *Dalton Transactions*, 2019, **48**, 2280-2284.
 57. H. J. Redman, P. Huang, M. Haumann, M. H. Cheah and G. Berggren, *Dalton Transactions*, 2022, DOI: 10.1039/D1DT03896F.
 58. M. E. Ahmed, S. Dey, M. Y. Darensbourg and A. Dey, *Journal of the American Chemical Society*, 2018, **140**, 12457-12468.
 59. F. Gloaguen and T. B. Rauchfuss, *Chemical Society Reviews*, 2009, **38**, 100-108.
 60. J. He, C.-L. Deng, Y. Li, Y.-L. Li, Y. Wu, L.-K. Zou, C. Mu, Q. Luo, B. Xie, J. Wei, J.-W. Hu, P.-H. Zhao and W. Zheng, *Organometallics*, 2017, **36**, 1322-1330.
 61. Y. Li and T. B. Rauchfuss, *Chemical Reviews*, 2016, **116**, 7043-7077.
 62. A. D. Merinero, A. Collado, L. Casarrubios, M. Gómez-Gallego, C. Ramírez de Arellano, A. Caballero, F. Zapata and M. A. Sierra, *Inorganic Chemistry*, 2019, **58**, 16267-16278.
 63. I. K. Pandey, T. Agarwal, S. M. Mobin, M. Stein and S. Kaur-Ghumaan, *ACS Omega*, 2021, **6**, 4192-4203.
 64. D. Schilter, J. M. Camara, M. T. Huynh, S. Hammes-Schiffer and T. B. Rauchfuss, *Chemical Reviews*, 2016, **116**, 8693-8749.
 65. D. G. Unwin, S. Ghosh, F. Ridley, M. G. Richmond, K. B. Holt and G. Hogarth, *Dalton Transactions*, 2019, **48**, 6174-6190.
 66. F. Wittkamp, E. B. Boydas, M. Roemelt and U.-P. Apfel, *Catalysts*, 2020, **10**, 522.
 67. R. Kositzki, S. Mebs, N. Schuth, N. Leidel, L. Schwartz, M. Karnahl, F. Wittkamp, D. Daunke, A. Grohmann, U.-P. Apfel, F. Gloaguen, S. Ott and M. Haumann, *Dalton Transactions*, 2017, **46**, 12544-12557.
 68. C. Tard, X. Liu, S. K. Ibrahim, M. Bruschi, L. D. Gioia, S. C. Davies, X. Yang, L.-S. Wang, G. Sawers and C. J. Pickett, *Nature*, 2005, **433**, 610-613.
 69. R. Zaffaroni, T. B. Rauchfuss, D. L. Gray, L. De Gioia and G. Zampella, *Journal of the American Chemical Society*, 2012, **134**, 19260-19269.

70. H. Li and T. B. Rauchfuss, *Journal of the American Chemical Society*, 2002, **124**, 726-727.
71. V. C. C. Wang, C. Esmieu, H. J. Redman, G. Berggren and L. Hammarström, *Dalton Transactions*, 2020, **49**, 858-865.
72. J.-F. Capon, S. El Hassnaoui, F. Gloaguen, P. Schollhammer and J. Talarmin, *Organometallics*, 2005, **24**, 2020-2022.
73. C. A. Boyke, T. B. Rauchfuss, S. R. Wilson, M.-M. Rohmer and M. Bénard, *Journal of the American Chemical Society*, 2004, **126**, 15151-15160.
74. M. T. Olsen, M. Bruschi, L. De Gioia, T. B. Rauchfuss and S. R. Wilson, *Journal of the American Chemical Society*, 2008, **130**, 12021-12030.
75. J. I. van der Vlugt, T. B. Rauchfuss and S. R. Wilson, *Chemistry – A European Journal*, 2006, **12**, 90-98.
76. X. Zhao, I. P. Georgakaki, M. L. Miller, R. Mejia-Rodriguez, C.-Y. Chiang and M. Y. Darensbourg, *Inorganic Chemistry*, 2002, **41**, 3917-3928.
77. D. Chong, I. P. Georgakaki, R. Mejia-Rodriguez, J. Sanabria-Chinchilla, M. P. Soriaga and M. Y. Darensbourg, *Dalton Transactions*, 2003, DOI: 10.1039/B304283A, 4158-4163.
78. F. Gloaguen, J. D. Lawrence and T. B. Rauchfuss, *Journal of the American Chemical Society*, 2001, **123**, 9476-9477.
79. W. Wang, M. J. Nilges, T. B. Rauchfuss and M. Stein, *Journal of the American Chemical Society*, 2013, **135**, 3633-3639.
80. M. E. Carroll, B. E. Barton, T. B. Rauchfuss and P. J. Carroll, *Journal of the American Chemical Society*, 2012, **134**, 18843-18852.
81. S. Roy, T.-A. D. Nguyen, L. Gan and A. K. Jones, *Dalton Transactions*, 2015, **44**, 14865-14876.
82. M. K. Harb, U.-P. Apfel, J. Kübel, H. Görls, G. A. N. Felton, T. Sakamoto, D. H. Evans, R. S. Glass, D. L. Lichtenberger, M. El-khateeb and W. Weigand, *Organometallics*, 2009, **28**, 6666-6675.
83. M. K. Harb, T. Niksch, J. Windhager, H. Görls, R. Holze, L. T. Lockett, N. Okumura, D. H. Evans, R. S. Glass, D. L. Lichtenberger, M. El-khateeb and W. Weigand, *Organometallics*, 2009, **28**, 1039-1048.
84. L.-C. Song, B. Gai, Z.-H. Feng, Z.-Q. Du, Z.-J. Xie, X.-J. Sun and H.-B. Song, *Organometallics*, 2013, **32**, 3673-3684.
85. J. P. Collman, R. K. Rothrock, R. G. Finke, E. J. Moore and F. Rose-Munch, *Inorganic Chemistry*, 1982, **21**, 146-156.
86. M. H. Cheah, S. J. Borg and S. P. Best, *Inorganic Chemistry*, 2007, **46**, 1741-1750.
87. F. Arrigoni, F. Rizza, J. Vertemara, R. Breglia, C. Greco, L. Bertini, G. Zampella and L. De Gioia, *ChemPhysChem*, 2020, **21**, 2279-2292.
88. J. A. Cabeza, M. A. Martínez-García, V. Riera, D. Ardura and S. García-Granda, *Organometallics*, 1998, **17**, 1471-1477.

89. G. A. N. Felton, A. K. Vannucci, J. Chen, L. T. Lockett, N. Okumura, B. J. Petro, U. I. Zakai, D. H. Evans, R. S. Glass and D. L. Lichtenberger, *Journal of the American Chemical Society*, 2007, **129**, 12521-12530.
90. M. Mirmohades, S. Pullen, M. Stein, S. Maji, S. Ott, L. Hammarström and R. Lomoth, *Journal of the American Chemical Society*, 2014, **136**, 17366-17369.
91. A. T. Castner, B. A. Johnson, S. M. Cohen and S. Ott, *Journal of the American Chemical Society*, 2021, **143**, 7991-7999.
92. S. Pullen, H. Fei, A. Orthaber, S. M. Cohen and S. Ott, *Journal of the American Chemical Society*, 2013, **135**, 16997-17003.
93. X. Zhu, W. Zhong and X. Liu, *International Journal of Hydrogen Energy*, 2016, **41**, 14068-14078.
94. S. E. Mulholland, B. R. Gibney, F. Rabanal and P. L. Dutton, *Journal of the American Chemical Society*, 1998, **120**, 10296-10302.
95. L. Michaelis and E. S. Hill *Journal of General Physiology*, 1933, **16**, 859-873.
96. P. Connolly and J. H. Espenson, *Inorganic Chemistry*, 1986, **25**, 2684-2688.
97. J. L. Dempsey, B. S. Brunschwig, J. R. Winkler and H. B. Gray, *Accounts of Chemical Research*, 2009, **42**, 1995-2004.
98. N. Kaeffer, M. Chavarot-Kerlidou and V. Artero, *Accounts of Chemical Research*, 2015, **48**, 1286-1295.
99. E. S. Rountree, D. J. Martin, B. D. McCarthy and J. L. Dempsey, *ACS Catalysis*, 2016, **6**, 3326-3335.
100. A. M. Appel, D. L. DuBois and M. Rakowski DuBois, *Journal of the American Chemical Society*, 2005, **127**, 12717-12726.
101. C. J. Curtis, A. Miedaner, R. Ciancanelli, W. W. Ellis, B. C. Noll, M. Rakowski DuBois and D. L. DuBois, *Inorganic Chemistry*, 2003, **42**, 216-227.
102. J. Y. Yang, R. M. Bullock, W. J. Shaw, B. Twamley, K. Frazee, M. R. DuBois and D. L. DuBois, *Journal of the American Chemical Society*, 2009, **131**, 5935-5945.
103. M. Rakowski Dubois and D. L. Dubois, *Accounts of Chemical Research*, 2009, **42**, 1974-1982.
104. S. Trasatti, *Journal of Electroanalytical Chemistry and Interfacial Electrochemistry*, 1972, **39**, 163-184.
105. P. Quaino, F. Juarez, E. Santos and W. Schmickler, *Beilstein J Nanotechnol*, 2014, **5**, 846-854.
106. T. R. Cook, D. K. Dogutan, S. Y. Reece, Y. Surendranath, T. S. Teets and D. G. Nocera, *Chemical Reviews*, 2010, **110**, 6474-6502.
107. Q. Lu, G. S. Hutchings, W. Yu, Y. Zhou, R. V. Forest, R. Tao, J. Rosen, B. T. Yonemoto, Z. Cao, H. Zheng, J. Q. Xiao, F. Jiao and J. G. Chen, *Nature Communications*, 2015, **6**, 6567.

108. A. K. Cheong, A. Lasia and J. Lessard, *Journal of The Electrochemical Society*, 1993, **140**, 2721-2725.
109. B. Hinnemann, P. G. Moses, J. Bonde, K. P. Jørgensen, J. H. Nielsen, S. Horch, I. Chorkendorff and J. K. Nørskov, *Journal of the American Chemical Society*, 2005, **127**, 5308-5309.
110. Z. W. Seh, J. Kibsgaard, C. F. Dickens, I. Chorkendorff, J. K. Nørskov and T. F. Jaramillo, *Science*, 2017, **355**, eaad4998.
111. D. Atkins, *Elements of physical chemistry*, Oxford university press, Oxford, 6th edn., 2009.
112. A. K. Brisdon, *Inorganic Spectroscopic Methods*, Oxford university press, United States, 2nd edn., 1998.
113. J. Chatt and L. A. Duncanson, *Journal of the Chemical Society (Resumed)*, 1953, DOI: 10.1039/JR9530002939, 2939-2947.
114. J. Chatt, L. A. Duncanson and L. M. Venzani, *Journal of the Chemical Society (Resumed)*, 1955, DOI: 10.1039/JR9550004456, 4456-4460.
115. Z. Cao and M. B. Hall, *Journal of the American Chemical Society*, 2001, **123**, 3734-3742.
116. J. R. B. John A. Weil, *Electron Paramagnetic Resonance: Elementary theory and practical applications*, Wiley and Sons Inc., New Jersey and Canada, second edn., 2007.
117. D. E. Sayers, E. A. Stern and F. W. Lytle, *Physical Review Letters*, 1971, **27**, 1204-1207.
118. J. Yano and V. K. Yachandra, *Photosynthesis Research*, 2009, **102**, 241.
119. G. R. Shulman, Y. Yafet, P. Eisenberger and W. E. Blumberg, *Proceedings of the National Academy of Sciences*, 1976, **73**, 1384-1388.
120. N. Leidel, P. Chernev, K. G. V. Havelius, S. Ezzaher, S. Ott and M. Haumann, *Inorganic Chemistry*, 2012, **51**, 4546-4559.
121. N. Leidel, C.-H. Hsieh, P. Chernev, K. G. V. Sigfridsson, M. Y. Darensbourg and M. Haumann, *Dalton Transactions*, 2013, **42**, 7539-7554.
122. F. W. Lytle, E. M. Larson, R. B. Gregor, E. C. Marques and A. J. Panson, *Physica B: Condensed Matter*, 1989, **158**, 471-472.
123. N. Elgrishi, K. J. Rountree, B. D. McCarthy, E. S. Rountree, T. T. Eisenhart and J. L. Dempsey, *Journal of Chemical Education*, 2018, **95**, 197-206.
124. B. D. McCarthy, C. L. Donley and J. L. Dempsey, *Chemical Science*, 2015, **6**, 2827-2834.
125. C. Costentin, D. G. Nocera and C. N. Brodsky, *Proceedings of the National Academy of Sciences*, 2017, **114**, 11303-11308.
126. J.-M. Savéant, *Chemical Reviews*, 2008, **108**, 2348-2378.
127. E. S. Rountree, B. D. McCarthy, T. T. Eisenhart and J. L. Dempsey, *Inorganic Chemistry*, 2014, **53**, 9983-10002.

128. D. J. Martin, B. D. McCarthy, E. S. Rountree and J. L. Dempsey, *Dalton Transactions*, 2016, **45**, 9970-9976.
129. C. Lambertz, N. Leidel, K. G. V. Havelius, J. Noth, P. Chernev, M. Winkler, T. Happe and M. Haumann, *Journal of Biological Chemistry*, 2011, **286**, 40614-40623.
130. M. T. Stiebritz and M. Reiher, *Chemical Science*, 2012, **3**, 1739-1751.
131. S. T. Stripp, G. Goldet, C. Brandmayr, O. Sanganas, K. A. Vincent, M. Haumann, F. A. Armstrong and T. Happe, *Proceedings of the National Academy of Sciences*, 2009, **106**, 17331-17336.
132. B. Kandemir, L. Kubie, Y. Guo, B. Sheldon and K. L. Bren, *Inorganic Chemistry*, 2016, **55**, 1355-1357.
133. S. Dey, A. Rana, D. Crouthers, B. Mondal, P. K. Das, M. Y. Darensbourg and A. Dey, *Journal of the American Chemical Society*, 2014, **136**, 8847-8850.
134. M. K. Bruska, M. T. Stiebritz and M. Reiher, *Journal of the American Chemical Society*, 2011, **133**, 20588-20603.
135. M. T. Stiebritz and M. Reiher, *Inorganic Chemistry*, 2009, **48**, 7127-7140.
136. J. Esselborn, L. Kertess, U.-P. Apfel, E. Hofmann and T. Happe, *Journal of the American Chemical Society*, 2019, **141**, 17721-17728.
137. M. E. Peover and B. S. White, *Electrochimica Acta*, 1966, **11**, 1061-1067.
138. J. Petlicki and T. G. M. van de Ven, *Journal of the Chemical Society, Faraday Transactions*, 1998, **94**, 2763-2767.
139. M. Y. Darensbourg and W. Weigand, *European Journal of Inorganic Chemistry*, 2011, **2011**, 994-1004.
140. S. J. Borg, T. Behrsing, S. P. Best, M. Razavet, X. Liu and C. J. Pickett, *Journal of the American Chemical Society*, 2004, **126**, 16988-16999.
141. T. Liu, B. Li, M. L. Singleton, M. B. Hall and M. Y. Darensbourg, *Journal of the American Chemical Society*, 2009, **131**, 8296-8307.
142. I. Aguirre de Carcer, A. DiPasquale, A. L. Rheingold and D. M. Heinekey, *Inorganic Chemistry*, 2006, **45**, 8000-8002.
143. S. Wang, A. Aster, M. Mirmohades, R. Lomoth and L. Hammarström, *Inorganic Chemistry*, 2018, **57**, 768-776.
144. E. Raamat, K. Kaupmees, G. Ovsjannikov, A. Trummal, A. Kütt, J. Saame, I. Koppel, I. Kaljurand, L. Lipping, T. Rodima, V. Pihl, I. A. Koppel and I. Leito, *Journal of Physical Organic Chemistry*, 2013, **26**, 162-170.
145. A. Roy, C. Madden and G. Ghirlanda, *Chemical Communications*, 2012, **48**, 9816-9818.
146. S. Chakraborty, E. H. Edwards, B. Kandemir and K. L. Bren, *Inorganic Chemistry*, 2019, **58**, 16402-16410.
147. V. Firpo, J. M. Le, V. Pavone, A. Lombardi and K. L. Bren, *Chemical Science*, 2018, **9**, 8582-8589.

148. Y. Guo, J. R. Stroka, B. Kandemir, C. E. Dickerson and K. L. Bren, *Journal of the American Chemical Society*, 2018, **140**, 16888-16892.
149. B. Ginovska-Pangovska, A. Dutta, M. L. Reback, J. C. Linehan and W. J. Shaw, *Accounts of Chemical Research*, 2014, **47**, 2621-2630.
150. J. A. Laureanti, M. O'Hagan and W. J. Shaw, *Sustainable Energy & Fuels*, 2019, **3**, 3260-3278.
151. G. Berggren, A. Adamska, C. Lambertz, T. R. Simmons, J. Esselborn, M. Atta, S. Gambarelli, J. M. Mouesca, E. Reijerse, W. Lubitz, T. Happe, V. Artero and M. Fontecave, *Nature*, 2013, **499**, 66.
152. J. M. Camara and T. B. Rauchfuss, *Nature Chemistry*, 2012, **4**, 26-30.
153. A. K. Jones, B. R. Lichtenstein, A. Dutta, G. Gordon and P. L. Dutton, *Journal of the American Chemical Society*, 2007, **129**, 14844-14845.
154. B. Guigliarelli and P. Bertrand, in *Advances in Inorganic Chemistry*, ed. A. G. Sykes, Academic Press, 1999, vol. 47, pp. 421-497.
155. L. Kertess, A. Adamska-Venkatesh, P. Rodríguez-Maciá, O. Rüdiger, W. Lubitz and T. Happe, *Chemical Science*, 2017, **8**, 8127-8137.
156. B. J. McNicholas, R. H. Grubbs, J. R. Winkler, H. B. Gray and E. Despagne-Ayoub, *Chemical Science*, 2019, **10**, 3623-3626.
157. B. C. Manor and T. B. Rauchfuss, *Journal of the American Chemical Society*, 2013, **135**, 11895-11900.
158. B. C. Manor, M. R. Ringenberg and T. B. Rauchfuss, *Inorganic Chemistry*, 2014, **53**, 7241-7247.
159. G. Eilers, L. Schwartz, M. Stein, G. Zampella, L. de Gioia, S. Ott and R. Lomoth, *Chemistry – A European Journal*, 2007, **13**, 7075-7084.
160. S. Stoll, in *Multifrequency Electron Paramagnetic Resonance*, 2014, DOI: <https://doi.org/10.1002/9783527672431.ch3>, pp. 69-138.
161. S. Stoll and A. Schweiger, *Journal of Magnetic Resonance*, 2006, **178**, 42-55.
162. A. K. Justice, R. C. Linck and T. B. Rauchfuss, *Inorganic Chemistry*, 2006, **45**, 2406-2412.
163. C. Sommer, C. P. Richers, W. Lubitz, T. B. Rauchfuss and E. J. Reijerse, *Angewandte Chemie International Edition*, 2018, **57**, 5429-5432.
164. H.-J. Pan and X. Hu, *Angewandte Chemie International Edition*, 2020, **59**, 4942-4946.
165. H.-J. Pan, G. Huang, M. D. Wodrich, F. F. Tirani, K. Ataka, S. Shima and X. Hu, *Nature Chemistry*, 2019, **11**, 669-675.
166. Y. Sheng, I. A. Abreu, D. E. Cabelli, M. J. Maroney, A.-F. Miller, M. Teixeira and J. S. Valentine, *Chemical Reviews*, 2014, **114**, 3854-3918.
167. C. J. BROCK and J. I. HARRIS, *Biochemical Society Transactions*, 1977, **5**, 1537-1539.
168. J. W. Whittaker, *Archives of Biochemistry and Biophysics*, 2012, **525**, 111-120.

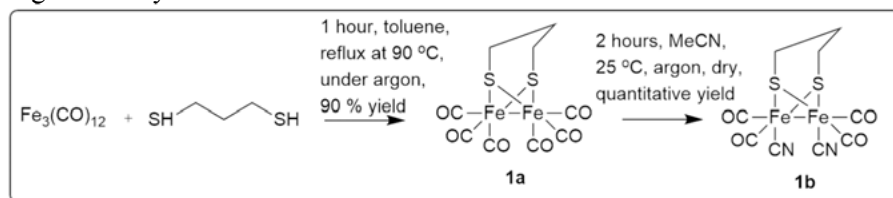
169. R. D. Adams, O.-S. Kwon and M. D. Smith, *Israel Journal of Chemistry*, 2001, **41**, 197-206.
170. R. D. Adams, O. S. Kwon and M. D. Smith, *Inorganic Chemistry*, 2001, **40**, 5322-5323.
171. R. D. Adams and S. B. Falloon, *Journal of the American Chemical Society*, 1994, **116**, 10540-10547.
172. R. D. Adams and J. L. Perrin, *Journal of the American Chemical Society*, 1999, **121**, 3984-3991.
173. R. B. King and C. A. Eggers, *Inorganic Chemistry*, 1968, **7**, 340-345.
174. R. B. King and C. A. Eggers, *Inorganic Chemistry*, 1968, **7**, 1214-1218.
175. E. Lindner, I. P. Butz, S. Hoehne, W. Hiller and R. Fawzi, *Journal of Organometallic Chemistry*, 1983, **259**, 99-117.
176. J. P. W. Schroth, *Chimia*, 1964, **18**.
177. L.-F. Radu, A. A. A. Attia, R. Silaghi-Dumitrescu, A. Lupan and R. B. King, *Dalton Transactions*, 2019, **48**, 324-332.
178. N. Wang, M. Wang, T. Liu, P. Li, T. Zhang, M. Y. Darensbourg and L. Sun, *Inorganic Chemistry*, 2008, **47**, 6948-6955.
179. M. T. Olsen, T. B. Rauchfuss and R. Zaffaroni, *Organometallics*, 2012, **31**, 3447-3450.
180. R. Zaffaroni, T. B. Rauchfuss, A. Fuller, L. De Gioia and G. Zampella, *Organometallics*, 2013, **32**, 232-238.
181. C. Esmieu and G. Berggren, *Dalton Transactions*, 2016, **45**, 19242-19248.
182. P. M. Treichel, J. H. Morris and F. G. A. Stone, *Journal of the Chemical Society (Resumed)*, 1963, DOI: 10.1039/JR9630000720, 720-723.
183. D. Seyferth, G. B. Womack, M. K. Gallagher, M. Cowie, B. W. Hames, J. P. Fackler and A. M. Mazany, *Organometallics*, 1987, **6**, 283-294.
184. R. D. Bethel, D. J. Crouthers, C.-H. Hsieh, J. A. Denny, M. B. Hall and M. Y. Darensbourg, *Inorganic Chemistry*, 2015, **54**, 3523-3535.
185. A. M. Lunsford, J. H. Blank, S. Moncho, S. C. Haas, S. Muhammad, E. N. Brothers, M. Y. Darensbourg and A. A. Bengali, *Inorganic Chemistry*, 2016, **55**, 964-973.
186. X. Zhou, B. E. Barton, G. M. Chambers, T. B. Rauchfuss, F. Arrigoni and G. Zampella, *Inorganic Chemistry*, 2016, **55**, 3401-3412.
187. P. F. Brandt, D. A. Lesch, P. R. Stafford, T. B. Rauchfuss, J. W. Kolis and L. C. Roof, in *Inorganic Syntheses*, 1996, DOI: <https://doi.org/10.1002/9780470132623.ch17>, pp. 112-116.
188. J. L. Stanley, T. B. Rauchfuss and S. R. Wilson, *Organometallics*, 2007, **26**, 1907-1911.
189. J. F. Siebel, A. Adamska-Venkatesh, K. Weber, S. Rumpel, E. Reiherse and W. Lubitz, *Biochemistry*, 2015, **54**, 1474-1483.

Appendix I – Synthesis of selected cofactor mimics

A1.1 $[\text{Fe}_2(\mu\text{-pdt})(\text{CO})_4(\text{CN})_2][\text{Et}_4\text{N}]$

Synthesis of compound $\mathbf{1b}^{2-}$ is much simpler than that of $\mathbf{2b}^{2-}$. Starting from triirronododecacarbonyl and 1,3-propanedithiol in toluene one can produce $[\text{Fe}_2(\mu\text{-pdt})(\text{CO})_6]$ ($\mathbf{1a}$) by stirring at 90 °C.¹⁸³ This yields a crude mixture that is purified by a silica column with pentane eluent, the purified product forms orange crystals on the rotavap.

Following purification of $\mathbf{1a}$, dissolution in acetonitrile and addition of 2.1 equivalents of tetraethylammonium cyanide $[\text{Et}_4\text{N}^+][\text{CN}^-]$ results in substitution of two CO ligands with two CN^- ligands over the course of 2 hours at room temperature.⁵⁴ In a very dry Schlenk flask covered in foil. The solvent should be evaporated and the product redissolved in degassed acetone. Then the product should be precipitated by adding degassed ethyl acetate, and storing the flask in the freezer over night (−30 °C). Finally, wash the supernatant should be removed, and the red-brown solid should be washed repeatedly with degassed ethyl acetate.



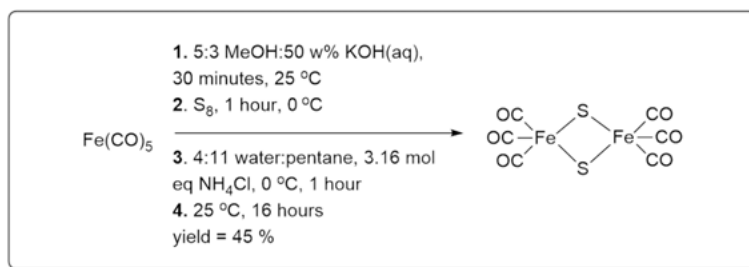
Scheme A1.1. Synthetic route to compound $\mathbf{1b}^{2-}$.

$\mathbf{1a}$ is in itself an important hydrogenase mimic and its chemistry and redox properties have been thoroughly studied.^{53, 140} $\mathbf{1a}$ is a very robust compound, it is stable in air and moisture, and the Fe_2S_2 core can withstand many chemical reactions. This makes it ideal for further modification to create a plethora of structural and functional mimics. The two areas where modification can take place are through substitution of the CO ligands, or through changing of the dithiolato bridgehead. The CO ligands are usually substituted by Lewis acids such as cyanides ($\mathbf{1b}^{2-}$ and $\mathbf{2b}^{2-}$),⁵⁴ phosphines,⁷⁵ carbenes.¹⁸⁴ Addition of Lewis acids allows tuning of the electron density and therefore the redox properties of the diiron centre,^{75, 185, 186} although this does lead to a more basic more easily oxidisable complex that is vulnerable to attack by nucleophiles. The

dithiolato bridgheads can be modified to tune the electron density on the iron or to introduce a new functional group or an outer coordination sphere to the complex.^{81, 82, 89, 145}

A1.2 [Fe₂(μ-adt)(CO)₄(CN)₂]₂[Et₄N]

Synthesis of **2a** and **2b**²⁻ is more involved.⁶⁹ The first step is messy and requires the use of a mechanical stirrer, I recommend that this step is carried out on a large scale (5-10 g) so that you do not have to repeat it often.



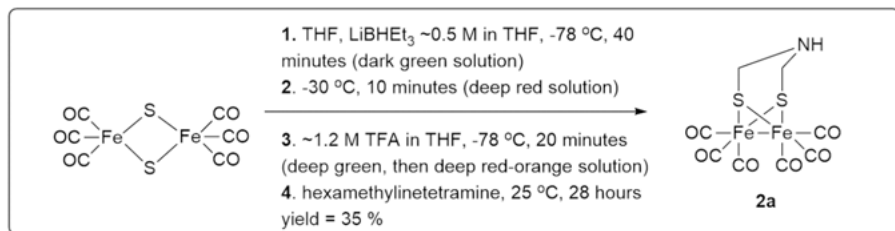
Scheme A1.2. Formation of diiron-μ-disulfidohexacarbonyl.

Start by degassing a mixture of freshly prepared methanol and 50 weight % potassium hydroxide solution in water by bubbling with argon for 60 minutes. To this, add the iron pentacarbonyl and stir for 30 minutes at room temperature. Next the reaction mixture is cooled down to 0 °C before adding sulphur powder and stirring for 60 minutes. In the meantime, start degassing a 4:11 mixture of water and pentane, then add it to the reaction mixture. Allow the reaction mixture to cool back down to 0 °C, then add the ammonium chloride (NH₄Cl). Do this slowly, because gas is produced upon addition of the NH₄Cl. After stirring the mixture for 1 hour at 0 °C, the reaction can be allowed to reach room temperature, it will appear as a black sticky tar. Stir the reaction for 16 hours at room temperature, the reaction should remain under a positive flow of argon throughout.

Filter the reaction mixture through celite. This is harder than it sounds because the crude product is extremely sticky. Wash the crude product with lots of pentane, until the residue is black and a little bit shiny (almost metallic). Collect the filtrate, dry over sodium sulfate and evaporate the solvent. Filtering the crude product can take more than 1 litre of pentane, so if you have a clean enough rotavap, it is good to recycle your solvent. Note, the black sticky tar product is very difficult to clean, and THF is really the only solvent that can remove it from the floor (and walls...and windows) of the fumehood.

Purify the product on a silica column with pentane eluent. You will observe that one brown-red band elutes (diiron μ-disulfido hexacarbonyl,

$\text{Fe}_2(\mu\text{-S}_2)(\text{CO})_6$, and a black solid remains on the top of the column (this is just junk iron and FeS oligomers). Evaporating the solvent yields a dark brown–red solid (3 g, 45 % yield). The original literature procedure states that the product should be purified by sublimation using a cold finger over 2 days instead of column chromatography. However in my experience column chromatography works just fine, and is much faster and easier than using a sublimation finger.^{187, 188}



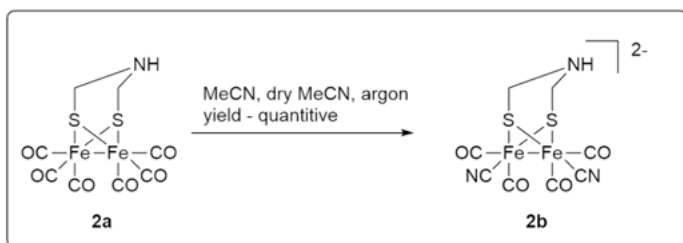
Scheme A1.3. Synthetic route to complex **2a**.

Before starting the next reaction (figure 1.8),^{69, 70} prepare hexamethylenetetramine by grinding with a pestle and mortar and drying in a SSchlenk flask under vacuum for two days. This reaction is air and moisture sensitive, and there are several things that can go wrong, as will be described herein. Having said that, it is a beautiful reaction with lots of fun colour changes!

Equip a 250 mL SSchlenk flask with a dropping funnel. Dry the glassware using a heat gun for 10 minutes, and apply vacuum while the glassware cools. Repeat this twice, the glassware should be bone dry. Once the glassware is cool, dissolve diiron μ -disulfido hexacarbonyl (1 g) in THF (60 mL). Cool down the reaction mixture to $-78\text{ }^\circ\text{C}$ using a cooling bath filled with dry ice and acetone. Charge the dropping funnel with THF (15 mL) followed by superhydride solution (LiBHEt_3 , 1 M in THF, 6 mL). Add this solution to the reaction mixture dropwise over the course of 20 minutes. The reaction should change colour from red–orange to green. The superhydride solution should be fresh. A tell–tale sign that it is not fresh enough is that the reaction mixture does not turn green upon addition of the superhydride solution. If the reaction mixture does not turn green, the reaction will not work. Allow the reaction temperature to rise slowly to approximately $-30\text{ }^\circ\text{C}$, do this by lowering the dry ice bath to just below the bottom of the flask. Stir the reaction for 30 minutes. Cool the reaction mixture to $-78\text{ }^\circ\text{C}$ again. Charge the dropping funnel with THF (15 mL) followed by trifluoroacetic acid (TFA, 0.8 mL). Add this solution to the reaction mixture dropwise over the course of 20 minutes. The reaction should now change from green to red. Add the hexamethylenetetramine (420 mg) to the reaction solution. This produces a clear red orange solution, which you should allow to warm to room temperature and then stir for 28 hours. After 28 hours, evaporate the solvent under reduced pressure,

then redissolve in the minimum volume of DCM before passing the crude product through a silica plug with DCM eluent. Evaporate the solvent.

Prepare a graduated gravity silica column. The starting eluent should be 9:1 pentane to DCM followed by 8:2 pentane to DCM and then 7:3 pentane to DCM. The third red band to come off the column is the product. This column can take up to 6 hours because, in my experience, it is very unhelpful to use an automated column machine (e.g. flashmaster) or to run it as a flash column. Sit back, relax and enjoy some podcasts while you watch the bands fall slowly off the column (Recommended podcasts; Off Menu, Happy Place, No Such Thing as a Fish).



Scheme A1.4. Synthetic route to compound $2b^{2-}$.

Following purification of **2a**, dissolution in acetonitrile and addition of tetraethylammonium cyanide $[\text{Et}_4\text{N}^+][\text{CN}^-]$ results in substitution of two carbonyl ligands with two cyanide ligands over the course of 2 hours at room temperature (scheme A1.4).⁵⁴ The solvent should be evaporated and the product redissolved in degassed acetone. Then the product should be precipitated by adding degassed diethyl ether, and storing the flask in the freezer over night (-30°C). Finally, wash the supernatant should be removed, and the red-brown solid should be washed repeatedly with degassed diethyl ether. The red-brown solid should be dried for one day under vacuum on the Schlenk-line.

Appendix 2 – Synthesis of **36e** and using **36e** to make a semi-synthetic [FeFe]-hydrogenase

As stated in Chapter 6, one exciting route for the manganese project is that the dicyanide derivative, **36e**, may be used to artificially maturate an apo-hydrogenase enzyme to create a semi-synthetic hydrogenase. This was already successfully attempted using a diruthenium complex. However the use of a dimanganese complex to create a [MnMn]-H₂ase would provide a more biologically relevant aspect in this field of study because it has been shown in some enzymes, such as ribonucleotide reductase (RNR) or superoxide dismutase (SOD), that Mn and Fe can perform reactions that involve the same chemical transformations. Here, I synthesised a dicyanide substituted mimic following similar procedures to the synthesis of **36b-d** in chapter 6, and furthermore attempted to use **36e** to make a semi-synthetic [MnMn]-H₂ase.

These results are very new, and require further investigation pending full characterisation of the new complex, and optimisation of the artificial maturation procedure.



Figure A2.1. Reaction scheme to form **36e**.

36e was produced following the procedure described in scheme A2.1. **36a** was dissolved in benzene, 38 mg, (0.1 mmol) along with Et₄NCN, 64 mg (0.4 mmol) and Me₃NO, 30 mg (0.4 mmol). This reaction mixture was stirred at 80 °C for 2 hours. A precipitate slowly formed. This precipitate did not move on a silica tlc plate, so it was washed with benzene, followed by pentane, to yield a mustard brown powder, 44 mg, (0.07 mmol, 70 % yield).

The reaction product was observed by FTIR, and showed two bands in the cyanide region of the spectrum at 2139 cm^{-1} and 2099 cm^{-1} , and three carbonyl bands at 2013 cm^{-1} , 2003 cm^{-1} , and 1911 cm^{-1} . The product was water soluble, so **36e** was used further to try and make a semi-synthetic enzyme.

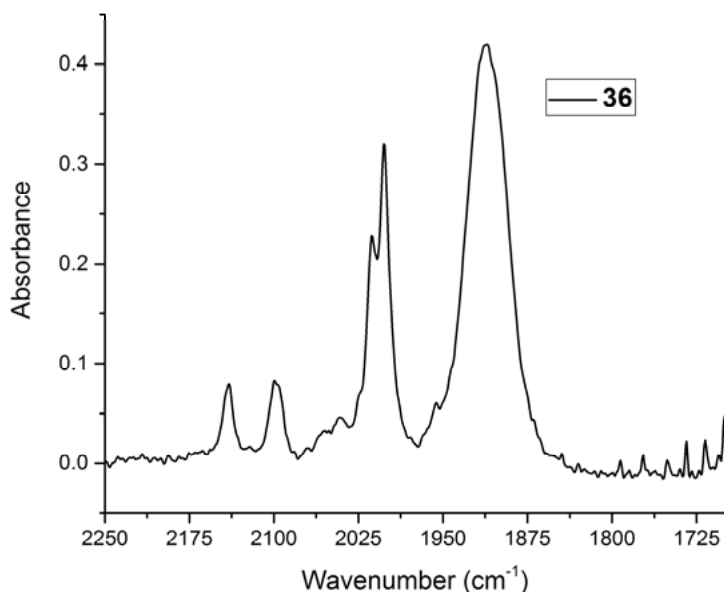


Figure A2.2. FTIR spectrum of 36e in DCM

The FTIR of **36e** was recorded in aqueous solution, 0.01 M tris-HCl, pH 8.0, 2 mM NaDT, and the following vibrational bands were observed; 2098 cm^{-1} , 2069 cm^{-1} , 2047 cm^{-1} , 2006 cm^{-1} , 1916 cm^{-1} and 1838 cm^{-1} (figure A2.3, black spectrum). The complex was mixed with apo-HydA1 under reducing conditions, and the resultant enzyme was purified via size exclusion chromatography. The new sample was measured by FTIR and slight difference in the spectra were observed ($\tilde{\nu} = 2096\text{ cm}^{-1}$, 2022 cm^{-1} , 1939 cm^{-1} , 1920 cm^{-1}) (figure A2.3, red spectrum). However these were not the typical sharpening of cofactor bands usually accompanied by insertion of the cofactor into the active site pocket.¹⁸⁹ Firstly the carbonyl bands shifted to higher wavenumbers. The broad band at 1838 cm^{-1} in the buffer disappeared after mixing with apo-HydA1 and the broad strong band at 1916 cm^{-1} shifted to 1920 cm^{-1} in the red spectrum, the band also appeared to be slightly more resolved revealing another band at 1936 cm^{-1} . The carbonyl band at 2006 cm^{-1} in the black spectrum shifted to 2022 cm^{-1} in the red spectrum. The cyanide bands in the black spectrum disappeared to leave only one cyanide band at 2096 cm^{-1} . A hydrogen evolution assay of the semi-synthetic enzyme revealed no H_2 production activity.

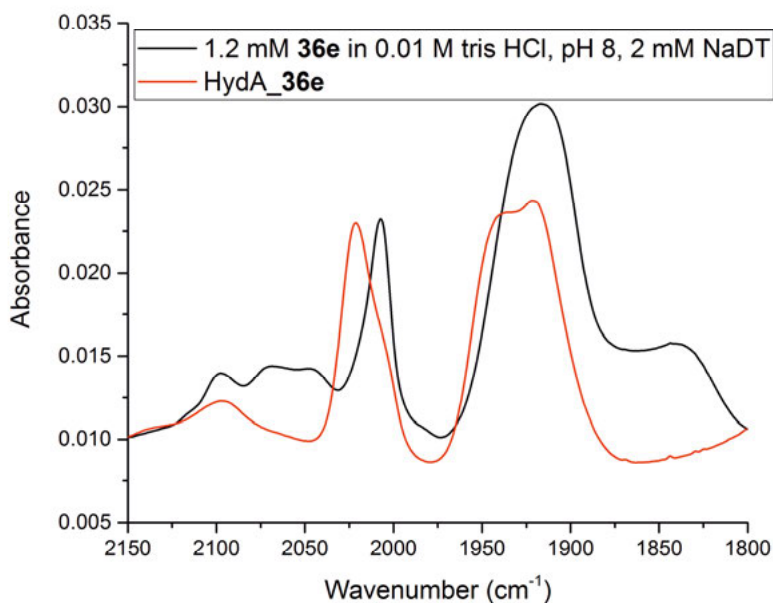


Figure A2.3. FTIR of **36e** in aqueous buffer (black spectrum); FTIR of HydA1 matured with **36e** in aqueous buffer (red spectrum).

The FTIR data clearly show a difference between the dimanganese cofactor, **36e**, in aqueous buffer, and the HydA1-**36e** in aqueous buffer. However, we expected to observe sharpening of the cofactor bands upon insertion into the enzyme active site pocket, which we do not observe in this case. Furthermore we observe no H₂ evolution activity. Still, the complex evidently binds to the protein, as it could be observed by FTIR following size-exclusion chromatography. These data together may suggest that the complex is stuck on the surface of the enzyme, as has been observed for other [FeFe]-H₂ase cofactor mimics by Siebel *et al.*,¹⁸⁹ and Marco Lorenzi (unpublished work). However, they are still inconclusive because the full characterisation of **36e** is needed, and repeats of this experiment should be carried out.

Acta Universitatis Upsaliensis

*Digital Comprehensive Summaries of Uppsala Dissertations
from the Faculty of Science and Technology 2132*

Editor: The Dean of the Faculty of Science and Technology

A doctoral dissertation from the Faculty of Science and Technology, Uppsala University, is usually a summary of a number of papers. A few copies of the complete dissertation are kept at major Swedish research libraries, while the summary alone is distributed internationally through the series Digital Comprehensive Summaries of Uppsala Dissertations from the Faculty of Science and Technology. (Prior to January, 2005, the series was published under the title "Comprehensive Summaries of Uppsala Dissertations from the Faculty of Science and Technology".)



ACTA
UNIVERSITATIS
UPSALIENSIS
UPPSALA
2022

Distribution: publications.uu.se
urn:nbn:se:uu:diva-470634